Active and Passive Coupled-Resonator Optical Waveguides

Thesis by

Joyce Kai See Poon

In Partial Fulfillment of the Requirements

for the Degree of

Doctor of Philosophy

California Institute of Technology

Pasadena, California

2007

(Defended May 21, 2007)

Thesis Committee

Professor Amnon Yariv (Chair)

Professor Marc W. Bockrath

Professor Bruno Crosignani

Professor Axel Scherer

Professor Kerry J. Vahala

Professor Changhuei Yang

Acknowledgments

I am grateful for the many people who created a supportive environment for me to grow intellectually and personally over the last five years. I am thankful for Professor Amnon Yariv for giving me the opportunities to mature as a researcher and scientist. His keen physical intuition and unwavering scientific enthusiasm have been a constant source of motivation and inspiration.

I thank Professors Marc Bockrath, Bruno Crosignani, Kerry Vahala, Axel Scherer, and Changhuei Yang for being part of my thesis committee, as well as Professors Hideo Mabuchi and Demetri Psaltis who were part of my candidacy committee. From Professor Bruno Crosignani, I have learned much about the culture of science. I enjoyed working with Dr. Willie Ng of HRL Laboratories who introduced me to research outside academia. I thank Professor John O'Brien and his group at the University of Southern California for allowing me to experience a different research environment.

My research group has been my family here at Caltech and the Watson building has been my home away from home. I have learned a lot from working with everyone and am thankful for their technical help, stimulating conversations, and friendship. In the past couple of years, I have enjoyed many interesting discussions with Lin Zhu and Dr. Philip Chak. Philip's precise thinking and unending patience are deeply appreciated. I would like to express my gratitude for Lin's help on the electron-beam lithography and Dr. John Choi's assistance on the coupled Fabry-Perot resonators. I am grateful for Professor Yanyi Huang, Professor Shayan Mookherjea, Dr. George Paloczi, Dr. William Green, Professor Koby Scheuer, and Professor Yong Xu for

setting me on my research path. Yanyi and George introduced me to the world of experiments and optical polymers, while Shayan, Koby, and Yong led me to appreciate the beauty in theory. Will has always been available to answer any questions even though he is now across the country. Dr. Reginald Lee and Dr. T. R. Chen are always a source of expert advice. Even though our current projects are quite different, I have enjoyed technical and broader discussions with Wei Liang and Naresh Satyan. During this past year, I have also enjoyed working with Xiankai Sun, Hsi-Chun Liu, and James Raftery.

The friendship of Ali Ghaffari and the assistance of Dr. Guy DeRose on the electron-beam lithography are deeply appreciated. Connie Rodriguez has been our tireless "group mom." Irene Loera, Linda Dozsa, Jennifer Su, Mabel Chik, Cierina Marks, Eleonora Vorobieff, and Kevin Cooper have also helped me with countless administrative matters. The dedication of the staff at Caltech to the students and faculty is truly unparalleled.

I am grateful for the Natural Sciences and Engineering Research Council of Canada, the IEEE Laser & Electro-Optics Society. and the Optical Society of America for supporting my graduate studies. The work presented in this thesis was financially supported by HRL Laboratories, the National Science Foundation (Award No. 0438038), and the Defense Advanced Research Projects Agency (Slow Light Project).

Several friends from my high school who made California their home have been a reminder that life exists outside of Caltech. Caroline Ong, Joanna Lai, and Eric Tang have been wonderful friends for 15 years and counting.

Above all, I thank my parents and my sister for their infinite patience, support, and understanding. Graduate school has been as much of a learning experience for them as it has been for me.

Abstract

Coupled-Resonator Optical Waveguides (CROWs) are chains of resonators in which light propagates by virtue of the coupling between the resonators. The dispersive properties of these waveguides are controllable by the inter-resonator coupling and the geometry of the resonators. If the inter-resonator coupling is weak, light can be engineered to propagate slowly in these structures. The small group velocities possible in CROWs may enable applications in and technologies for optical delay lines, interferometers, buffers, nonlinear optics, and lasers.

This thesis reports on achieving and controlling the optical delay in passive and active CROWs. Both theoretical and experimental results are presented. Transfer matrices, tight-binding models, and coupled-mode approaches are developed to analyze and design a variety of coupled resonator systems in the space, frequency, and time domains. Although each analytical method is fundamentally different, in the limit of weak inter-resonator coupling these approaches are consistent with each other. From these formalisms, simple expressions for the delay, loss, bandwidth, and a figure of merit are derived to compare the performance of CROW delay lines. Using a time-domain tight-binding model, we examine the resonant gain enhancement and spontaneous emission noise in amplifying CROWs to find that the net amplification of a propagating wave does not always vary with the group velocity but instead depends on the termination and excitation of the CROW.

CROWs in the form of high-order (> 10) weakly coupled passive polymer microring resonators were fabricated and measured. The measured transmission, group delay, and dispersive properties of the CROWs agreed with the theoretical results.

Delays in excess of 100 ps and slowing factors of about 25 over bandwidths of about 20 GHz were observed. The main limitation of the passive CROWs was the optical losses. To overcome the losses and to enable electrical integration, we demonstrated active CROWs in the form of current injection InP-InGaAsP Fabry-Perot laser arrays. Even though the losses could be completely compensated, the transmission spectra and signal-to-noise ratio depended strongly on the injection current and resonator position. The signal-to-noise ratio degraded rapidly away from the input. Our results highlight possible avenues to operate laser arrays as loss-compensated or amplifying CROWs.

Table of Contents

List of Figures

List of Tables

List of Frequently Used Abbreviations and Symbols

α, a	Gain/loss coefficient
β	Propagation constant
Λ	Spatial period
κ	Dimensionless, length-integrated coupling constant
κ_1	Normalized spatial overlap integral
κ_l	Coupling coefficient per unit length
κ_t	Coupling rate per unit time
Ω	Resonance frequency of a single resonator
c	Speed of light in vacuum
$\mathcal{F}$	Finesse
K	Bloch wave-vector
n	Refractive index
n_{eff}	Effective index
n_g	Group index
Q	Quality factor
Q_{int}	Intrinsic quality factor
Q_{ext}	External quality factor
Q_L	Loaded quality factor
S	Slowing factor

t	Dimensionless, length-integrated transmission coefficient
v_g	Group velocity
CROW	Coupled-resonator optical waveguide
DFB	Distributed feedback
FWHM	Full-width half-maximum
FSR	Free spectral range
GVD	Group velocity dispersion
InP	Indium phosphide
InGaAsP	Indium gallium arsenide phosphide
TE	Transverse electric
TM	Transverse magnetic
UV	Ultra-violet

Chapter 1

Overview

Resonators and oscillators are prevalent in many fields of science and engineering, from mechanical springs to capacitors and inductors. Resonators are able to store large amounts of energy built up from a considerably weaker input. Optical resonators, in the same way, are capable of storing and building up intense optical fields. Optical resonators are commonplace, for example, they are used as laser cavities and Fabry-Perot etalon spectrum analyzers. While optical resonators have been studied for many years [1], only with recent developments in fabrication technologies over the past decade or so have researchers been able to fabricate optical microresonators which have micron to sub-micron sizes.

Because of their compact, essentially chip-scale sizes, optical microresonators have been attracting considerable theoretical and experimental attention, since they have applications in fields ranging from fundamental physics to telecommunications systems [2]. Resonators with effective volume $V \leq (\frac{\lambda_0}{n})^3$ possessing only one electromagnetic mode in a given spectral region (such as the emission region of an inverted atomic population), have been essential for studies in atom-light interactions such as cavity quantum electrodynamics (QED) and the Purcell effect [2]. Microresonator lasers may have low thresholds since both the spontaneous emission as well as the stimulated emission can take place into the same, single, electromagnetic mode.[2] Resonators can also be used as optical filters and add-drop multiplexers for optical communication systems [3, 4, 5].

1.1 Basic Properties of Optical Resonators

Several parameters are important in the description of resonators: the free spectral range, the quality factor, and the finesse. We will be referring to these terms frequently throughout this work. The free spectral range (FSR) is a measure of the optical path inside the resonator and gives the frequency or wavelength spacing between the resonances. The FSR is defined as

$$\Delta\omega_{FSR} \equiv \Omega_{m+1} - \Omega_m, \tag{1.1}$$

where Ω_{m+1} and Ω_m are consecutive resonance orders. The resonance condition is satisfied whenever

$$\beta_m L_{RT} + \phi_0 = 2m\pi, \tag{1.2}$$

where $\beta_m = \Omega_m n_{eff}/c$ is the propagation constant, L_{RT} is the round-trip length of the resonator, and ϕ_0 is any additional phase that the light may accumulate in a round-trip. n_{eff} is the effective index of the resonator and c is the speed of light. Therefore, substituting into Eq. (1.1), we obtain

$$\Delta\omega_{FSR} = \frac{2\pi c}{n_g L_{RT}}. \tag{1.3}$$

n_g is the group index, defined as

$$n_g = n_{eff}\left[1 + \omega\frac{1}{n_{eff}}\frac{\partial n_{eff}}{\partial\omega_{|\Omega}}\right]. \tag{1.4}$$

Because of their small sizes, microresonators can have FSRs of the order of GHz to THz, making them useful for filtering applications in optical communication systems, for example in wavelength division multiplexed (WDM) channels.

The second property used in descriptions of resonators is the quality factor, Q. The Q factor describes the losses of the resonator and is defined as [1]

$$Q \equiv \Omega \times \frac{\text{Field Energy Stored}}{\text{Power Dissipated}}, \tag{1.5}$$

where Ω is the resonance frequency of the resonator. Assuming that U is the field energy stored, α_{RT} is the fractional loss per round-trip in the resonator, and τ_{RT} is the round-trip time, the power dissipated by the resonator is

$$\text{Power Dissipated} = \frac{\alpha_{RT} U}{\tau_{RT}}. \tag{1.6}$$

Thus, substituting into Eq. (1.5), we have

$$Q = \Omega \frac{\tau_{RT}}{\alpha_{RT}}. \tag{1.7}$$

From Eq. (1.7), Q can be improved by either increasing the propagation time in the resonator if the round-trip loss is fixed or by decreasing the round-trip loss.

The Q factor is also related to the bandwidth of a Lorentzian lineshape. For a Lorentzian lineshape, the energy decays exponentially in the resonator so $\alpha_{RT} = 1 - \exp(-\tau_{RT}/\tau_L)$, where $1/\tau_L$ is the rate of the dissipation. Hence, for small losses such that $\alpha_{RT} \approx \tau_{RT}/\tau_L$, Eq. (1.7) becomes

$$Q = \Omega \tau_L = \frac{\Omega}{\Delta\omega_{1/2}} = \frac{\lambda_0}{\Delta\lambda_{1/2}}, \tag{1.8}$$

where $\Delta\omega_{1/2}$ and $\Delta\lambda_{1/2}$ are the full-widths half-maximum (FWHM) in frequency and wavelength of the lineshape respectively, and λ_0 is the resonance wavelength. Eq. (1.8) is a particularly useful expression of the Q factor for comparison with experiments, where $\Delta\omega_{1/2}$ and $\Delta\lambda_{1/2}$ can be directly measured.

The final property is often used to describe resonators is the finesse, $\mathcal{F}$. The definition of finesse originally arose from the resolving power of a Fabry-Pert etalon and is the ratio of the FSR to the FWHM width of the resonance,

$$\mathcal{F} = \frac{\Delta\omega_{FSR}}{\Delta\omega_{1/2}} = \frac{\Delta\lambda_{FSR}}{\Delta\lambda_{1/2}}. \tag{1.9}$$

$\mathcal{F}$ can alternatively be viewed as a parameter that combines the FSR and Q, since

for the case of a Lorentzian lineshape,

$$\mathcal{F} = \frac{\Delta\omega_{FSR}Q}{\Omega} = \frac{\Delta\lambda_{FSR}Q}{\lambda_0}. \tag{1.10}$$

1.2 Optical Microresonators

Recent advances in fabrication technologies and application-driven demands, particularly in telecommunications, sensing, and quantum computing, have enabled a rapid development of optical microresonators. Microresonators can be broadly classified into two categories depending on how they trap light: those that rely on total internal reflection (TIR) and those that rely on Bragg reflection for optical confinement.

Examples of TIR microresonators include microspheres [6, 7], microdisks [8], microtoroids [9], and microrings [5, 10, 11, 12]. TIR microresonators have been fabricated in a wide variety of materials including silica, silicon, compound semiconductors, and polymers. The size of a TIR microresonator is limited by the TIR condition, or equivalently, the index difference between the guiding region and the cladding. Compared to Bragg resonators, index-guided resonators have the advantage that they are typically easier to fabricate, for example requiring only photolithography, and also have simpler coupling mechanisms, since the design of phase-matched couplers is better understood. Moreover, this type of resonators has been demonstrated to possess Q factors in excess of 10^8 [6, 7]. Ultra-high Q factors offer opportunities to explore numerous fundamental aspects of optics, such as parametric effects [13], opto-mechanical coupling [14], and light-atom coupling [15].

The second category of microresonators relies on Bragg reflection to confine light. Examples of Bragg resonators include quarter-wave shifted distributed feedback (DFB), photonic crystal (PC), Bragg annular, and onion cavities [1, 16, 17, 18]. This type of resonator can possess significantly smaller physical sizes than index-guided resonators since they are not limited by total internal reflection.

1.3 Coupled-Resonator Optical Waveguides

As optical microresonators have the capability of storing light in physically small volumes, we envision that a chain of coupled microresonators may provide a new method for controlling the group velocity of optical pulses in a compact way on a chip. A coupled-resonator optical waveguide (CROW) consists of a chain of resonators in which light propagates in virtue of the coupling between the adjacent resonators [19, 20, 21]. CROWs have the potential to significantly slow down the propagation of light, which may find applications such as optical delay lines, interferometers, optical buffers, and nonlinear optics [22, 23, 24].

Coupled optical resonators have already become important in nonlinear optics research as well as in telecommunication applications in recent years [25, 26, 27, 28]. Systems consisting of a few coupled resonators, say $1 < N < 5$, have been proposed and demonstrated for optical filtering and modulation [4, 3, 22]. CROWs are "large" systems at the other extreme, with say $N > 10$ resonators, and can be regarded as waveguides with unique and controllable dispersion properties [19, 20, 25, 29].

1.3.1 Tight-Binding Analysis

The "large" chains (CROWs) have been previously analyzed using a spatial tight-binding formalism [19]. In the tight-binding method, we approximate the electric field of an eigenmode $\mathbf{E}_K$ of the CROW as a Bloch wave superposition of the individual resonator modes $\mathbf{E}_\Omega$ [19],

$$\mathbf{E}_K(\mathbf{r},t) = E_0 \exp(i\omega_K t) \sum_n \exp(-inK\Lambda)\mathbf{E}_\Omega(\mathbf{r} - n\Lambda\hat{\mathbf{z}}), \tag{1.11}$$

where the nth resonator in the chain is centered at $z = n\Lambda$.

We substitute Eq. (1.11) into the wave equation and adopt the normalization $\int \mathrm{d}^3\mathbf{r}\mathbf{E}^*_\Omega(\mathbf{r})\epsilon_\Omega(\mathbf{r})\mathbf{E}_\Omega(\mathbf{r}) = 1$, where $\epsilon_\Omega(\mathbf{r})$ is the dielectric coefficient of an individual resonator. Under the assumption of symmetric nearest neighbor coupling, after some

algebra, we find the dispersion relation of the CROW is [19]

$$\omega_K = \Omega \left[1 - \frac{\Delta\alpha}{2} + \kappa_1 \cos(K\Lambda) \right], \tag{1.12}$$

where Ω is the resonant frequency of an individual resonator and $\Delta\alpha$ and κ_1 are defined as

$$\Delta\alpha = \int \mathrm{d}^3\mathbf{r}[\epsilon(\mathbf{r}) - \epsilon_\Omega(\mathbf{r})]\mathbf{E}_\Omega(\mathbf{r}) \cdot \mathbf{E}_\Omega(\mathbf{r}) \tag{1.13a}$$

$$\kappa_1 = \int \mathrm{d}^3\mathbf{r}[\epsilon_\Omega(\mathbf{r} - \Lambda\hat{\mathbf{z}}) - \epsilon(\mathbf{r} - \Lambda\hat{\mathbf{z}})]\mathbf{E}_\Omega(\mathbf{r}) \cdot \mathbf{E}_\Omega(\mathbf{r} - \Lambda\hat{\mathbf{z}}), \tag{1.13b}$$

where $\epsilon(\mathbf{r})$ is the dielectric coefficient of the CROW. Therefore, the coupling parameter κ_1 represents the overlap of the modes of two neighboring resonators and $\Delta\alpha/2$ gives the fractional self-frequency shift of ω_K.

The aforementioned tight-binding expansion is mathematically elegant and applies to any kind of resonator. It has been used extensively to study both linear and nonlinear optical propagation in CROWs [30, 31, 32, 33]. This theoretical framework most readily lends itself to the analysis of infinitely long, lossless CROWs, or those in which periodic boundary conditions apply, consisting of identical resonators.

1.4 Motivation and Organization of the Thesis

Since the initial proposal of CROWs [19, 20], most of the research to date on CROWs has been theoretical in nature. With such unique dispersive properties and the potential to significantly slow down propagating optical pulses, CROWs may find applications in many fields of science and engineering. This thesis brings CROWs from the theoretical realm into practice by developing the theoretical and experimental approaches to understanding, explaining, and measuring light propagation in active and passive CROWs.

We begin with Chapter 2 wherein we develop a theoretical approach based on transfer matrices to analyze CROWs that can be easily corroborated with experimental results. A set of design rules for CROW delay lines is presented in Chapter

3, which quantifies the fundamental trade-offs between bandwidth, delay, and loss in CROWs. Chapter 4 gives an introduction to optical polymers as well as the fabrication and measurement of single microring resonators. We then present amplitude and time-delay measurements of CROWs in the form of high-order coupled ring resonators in Chapter 5.

The last several chapters of the thesis discuss CROWs in active, optically amplifying media. Chapter 6 develops a time-domain tight-binding model to examine the spontaneous emission noise and the effect of the termination of CROWs on the net gain through the structure. Chapter 7 proposes Fabry-Perot resonator arrays as a means to achieve a large reduction of the group velocity without using a high refractive index contrast material system, culminating in a demonstration of active CROWs in the form of current injection InP-InGaAsP laser arrays in Chapter 8. Some basic properties of transfer matrices and their applications to other types of coupled resonators are included in Appendix A.

Chapter 2

Matrix Analysis of Coupled-Resonator Optical Waveguides

2.1 Introduction

In this chapter[1], we use a transfer matrix formalism to investigate continuous-wave and pulse propagation through microring CROWs. In the limit of weak inter-resonator coupling, we shall find the dispersion relation agrees with that derived using the tight-binding model, and the equivalent time domain equations agree with temporal coupled-mode theory. We will obtain analytical expressions for pulse propagation through a semi-infinite CROW in the case of weak coupling which fully accounts for the nonlinear dispersive characteristics. We shall also show that intensity of a pulse in a CROW is enhanced by a factor inversely proportional to the inter-resonator coupling. In finite CROWs, anomalous dispersion allows for a pulse to propagate with a negative group velocity such that the output pulse will appear to emerge before the input as in "superluminal" propagation. The matrix formalism, as we will demonstrate, is a powerful approach for microring CROWs since it can be applied to structures and geometries for which analyses with the commonly used tight-binding or temporal coupled-mode approach are not applicable.

The theory of CROWs and other coupled-resonator systems has been explored extensively in recent years. Much of the theoretical work on CROWs thus far has been based on the tight-binding method described in Section 1.3.1 [25, 27] and the temporal

[1] ©2004 OSA. Reprinted, with permission, from [34] and [35].

coupled-mode theory [5, 36]. The temporal coupled-mode equations [37] are largely phenomenological, and the tight-binding method, while mathematically elegant, is not always convenient for physical systems. For example, it does not readily account for input/output coupling, loss, different resonator sizes, finite resonator chains, or variations in coupling strengths.

In practice, the number of coupled resonators in a CROW is finite and possibly not very large, hence we need a design-oriented analysis tool that can deal with any number of resonators $1 \leq N < \infty$. The transfer matrix approach [38, 39, 40] is particularly powerful since it can deal with any arbitrary sequence of resonators and couplers, which is a prerequisite to general optical filter design [3, 5, 41]. With the aim of rigorously analyzing realistic CROW structures, we use the transfer matrices to study a system consisting of N coupled ring resonators with input and output waveguides.

We choose to study a specific model of a sequence of ring resonators that are coupled serially in a phase-matched manner as in Fig. 2.1 for the following reasons:

1. Ring resonators can be made to support a single transverse mode in a given spectral region which is an essential feature in its practical and scientific applications. This property is in contrast to disk or spherical resonators with radii much greater than the optical wavelength.

2. Evanescent wave coupling between ring resonators and optical waveguides can be realized straight-forwardly and in the planar geometry by simple lithographic techniques.

3. The simple modal structure and coupling mechanism enable an essentially "exact" analytical treatment of arbitrary sequences of coupled ring resonators, thus a meaningful comparison to experiments.

Since the modal properties of ring resonators can be easily tailored and their fabrication technology is mature [41, 42], they may enable practical implementations of CROWs. The results we obtain from the analysis of the ring resonators will be generalized to photonic crystal and Fabry-Perot cavities in Section 2.7.

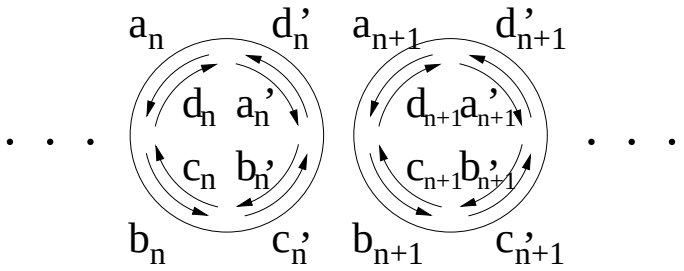

Figure 2.1: An infinitely long chain of coupled ring resonators, with the forward and backward propagating field components labelled

2.2 Transfer Matrix Formalism

We first consider an infinite chain of coupled ring resonators in order to obtain its dispersion relation. Both forward and backward propagating waves exist in an individual resonator, as shown in Fig. 2.1. We assume the coupling region is sufficiently long compared to λ, so that the light circulating in one direction in a resonator is phase-matched to only one of the two degenerate counter-propagating modes of the adjacent resonator. Using the notation of Fig. 2.1, the coupling between two adjacent rings can thus be described by [43]

$$\begin{bmatrix} b'_n \\ b_{n+1} \end{bmatrix} = \begin{bmatrix} t & \kappa \\ -\kappa^* & t^* \end{bmatrix} \begin{bmatrix} a'_n \\ a_{n+1} \end{bmatrix}, \quad \begin{bmatrix} d'_n \\ d_{n+1} \end{bmatrix} = \begin{bmatrix} t & \kappa \\ -\kappa^* & t^* \end{bmatrix} \begin{bmatrix} c'_n \\ c_{n+1} \end{bmatrix} \tag{2.1}$$

where t and κ are respectively the dimensionless transmission and coupling coefficients over the coupling length. The matrix is unitary and unimodular so that $|t|^2+|\kappa|^2 = 1$. Defining a vector with the different field components,

$$x_n = \begin{bmatrix} a \\ b \\ c \\ d \end{bmatrix}_n, \tag{2.2}$$

Eq. (2.1) can be rewritten as

$$x_{n+1} = \begin{bmatrix} P & 0 \\ 0 & P \end{bmatrix} x'_n \equiv \mathbb{P} x'_n \tag{2.3a}$$

$$P = \frac{1}{\kappa} \begin{bmatrix} -t & 1 \\ -1 & t^* \end{bmatrix}. \tag{2.3b}$$

As the field propagates around the ring, it accumulates a phase shift and may be attenuated, so

$$x'_n = \begin{bmatrix} 0 & Q \\ Q & 0 \end{bmatrix} x_n \equiv \mathbb{Q} x_n \tag{2.4a}$$

$$Q = \begin{bmatrix} 0 & \mathrm{e}^{-i\beta R\pi} \\ \mathrm{e}^{i\beta R\pi} & 0 \end{bmatrix}. \tag{2.4b}$$

In the above definition, R is the ring radius and $\beta = n_{eff}(\omega)\omega/c + i\alpha$, where $n_{eff}(\omega)$ is the frequency dependent effective index and α is the loss (or gain) per unit length in the ring. Combining Eqs. (2.3) and (2.4), we have

$$x_{n+1} = \mathbb{P}\mathbb{Q} x_n. \tag{2.5}$$

Eq. (2.5) is completely general. The matrices $\mathbb{P}$ and $\mathbb{Q}$ can be specified at each frequency to account for any frequency dependence of the effective index, loss, and transmission and coupling coefficients.

2.3 CROW Dispersion Relation

From a theoretical point of view, it is important to understand how the tight-binding and matrix approaches are related to each other. We shall show that the matrix method embodied in Eq. (2.5) converges to the tight-binding result in Eq. (1.12) under certain approximations. The approach we adopt is similar to the transfer matrix analysis of a Bragg stack [44].

The field in one resonator of the CROW as specified by x_n is

$$\mathcal{E}(\rho,\phi) = \mathbf{E}(\rho) \times \begin{cases} a_n \exp[i\beta R(\pi-\phi)] + d_n \exp[-i\beta R(\pi-\phi)] & 0 < \phi < \pi \\ b_n \exp[-i\beta R(\pi+\phi)] + c_n \exp[i\beta R(\pi+\phi)] & -\pi < \phi < 0 \end{cases} \tag{2.6}$$

where ϕ is the azimuthal angle relative to the propagation direction in the counter-clockwise sense, and ρ is the radial co-ordinate. For a mode of an infinite chain of ring resonators, the fields are periodic at the lattice constant, Λ. So applying Bloch's theorem,

$$x_{n+1} = \exp(-iK\Lambda)x_n, \tag{2.7}$$

where K is the CROW propagation constant. Combining this requirement with Eq. (2.5) leads to

$$\mathrm{Det}|\mathbb{PQ} - \exp(-iK\Lambda)U| = \mathrm{Det}|(PQ)^2 - \exp(-i2K\Lambda)U| = 0, \tag{2.8}$$

where U is the identity matrix.

We assume lossless propagation and $\mathrm{Im}(\kappa) \gg \mathrm{Re}(\kappa)$ for phase-matched coupling. We recall that at the resonant frequency of an individual resonator, Ω, $\Omega n_{eff}(\Omega)R/c = m$, where m is an integer, and $n_{eff}(\Omega)$ is the effective index at Ω. Therefore, solving Eq. (2.8), we obtain

$$\sin\left(\frac{n_{eff}(\omega)\omega\pi R}{c}\right) = \pm\mathrm{Im}(\kappa)\cos(K\Lambda), \tag{2.9}$$

which is the desired dispersion relation for a ring CROW. This relation is exact in the sense that it involves no assumption about the coupling strength. Approximating $n_{eff}(\Omega) \approx n_{eff}(\omega_K)$, Eq. (2.9) becomes

$$\sin\left(\frac{\omega_K}{\Omega}m\pi\right) = \pm\mathrm{Im}(\kappa)\cos(K\Lambda). \tag{2.10}$$

If we expand Eq. (2.9) in the parameter $\Delta\omega n_{eff}\pi R/c$, $\Delta\omega \equiv \omega_K - \Omega$, we obtain

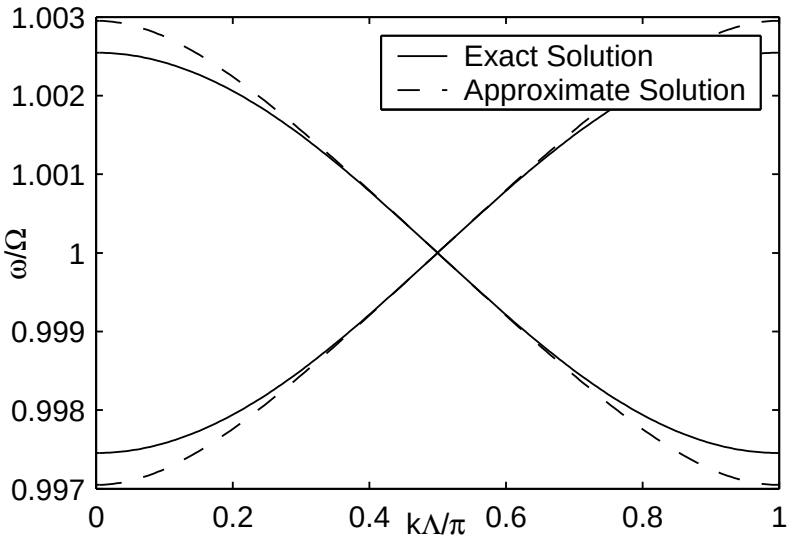

Figure 2.2: The exact and cosine-approximate (i.e., tight-binding-approximate) dispersion relations for $m = 100$ and $\kappa = -0.8i$

to first order

$$\frac{\omega_K}{\Omega} = 1 \pm \kappa_2 \cos(K\Lambda), \tag{2.11}$$

where $\kappa_2 \equiv \mathrm{Im}(\kappa)/(m\pi)$. The two dispersion relations corresponding to the '$\pm$' coexist for an infinite structure to allow for both forward and backward wave propagation (i.e., positive and negative group velocities). Physically, for a finite structure without reflection and a uni-directional input as in Fig. 2.3, only the dispersion relation with the matching group and phase velocities as the input wave will be of significance.

Eq. (2.11) is of a form identical to the tight-binding result in Eq. (1.12). The correction $\Delta\alpha/2$ term does not explicitly appear in Eq. (2.11) since it is accounted for by $\mathrm{Re}(\kappa)$. From Eq. (2.11), it follows that for $\Delta\omega m\pi/\Omega \ll 1$, it is necessary that $|\kappa| \ll 1$. This condition and the absence of all but the nearest neighbor coupling are thus the validity conditions for the tight-binding approximate result Eq. (2.11).

Figure 2.2 shows the dispersion relations for $\kappa = -0.8i$ and $m = 100$ as calculated using the "exact" form in Eq. (2.10) and the approximated form in Eq. (2.11). As ω_K/Ω increases, the exact dispersion relation deviates more significantly from the cosine form. For smaller values of κ, the deviation from the cosine dispersion relation is reduced.

The Bloch modes of the CROW are given by the eigenvectors of $\mathbb{PQ}$. At each frequency, there are 4 Bloch modes corresponding to the 4 eigenvalues (i.e., values of K). The eigenvalues are $\exp(-iK_1\Lambda) \equiv \xi_1$, $\exp[-i(K_1\Lambda + \pi)] \equiv -\xi_1$, $\exp(-iK_2\Lambda) \equiv \xi_2$, and $\exp[-i(K_2\Lambda + \pi)] \equiv -\xi_2$. The corresponding (un-normalized) eigenvectors are

$$\hat{q}_{\xi_1} = \begin{bmatrix} \zeta+\gamma \\ 1 \\ \zeta+\gamma \\ 1 \end{bmatrix}, \quad \hat{q}_{-\xi_1} = \begin{bmatrix} -(\zeta+\gamma) \\ -1 \\ \zeta+\gamma \\ 1 \end{bmatrix}, \quad \hat{q}_{\xi_2} = \begin{bmatrix} \zeta-\gamma \\ 1 \\ \zeta-\gamma \\ 1 \end{bmatrix}, \quad \hat{q}_{-\xi_2} = \begin{bmatrix} -(\zeta-\gamma) \\ -1 \\ \zeta-\gamma \\ 1 \end{bmatrix}, \tag{2.12}$$

where

$$\gamma = \frac{1}{2t}\sqrt{1+\exp(\frac{-4im\pi\omega}{\Omega}) + 2\exp(\frac{-2im\pi\omega}{\Omega})(1-2t^2)}, \tag{2.13a}$$

$$\zeta = \frac{1}{2t}\left[1+\exp(\frac{2im\pi\omega}{\Omega})\right]. \tag{2.13b}$$

The 4 eigenvectors are orthogonal to each other and they represent standing waves in each resonator. In the limit of weak coupling $|\kappa| \ll 1$ and $\omega \approx \Omega$, such that $\gamma \approx |\kappa| \approx 0$, $\zeta \approx 1$, and $\xi_1 = \xi_2$, the 4 eigenvectors reduce to 2 degenerate eigenvectors, representing the two different superpositions of the clockwise and counter-clockwise propagating waves in a single resonator:

$$\hat{q}_{\xi_1} = \hat{q}_{\xi_2} = \begin{bmatrix} 1 \\ 1 \\ 1 \\ 1 \end{bmatrix}, \quad \hat{q}_{-\xi_1} = \hat{q}_{-\xi_2} = \begin{bmatrix} -1 \\ -1 \\ 1 \\ 1 \end{bmatrix}. \tag{2.14}$$

In the limit of strong coupling and $\omega \approx \Omega$, $t \ll 1$, $\gamma + \zeta \approx \sqrt{\frac{1+|\kappa|}{1-|\kappa|}} \approx \frac{2}{t}$, and

$\zeta - \gamma \approx \sqrt{\frac{1-|\kappa|}{1+|\kappa|}} \approx 0$. The eigenvectors become

$$\hat{q}_{\xi_1} = \begin{bmatrix} \frac{2}{t} \\ 1 \\ \frac{2}{t} \\ 1 \end{bmatrix}, \quad \hat{q}_{-\xi_1} = \begin{bmatrix} -\frac{2}{t} \\ -1 \\ \frac{2}{t} \\ 1 \end{bmatrix}, \quad \hat{q}_{\xi_2} = \begin{bmatrix} 0 \\ 1 \\ 0 \\ 1 \end{bmatrix}, \quad \hat{q}_{-\xi_2} = \begin{bmatrix} 0 \\ -1 \\ 0 \\ 1 \end{bmatrix}. \tag{2.15}$$

We observe that 2 field components are significantly stronger than the other. This corresponds to a wave that "zig-zags" through the resonators without making complete round-trips in each resonator. The asymptotic behavior of the eigenvectors confirms the physical picture that as $|\kappa| \to 0$, the modes of the CROW are essentially the modes of the independent resonators, and as $|\kappa| \to 1$, the microrings no longer act as resonators and the CROW modes are essentially conventional waveguide modes.

2.4 Time Domain Analysis

Another powerful approach in the study of coupled resonator systems is the time domain or temporal coupled-mode analysis. A time domain picture can also more easily facilitate the study of pulse propagation in the presence of certain optical nonlinearities, such as the Kerr effect for example [26, 27]. Little et al. have previously analyzed coupled ring resonators using temporal coupled-mode theory [5]. We shall see that the transfer matrices are also consistent with this approach.

Since the matrix analysis is a frequency domain approach, the temporal dynamics is related to the transfer matrices by the Fourier transform. The field amplitudes in the matrix approach, a_n and b_n, are the frequency-dependent Fourier components of the field. From the coupling matrices and for unidirectional, phase-matched coupling such that $\kappa^* = -\kappa$ [1], using Eqs. (2.3) and (2.4), we find that

$$2ia_n \sin(\beta\pi R) = i|\kappa|(a_{n+1} + a_{n-1}). \tag{2.16}$$

Since $\beta = \omega n_{eff}/c$, in the same way that Eq. (1.12) can be approximated by Eq. (2.11) in the limit of weak coupling, the left side of Eq. (2.16) can be linearized such that

$$i\omega a_n - i\Omega a_n = \pm\frac{i|\kappa|c}{2n_g\pi R}(a_{n+1} + a_{n-1}), \tag{2.17}$$

where n_g is the group index. If $n_g \approx n_{eff}$, taking the inverse Fourier transform of Eq. (2.17), we find the evolution of the field in the time domain is

$$\frac{\mathrm{d}\tilde{a}_n(t)}{\mathrm{d}t} - i\Omega\tilde{a}_n(t) = \pm\frac{i|\kappa|\Omega}{2m\pi}[\tilde{a}_{n+1}(t) + \tilde{a}_{n-1}(t)]. \tag{2.18}$$

Attenuation or gain can be introduced by the addition of an imaginary part to n_{eff}. Substituting the form of the pulse envelope, $A_n(t) = \tilde{a}_n(t)\exp(-i\Omega t)$, into (2.18) yields

$$\frac{\mathrm{d}A_n(t)}{\mathrm{d}t} = \pm\frac{i|\kappa|\Omega}{2m\pi}[A_{n+1}(t) + A_{n-1}(t)]. \tag{2.19}$$

Eq. (2.19) represents a set of linear first-order differential equations that can be solved for specific initial conditions. In analogy to an array of coupled waveguides, the solution to (2.19) for the initial conditions $A_0(t=0) = 1$ and $A_{n\neq 0}(t=0) = 0$ is

$$A_n(t) = i^n J_n\left(\frac{t}{T_{ext}}\right), \tag{2.20}$$

where J_n is the n^{th} order Bessel function and $T_{ext} = \pm\frac{m\pi}{|\kappa|\Omega}$ [1]. Appropriate superpositions of Bessel functions can be used to satisfy any arbitrary initial conditions and can thus describe the evolution of an arbitrary pulse in an infinite ring resonator CROW in a purely temporal picture.

Eq. (2.18) is exactly identical to the result obtained previously by Little et al. whose analysis is completely based in the time domain [5]. Reynolds et al. have also derived the same result for coupled defects in photonic crystals with nearest neighbor coupling [36]. The result shows that the transfer matrix method is identical to the temporal coupled-mode theory in the limit of weak, phase-matched coupling. This equivalence is essential since it allows for the generalization of the results obtained

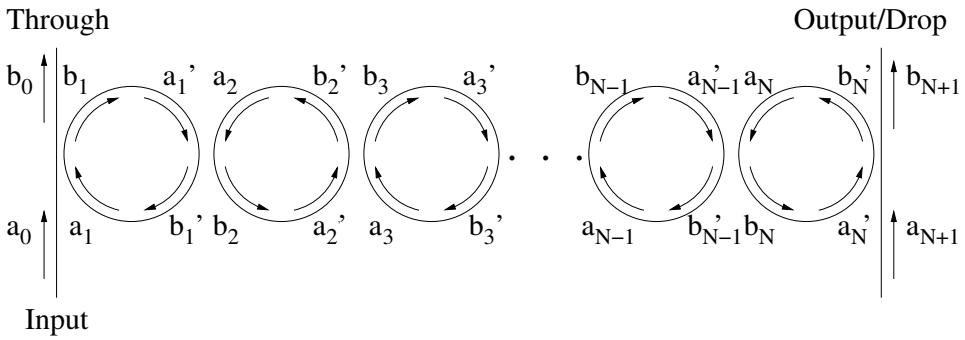

Figure 2.3: A CROW consisting of N ring resonators with input and output waveguides

using a particular approach to other structures for which that approach does not strictly apply.

2.5 Finite CROWs and a Travelling Wave Picture

For physical realizations of CROWs, we are interested in finite structures with input and output coupling. These properties can be easily incorporated into the transfer matrices. Fig. 2.3 shows a typical implementation of a microring CROW: light is coupled into and out of a set of coupled ring resonators via the input and output waveguides. Assuming that the coupling length between waveguides and the CROW is long compared to λ, then only the travelling wave phase-matched to the input can be excited.

Adopting the notation in Fig. 2.3, the fields between adjacent resonators are related by

$$\begin{bmatrix} a \\ b \end{bmatrix}_{n+1} = PQ \begin{bmatrix} a \\ b \end{bmatrix}_{n}, \tag{2.21}$$

where P and Q are defined in Eq. (2.3) and Eq. (2.4).

By cascading the transfer matrices, PQ, we obtain an expression for the field

components at the output of the CROW after N identical rings:

$$\begin{bmatrix} a_{N+1} \\ b_{N+1} \end{bmatrix} = P_{out}Q(PQ)^{N-1}P_{in} \begin{bmatrix} a_0 \\ b_0 \end{bmatrix} \equiv \begin{bmatrix} A & B \\ C & D \end{bmatrix} \begin{bmatrix} a_0 \\ b_0 \end{bmatrix}, \tag{2.22}$$

where P_{in} and P_{out} describe the coupling between the CROW and the input/output waveguides. For a single input to the waveguide, we set $a_{N+1} = 0$. Therefore, the transfer functions at the "through" and "output" ports as shown in Fig. 2.3 are

$$\frac{b_0}{a_0} = -\frac{A}{B} \equiv T_{thr}(\omega), \tag{2.23a}$$

$$\frac{b_{N+1}}{a_0} = C - \frac{AD}{B} \equiv T_{out}(\omega). \tag{2.23b}$$

As in microring filter design [5], the coupling between the waveguides and the CROW can be selected to maximize the flatness of the transmission response. Therefore, a finite CROW can be designed to mimic an infinite CROW over a bandwidth with a sufficiently flat transmission response.

An advantage of the matrix formalism is that it is valid for chains of any length N, which is essential in analyzing any physical realization of a CROW. From the phase response of the transmission function given by Eq. (2.23), we can deduce the dispersion relation of the structure. However, we note that the travelling wave is not an eigenmode of the CROW, since the Bloch modes as given by the eigenvectors of $\mathbb{PQ}$ are standing waves as in Eq. (2.12). A travelling wave solution is formed by a superposition, either the sum or difference, of the two Bloch modes with equal group velocities (i.e., $\hat{q}_{\xi_1}$ and $\hat{q}_{-\xi_1}$, or $\hat{q}_{\xi_2}$ and $\hat{q}_{-\xi_2}$). The travelling wave is an eigenvector of $(PQ)^2$, and it is verified that the sense of propagation in the rings alternates between clockwise and counter-clockwise with each operation of $\mathbb{PQ}$, as depicted in Fig. 2.3. Therefore, taking the phase difference accumulated over two rings to be $-2K\Lambda$, where K is the Bloch wave vector, such that the phase difference between the output and the input is approximately $-(N-1)K\Lambda$, we can determine the CROW dispersion from the finite structure.

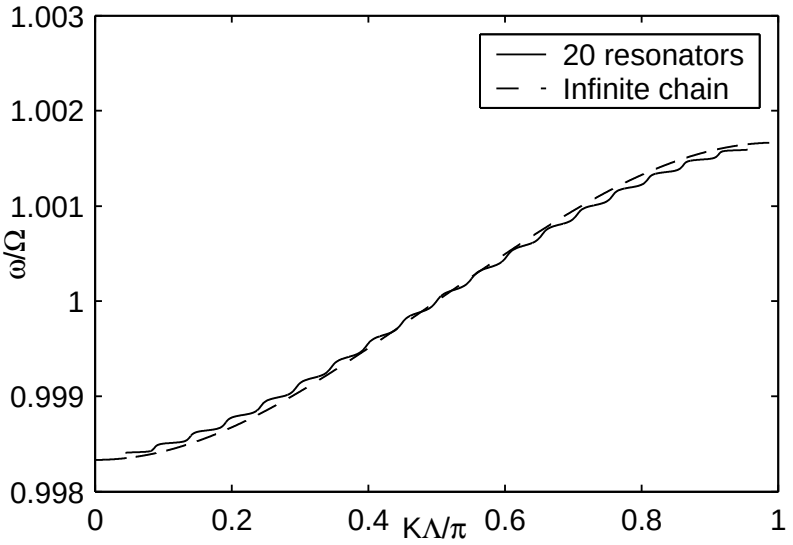

Figure 2.4: The exact dispersion relation for an infinite CROW and the dispersion relation as extracted from 20 coupled resonators. The rings have a radius of 16.4 μm and the inter-resonator coupling is $-0.5i$.

As an example, we compute the dispersion relation of a finite CROW consisting of 20 coupled rings with inter-resonator and waveguide-resonator coupling constants of $-0.5i$. The rings are lossless, and their radius is 16.4 μm. n_{eff} is taken to be constant and equal to 1.5. Fig. 2.4 compares the dispersion relation extrapolated from the finite CROW with the dispersion relation of an infinite CROW as given by Eq. (2.10). The small amplitude ripples are manifested at the resonance frequencies of the finite structure. In the limit of an infinite number of resonators, the resonance peaks will be infinitesimally close to each other and the ripples will be smoothed out.

2.6 Pulse Propagation

Pulse propagation through CROWs are of particular technological interest, since information transmitted in optical communication systems is typically encoded in pulses. Using the results from the previous sections, we can analytically and numerically study optical pulse propagation in semi-infinite and finite microring CROWs.

2.6.1 Semi-Infinite Case

A semi-infinite microring CROW consists of an infinitely long CROW coupled to a single input waveguide as in Fig. 2.5. The input waveguide ensures that only a pulse of positive (or negative) group velocity propagates through the structure. Assuming that the bandwidth of the input pulse is within the bandwidth of the CROW band such that all of the input light is coupled into the waveguide, the field amplitude b_1 in the first resonator is $b_1(\omega) = -1/\kappa_i a_0(\omega)$, where κ_i is the coupling coefficient between the input waveguide and the first resonator. Since $|\kappa_i| < 1$, the intensity of the field inside the CROW is higher than that of the input pulse by $1/|\kappa_i|^2$. This does not violate energy conservation, as the increased intensity is a consequence of the reduced group velocity and hence the spatial compression of the pulse inside the CROW. Using the dispersion relation in Eq. (2.11) and approximating $\Lambda \simeq 2R$, the maximum group velocity in the CROW is

$$v_{g,\max} = \frac{2c|\kappa|}{n_{eff}\pi}. \tag{2.24}$$

Defining the "slowing" factor to be

$$S = \frac{c}{n_{eff} v_{g,\max}}, \tag{2.25}$$

then S can be expressed as

$$S = \frac{\pi}{2|\kappa|}. \tag{2.26}$$

Therefore, for $\kappa_i = \kappa$, the intensity inside the rings is roughly enhanced by $(\frac{2}{3}S)^2$. This result makes intuitive sense since the only loss mechanism for the otherwise lossless resonators is the inter-resonator coupling. Interestingly, even though the energy velocity of the Bloch modes at Ω corresponds to the group velocity $v_{g,\max}$[44], the energy velocity of a wave that is fully coupled into the semi-infinite CROW is proportional to $|\kappa|^2$. Hence, the intensity enhancement is proportional to the energy velocity reduction rather than the group velocity reduction.

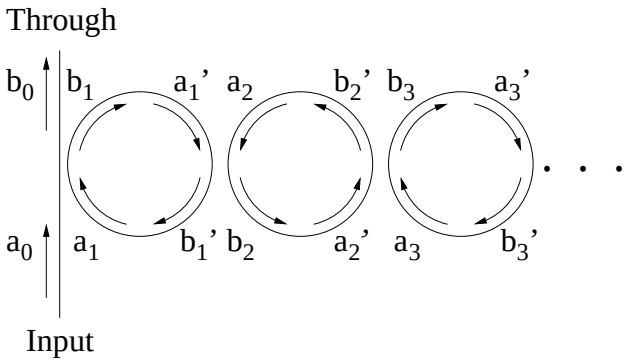

Figure 2.5: A semi-infinite CROW

Also, in contrast to CROWs, for other coupled resonator structures where there is no feedback between the resonators, such as the SCISSOR [45], the slowing factor is approximately proportional to $1/|\kappa|^2$ in the case of weak coupling. However, a CROW has the advantage that, even in the presence of loss, it is most transmitting for the frequencies of the CROW band, while a side-coupled resonator is most attenuating near the resonant frequency of the resonator.

To analyze the temporal dynamics of a pulse launched into the semi-infinite CROW, we adopt a method of analysis that is analogous to pulse propagation in conventional waveguides such as optical fibers. We shall find in the limit of weak coupling, such that Eq. (2.11) is a good approximation, there exists a closed-form solution to the evolution of any arbitrary input pulse.

The electric field where b_1 is taken, $\mathcal{E}(t, z = 0)$, can be expressed as the Fourier integral

$$\mathcal{E}(t, z = 0) = \int_{band} \mathrm{d}\omega b_1(\omega) \exp(i\omega t), \tag{2.27a}$$

$$b_1(\omega) = \int \frac{\mathrm{d}t'}{2\pi} \mathcal{E}(t', z = 0) \exp(-i\omega t'). \tag{2.27b}$$

At $z = N\Lambda$, each frequency component, $b_1(\omega)$, acquires a phase shift of $NK\Lambda$, so the field is

$$\mathcal{E}(t, z = N\Lambda) = \int_{band} \mathrm{d}\omega \exp(i\omega t) \int \frac{\mathrm{d}t'}{2\pi} \mathcal{E}(t', z = 0) \exp[-i(\omega t' + K(\omega) N\Lambda)]. \tag{2.28}$$

However, $K(\omega)$ is given by the dispersion relation of the CROW, Eq. (2.11). Therefore, instead of integrating over frequency in Eq. (2.28), if we integrate over the half of the Brillouin zone that gives the appropriate group velocity (for example, the right half), we obtain

$$\begin{aligned}\mathcal{E}(t, z = N\Lambda) = \; & -\Lambda\Omega\kappa_2 e^{i\Omega t} \textstyle\int_0^{\pi/\Lambda} \mathrm{d}K \sin(K\Lambda) e^{-iKN\Lambda} e^{i\Omega\kappa_2 \cos(K\Lambda)(t-t')} \\ & \textstyle\int \frac{\mathrm{d}t'}{2\pi} \mathcal{E}(t', z = 0) e^{-i\Omega t'}.\end{aligned} \tag{2.29}$$

Eq. (2.29) can be further simplified by letting $x = K\Lambda$, and invoking the Jacobi-Anger expansion [32],

$$e^{i\Omega\kappa\cos(x)(t-t')} = \sum_m c_m J_m[\Omega\kappa_2(t-t')]\cos(mx) \tag{2.30a}$$

$$c_m = \begin{cases} 1 & \text{if } m = 0 \\ 2i^m & \text{if } m > 0 \end{cases}, \tag{2.30b}$$

to arrive at

$$\begin{aligned}\mathcal{E}(t, z = N\Lambda) = \; & -\Omega\kappa_2 e^{i\Omega t} \textstyle\sum_m c_m \int_0^{\pi} \mathrm{d}x \sin(x)\cos(mx) e^{-ixN} \\ & \textstyle\int \frac{\mathrm{d}t'}{2\pi} J_m[\Omega\kappa_2(t-t')] \mathcal{E}(t', z = 0) e^{-i\Omega t'}.\end{aligned} \tag{2.31}$$

However, $\alpha_{m,N} = \int_0^{\pi} \mathrm{d}x \sin(x)\cos(mx)e^{-ixN} \neq 0$ only for certain values of m and N:

$$\alpha_{m,N} = \begin{cases} \frac{i\pi}{4} & \text{for } N = m-1 \text{ and } N = -m-1 \\ -\frac{i\pi}{4} & \text{for } N = m+1 \text{ and } N = -m+1 \\ \frac{-2(m^2+N^2-1)}{(m^2+N^2-1)^2-4m^2N^2} & \text{for } N+m = \text{even}. \end{cases} \tag{2.32}$$

So the equation for the pulse envelope $E(t, z)$, such that $\mathcal{E}(t, z) = E(t, z)e^{i\Omega t}$, is given by the convolution integral

$$E(t, z = N\Lambda) = -\frac{\kappa_2\Omega}{2\pi} \sum_m c_m \alpha_{m,N} \int \mathrm{d}t' J_m[\Omega\kappa_2(t-t')] E(t', z = 0). \tag{2.33}$$

The Fourier transform of a Bessel function $J_n(t)$ is only defined within $|2\pi f| \leq 1$ [46], which accounts for the finite bandwidth of the CROW, $\Omega(1-|\kappa_2|) \leq \omega \leq \Omega(1+|\kappa_2|)$.

Eq. (2.33) holds for an arbitrary input pulse and its sole assumption is the cosine-approximate dispersion relation, which is valid for small κ. The nonlinear dispersive nature of the CROW is embodied in the summation over the Bessel functions. Fig. 2.6(a) shows the evolution of a Gaussian input pulse $E(t, z = 0) = \exp(-t^2/T^2)$ as calculated using Eq. (2.33). Figure 2.6(b) shows the numerical results obtained from the transfer matrices. The analytical solution is in excellent agreement with the fully numerical approach. As the pulse propagates, even though the main peak travels at the group velocity, the ripples develop only at the tail end of the pulse.

2.6.2 Finite Case

Pulse propagation through finite CROWs can be easily analyzed using the transfer matrices results of Eq. (2.23). Since Eq. (2.23) is specified at each frequency, we simply have to find the product between the transfer functions and the spectral components of the input pulse. The temporal behavior follows naturally from the Fourier transform.

Distortionless propagation through an arbitrary finite CROW can always be achieved if the input pulse is sufficiently narrow-band such that the transmission function of the drop port, as defined in Fig. 2.3, over the pulse bandwidth is near unity. However, short pulses which become distorted as they propagate in the CROW are also of fundamental interest. For this purpose, we take an example consisting of 10 coupled ring resonators of radius 164.5 μm and $n_{eff} = 1.5$. The inter-resonator coupling constant is $-0.3i$ and the coupling between the waveguides and CROW is $-0.5i$. The transfer characteristics of this structure are shown in Fig. 2.7. We launch a 30.5 ps (FWHM) long pulse centered at 1.55 μm into the CROW.

Using the transfer matrices, we can examine how a pulse evolves in the CROW by finding the transfer functions associated with a_n or b_n. Fig. 2.8 shows the evolution of the pulse through the CROW. Even though the output pulse is attenuated compared

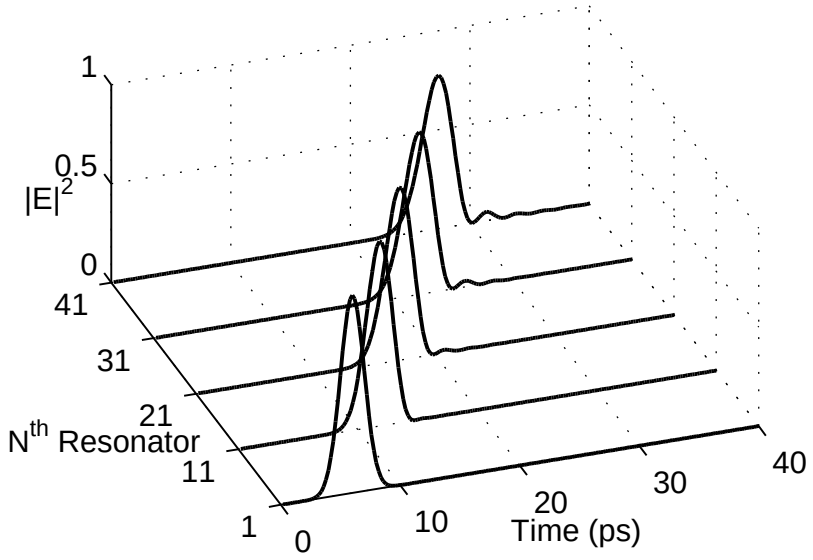

(a)

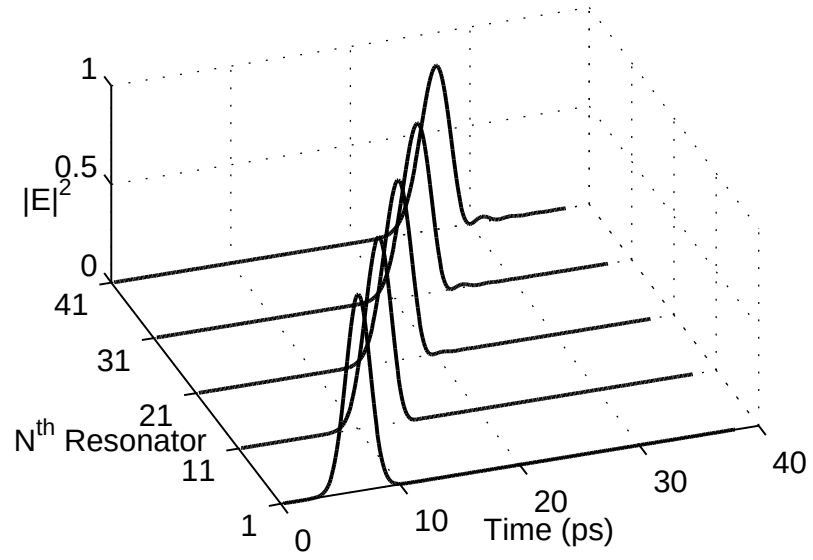

(b)

Figure 2.6: Evolution of a 2.4 ps (FWHM) Gaussian pulse centered about 1.5 μm in a semi-infinite CROW with $\kappa_2 = 0.0016$. The fields are normalized to the maximum field amplitude in the first resonator. (a) Theoretical results computed using Eq. (2.33). (b) Results computed numerically with the transfer matrices using a chain of 100 ring resonators ($n_{eff} = 1.5$, $R = 16$ μm)

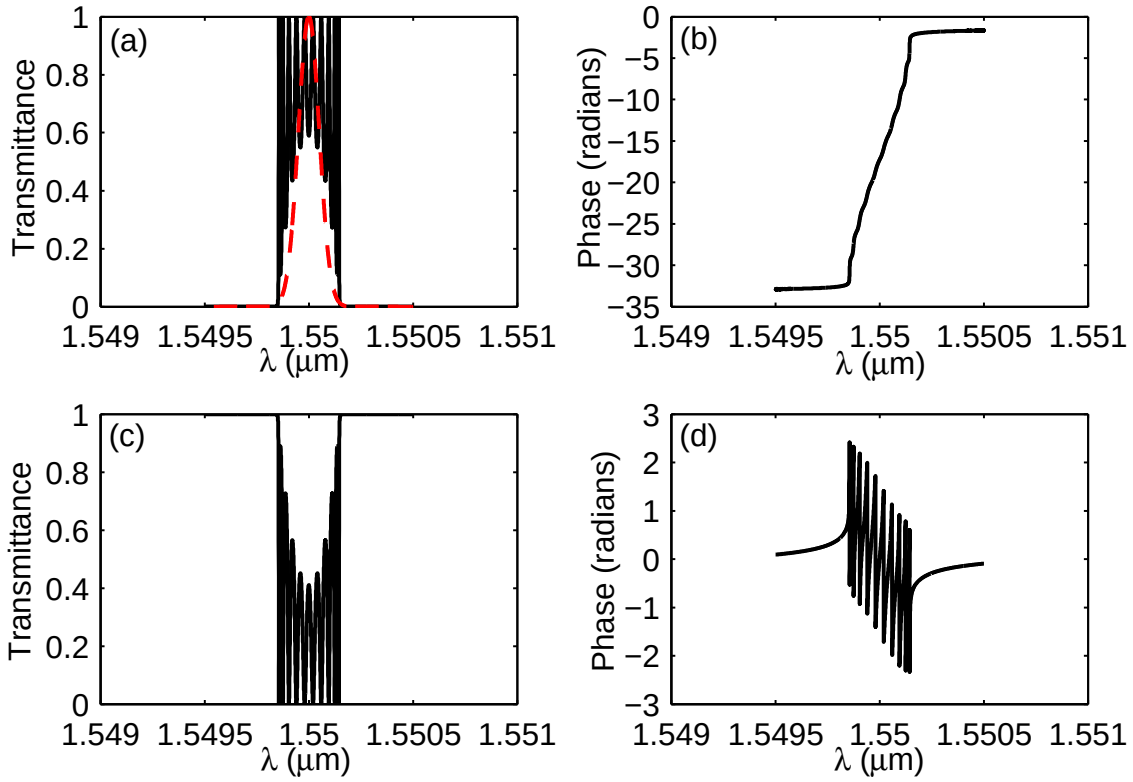

Figure 2.7: The transmission characteristics of a 10 ring long CROW. The ring radius is 164.5 μm and $n_{\text{eff}} = 1.5$. Inter-resonator coupling is $-0.3i$ and the waveguide-CROW coupling is $-0.5i$. A 30.5 ps (FWHM) long pulse centered at 1.55 μm is input into the CROW. (a) Transmittance at the drop port. The dashed line shows the spectrum of the input pulse. (b) Phase response at the drop port. (c) Transmittance at the through port. (d) Phase response at the through port.

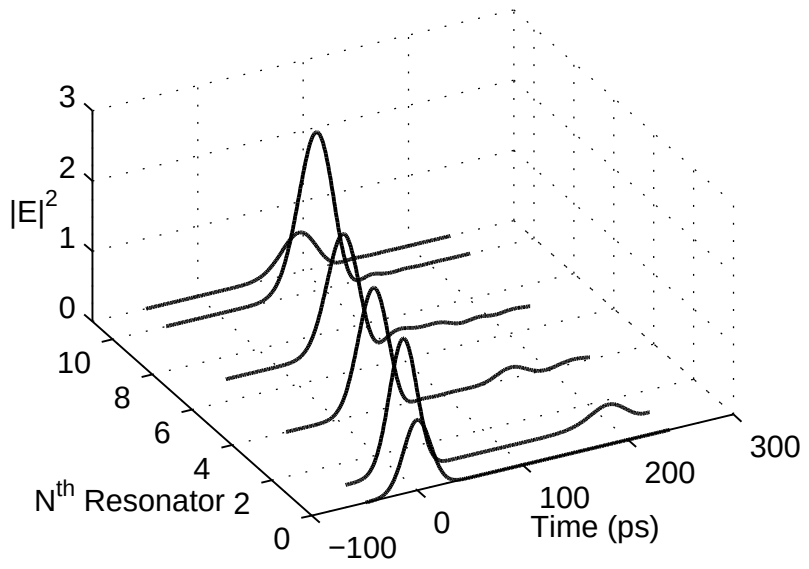

Figure 2.8: The pulse transmission through the CROW described in Fig. (2.7). The $0th$ resonator is the input pulse and the $11th$ resonator is the output pulse at the drop port.

to the input, the field intensity inside the rings can be greater than the input, as in the case of the semi-infinite CROW. The intensity build-up is verified by a FDTD simulation discussed in Section 5.3. The significant increase in the intensity of the input pulse inside the CROW can be used to enhance the strengths of nonlinear optical interactions. As noted earlier, we can account for loss (or gain) in our model by including an imaginary part to the propagation factor β. We have found the transfer matrices give excellent agreement with experimental results [40].

Another interesting effect is the small amplitude ripple that follows the main peak in each resonator. The ripple is travelling from the end of the CROW back to the start at approximately the group velocity of the forward moving pulse. This is analogous to a reflection from the end of a waveguide, though in the microring CROW described here there are no reflection mechanisms, as the coupling is assumed to be perfectly phase-matched. Indeed, Fig. 2.9 shows that the ripple at the through port is delayed from the the drop port pulse by the travelling time between the input and the drop. Therefore, although the microring CROW is composed of "microscopic," discrete elements, it possesses certain "macroscopic" properties that mimic conventional

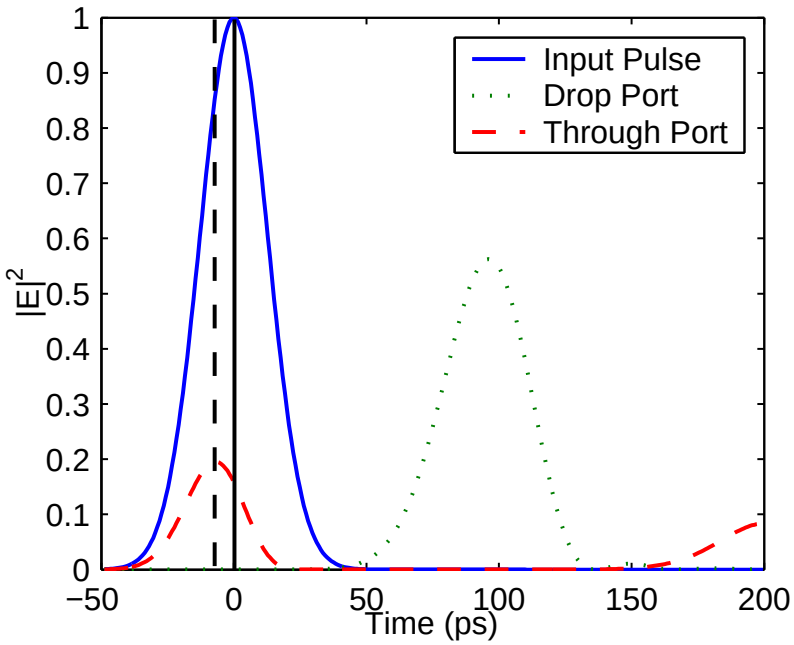

Figure 2.9: The input pulse and the output pulses at the drop and through ports of the the CROW described in Fig. 2.7. The solid vertical line marks the maximum of the input pulse, and the dashed vertical line marks the maximum of the output pulse at the through port. The peak of the through port pulse occurs about 5 ps sooner than the peak of the input.

waveguides.

At the through port, we may obtain negative group velocities, which some researchers refer to as "superluminal propagation" [28, 47]. In the time domain, the main (highest) peak of the output pulse does indeed appear before the peak of the input pulse. Fig. 2.9 shows the output pulses at the through and drop ports as well as in the input pulse. The peak of the through pulse is approximately 5 ps before the peak of the input, as though the output appears before the input. However, the pulse is attenuated and distorted. This behavior is accounted for by the anomalous dispersive properties at the through port in Fig. 2.7(d). The anomalous dispersion is also confirmed by the FDTD simulation discussed in the next section.

2.6.3 FDTD Simulations

As a test for the transfer matrix method and a confirmation of the intensity build-up and anomalous dispersion, we use a finite difference time domain (FDTD) simulation to study the pulse propagation through two coupled ring resonators. The waveguides and rings are 0.2 μm wide. They are set in air and have an index of refraction of 3.5. The rings have a radius of 5 μm, and the wavelength dependent effective index, as extrapolated from a separate FDTD simulation of the waveguides, is $n_{\text{eff}} = 3.617 - 0.5539\lambda$. The coupling between the rings is $-0.32i$, and the coupling between the rings and the waveguides is $-0.4i$. A 2.4 ps (FWHM) Gaussian pulse is launched into the system, and the fields at the through port, drop port, and inside the rings are monitored. We compare the transfer matrix method with the FDTD simulation in Fig. 2.10(a), showing that the approaches are in excellent agreement. The anomalous dispersion at the through port and the increase in intensity in the coupled rings are confirmed by the FDTD simulation and are evident in Fig. 2.10(b).

2.7 Photonic Crystal Defect and Fabry-Perot Cavities

Even though our derivations have been based on the example of ring resonators thus far, in this section, we shall consider how to generalize the ring resonator results to two other important classes of resonators: the photonic crystal defect and Fabry-Perot cavities. In contrast to ring resonators, the coupling between Fabry-Perot resonators with Bragg end mirrors is controlled by Bragg reflection. Even though the coupling coefficient may be more stringently controlled in these structures, ring resonators remain an attractive option for CROWs in planar integrated optical circuits because they can be fabricated in a single lithographic step. Moreover, recent developments in coupled ring resonators in polymer, silica, and silicon illustrate the potential of using ring resonators as constituent elements in CROWs [10, 48, 49].

Photonic crystal defect CROWs were first realized and measured by Olivier et al. several years ago [50]. Since the modes of photonic crystal defect cavities cannot be

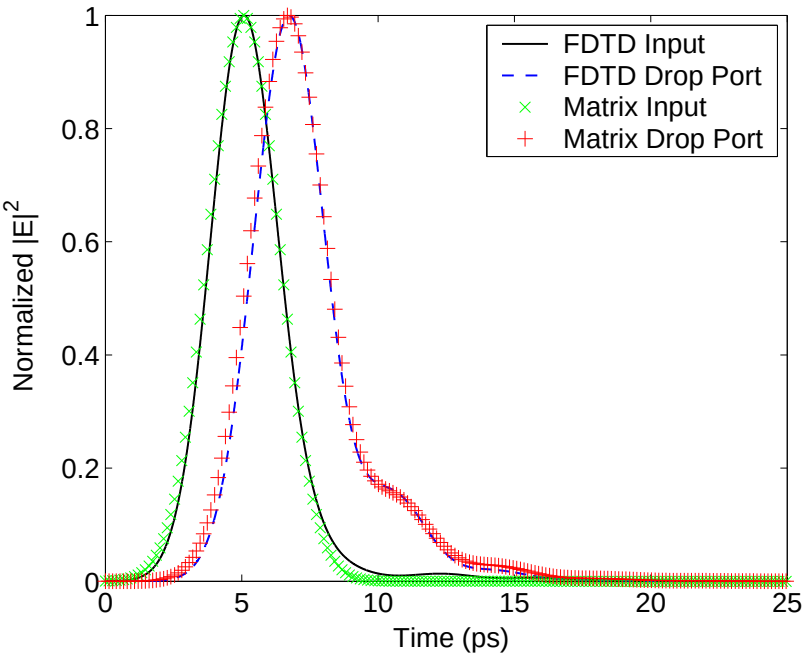

(a)

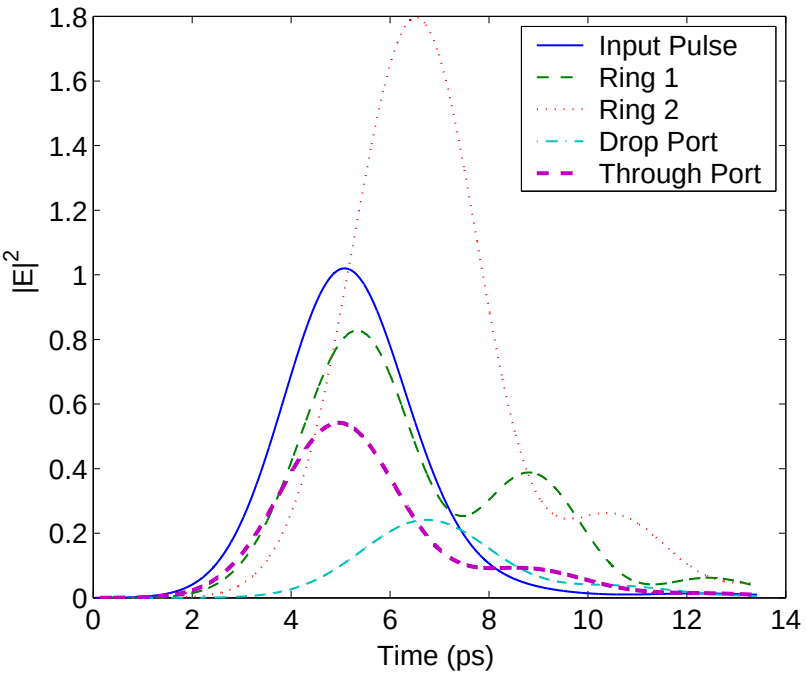

(b)

Figure 2.10: FDTD simulation of 2 coupled ring resonators with input and output waveguides. The radius of the rings is 5 μm, and the effective index is $n_{\text{eff}} = 3.617 - 0.5539\lambda$. The inter-resonator coupling is $-0.32i$ and the waveguide-resonator coupling is $-0.4i$. The input pulse is a 2.4 ps (FWHM) Gaussian centered at 1.55 μm. (a) Comparison between the FDTD simulation and the transfer matrix method. Output refers to the drop port. (b) Intensity build-up and anomalous dispersion as confirmed by the FDTD simulation.

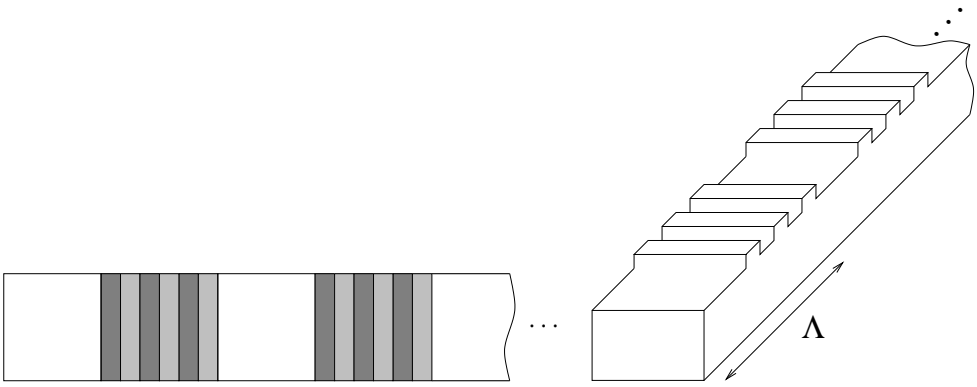

(a) Epitaxially grown. (b) Gratings on a waveguide.

Figure 2.11: Coupled Fabry-Perot cavities

readily decomposed into travelling plane waves, the analysis of coupled photonic crystal defect cavities using a transfer matrix method has been limited [51, 52]. However, because the temporal coupled-mode equations for the ring resonator and photonic crystal defect cavity CROWs are identical [36], the conclusions we draw from the ring resonator example hold for the latter case with $|\kappa|/(m\pi)$ replaced by κ_1 in the tight-binding dispersion relation Eq. (1.12).

The Fabry-Perot CROWs as in Fig. 2.11 can be analyzed in the same way as photonic crystal defect cavities or using transfer matrices. CROWs using Fabry-Perot etalons with Bragg end mirrors have also been explored recently [53]. There have also been extensive studies in the linear and nonlinear optical propagation in Bragg stacks [44, 54, 55, 56, 57, 58]. In Fabry-Perot resonators, the coupling parameter κ corresponds to the transmission coefficient, while t corresponds to the reflection coefficient. They can be calculated from the Fresnel coefficients or from an analysis of a Bragg stack in the case of a Fabry-Perot with Bragg end mirrors [44]. However, κ is generally complex, not imaginary in the case of phase-matched co-directional coupling as derived from coupled-mode theory [1, 44]. Moreover, because Fabry-Perot resonators are one dimensional, they can be completely described by 2×2 transfer matrices [44], in contrast to ring resonators which require a 4×4 transfer matrix to model the Bloch modes [34]. Therefore, there are only 2 Bloch modes at each frequency rather than 4 for the ring resonator CROW.

For a general complex coupling coefficient between the Fabry-Perot (1 dimensional) cavities, $\kappa = \kappa_0 \exp(i\theta)$, the dispersion relation becomes

$$\frac{\omega(K)}{\Omega} = 1 + \frac{(-1)^m \kappa_0}{m\pi} \left[\sin(K\Lambda - \theta)\right]. \tag{2.34}$$

The dispersion relation is of the same form as Eq. (2.11), but the $\pm$ sign is absent and θ could be arbitrarily specified depending on the nature of the coupling. While it does not significantly alter the general characteristics of a CROW, the presence of the phase shift modifies the phase velocity of the CROW Bloch modes. Nonetheless, the results discussed thus far for the ring CROW still holds for a chain of coupled linear resonators with πR replaced by L, the length of the cavity.

2.8 Summary

A transfer matrix method is developed to analyze microring coupled resonators. In the limit of weak coupling, the transfer matrix and tight-binding approaches yield equivalent dispersion relations, and the transfer matrix gives the same time domain field evolution equations as temporal coupled-mode theory. We also study pulse propagation through semi-infinite and finite CROWs to find the intensity enhancement as well as anomalous dispersion. The transfer matrix method can account for finite chains, holds for any coupling strength, applies to travelling waves, and can treat heterogeneous chains consisting of an arbitrary mix of resonators and coupling constants. These features make the transfer matrices versatile for device design and for analyzing experimental results of microring CROWs.

Chapter 3

Designing Coupled-Resonator Optical Waveguide Delay Lines

3.1 Introduction

With the theoretical framework we formulated in the last chapter, we will now proceed to address the design issues of slowing light and making delay lines with CROWs[1]. In particular, we will find there are fundamental trade-offs among delay, loss, and bandwidth. We shall derive simple, analytical expressions for the achievable delay, loss, bandwidth, and a figure of merit to compare delay line performance. Dispersion-related distortion in CROWs has been explored previously [21, 32], and how it limits the amount of slowing that can be achieved is discussed in [59]. We will compare CROW delay lines composed of ring resonators, toroid resonators, Fabry-Perot resonators, and photonic crystal defect cavities based on recent experimental results reported in the literature.

3.2 Delay, Loss, and Bandwidth

Using the dispersion relation Eq. (2.11) and the transfer matrices for the specific case of ring resonators, we now proceed to derive and verify the expressions that highlight the trade-offs among delay, bandwidth, and loss of a CROW. As discussed in Section 2.7, the results we obtain can be easily generalized to other common types

[1] ©2004 OSA. Reprinted, with permission, from [35].

of resonators. The immediate consequence of Eq. (2.11) is that the group velocity,

$$|v_g| \equiv \left|\frac{\partial\omega}{\partial K}\right| = \frac{2c}{n_{eff}\pi}\left|\kappa\sin(K\Lambda)\right|, \tag{3.1}$$

is dependent on the coupling coefficient $|\kappa|$. Since $|\kappa|$ can be controlled by the separation between adjacent resonators, we can in principle achieve arbitrarily large slowing down of optical pulses. The delay can also be controlled by changing the refractive index of the resonators or the coupling region through the electro-optic or thermo-optic effect [60, 61, 62, 63]. However, as $|\kappa|$ decreases, so does the bandwidth of the CROW, and the overall loss of the CROW becomes more sensitive to the intrinsic losses in the individual resonator. The latter occurs because the light spends more time in a resonator before "tunnelling" to its neighbor.

In the absence of other mechanisms to compensate for group velocity dispersion (GVD), such as Kerr nonlinearity [26, 27], an optical pulse propagating in a CROW should have a central frequency near the zero GVD region of the dispersion curve ($\frac{\partial^2 K}{\partial\omega^2} \approx 0$) to minimize the accumulated distortion. This condition occurs at the center frequency, $\omega \approx \Omega$, where the group velocity is maximum $v_{g,\max} = 2c|\kappa|/n_{eff}\pi$. From Eq. (2.11), a CROW band spans a frequency range of $\Delta\omega = 2c|\kappa|/n_{eff}\pi R$. Consequently, we define the usable bandwidth of a CROW as half of this total bandwidth centered at Ω,

$$\Delta\omega_{use} \equiv \frac{|\kappa|c}{\pi n_{eff}R}. \tag{3.2}$$

The periodicity, Λ is taken to be approximately equal to $2R$. Thus, the temporal delay of a pulse propagating through the whole length of the CROW is determined by the distance traversed in the CROW and the group velocity at Ω:

$$\tau = \frac{\pi n_{eff}RN}{|\kappa|c}. \tag{3.3}$$

From Eq. (3.3), we observe that the CROW effectively acts as conventional wave-

guide with a group velocity c/n_{eff} but with a length of

$$L_{\text{eff}} = \frac{c\tau}{n_{eff}} = \frac{\pi RN}{|\kappa|}, \tag{3.4}$$

i.e., $\sim 1/|\kappa|$ times longer than the CROW. Due to the reduced group velocity provided by the feedback amongst the coupled resonators, the total length of the CROW, $N\Lambda$, is contracted by a factor of $S = \frac{\pi}{2}|\kappa|$. S also represents the slowing factor of the group velocity $c/(n_{eff}v_{g,\max})$. The contraction in the spatial length also applies to a pulse propagating through the structure, such that a 100 ps pulse in a fiber, which has a spatial extent of $\sim$ 2 cm, contracts to a length of $\sim$ 3 mm in a CROW with $|\kappa| = 0.1$.

Furthermore, the loss from the input to the output of the CROW is intuitively given by the product of the loss per unit length and L_{eff}:

$$\alpha = \frac{a\pi RN}{|\kappa|} = \frac{2\pi n_{eff}N}{\lambda_0|\kappa|Q_{int}}, \tag{3.5}$$

where $\exp(-\alpha)$ is the net power attenuation coefficient of the CROW, $\exp(-a2\pi R)$ is the power attenuation in the waveguides of the constituent resonators, $\lambda_0 = 2\pi c/\Omega$, and Q_{int} is the intrinsic quality factor or Q factor of the resonator. Eqs. (3.2), (3.3), and (3.5) enable the straight-forward design of CROW delay lines.

If only a specific loss is tolerated, the maximal delay achievable is independent of $|\kappa|$. To illustrate this, we define the maximum tolerable loss as $\exp(-\alpha) = \exp(-1)$. Using Eqs. (3.5) and (3.3), we find that

$$\tau_{\max} = \frac{n_{eff}}{ca}. \tag{3.6}$$

This result makes intuitive sense since light must travel the same optical length to achieve a given delay. The role of the resonators is now clear: the weakly coupled resonators make this net length more compact.

To verify the simple and intuitive equations, Eqs. (3.2), (3.3), and (3.5), we compare the equations with numerical results obtained from the transfer matrices. In

Table 3.1: Coupling Constants Used in Fig. 3.2 for $N = 10$

$\lvert\kappa\rvert$	0.1	0.15	0.2	0.25	0.3	0.35
$\lvert\kappa_i\rvert$	0.43	0.55	0.6	0.65	0.7	0.75

coupled resonator filter synthesis, the coupling constants must be at particular ratios to avoid ripples in the passband which cause significant deviations from the ideal, infinite CROW characteristics [5, 11, 64]. For a maximally flat transfer function, the inter-resonator couplings are not constant throughout the structure [5, 65, 64]; hence, Eqs. (3.2), (3.3), and (3.5) do not strictly apply. However, we may still obtain fairly flat transfer functions over $\Delta\omega_{use}$ by having a single inter-resonator coupling constant, κ, and a different waveguide-resonator coupling, κ_i. Fig. 3.1 shows the passband spectra for a finite CROW with a single κ and a different κ_i. As shown in Fig. 3.1, we find that one pair of κ and κ_i is sufficient to obtain flat transmission spectrum over a large range in the number of resonators. The flat responses enable us to use finite structures to mimic an infinitely long CROW characterized by a single coupling constant.

Therefore, using the parameters in Table 3.1 when N is fixed to be 10 and κ is varied, and setting $\kappa_i = -0.43i$ and $\kappa = -0.1i$ when N is varied, we compare Eqs. (3.2), (3.3), and (3.5) with the calculations from the transfer matrices. As shown in Fig. 3.2, the expressions are in excellent agreement with the numerical calculations. In the plots of the delay times, the theoretical results as indicated by the solid lines coincide best with the data points corresponding to slight waveguide losses ($\sim$ 4 dB/cm). This occurs because the losses smooth out the transmission spectrum ripples, making the passband of the finite CROW a better approximation to an infinitely long CROW.

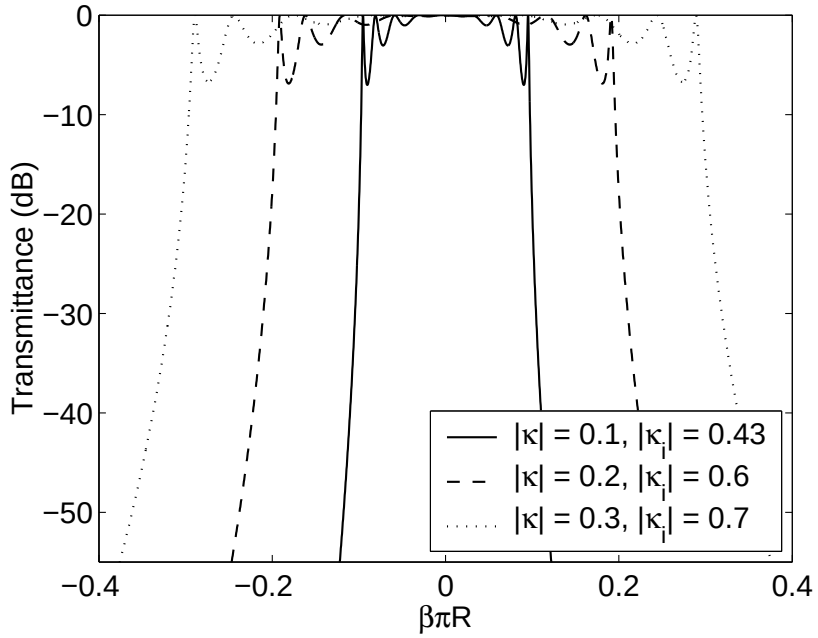

(a) N=10

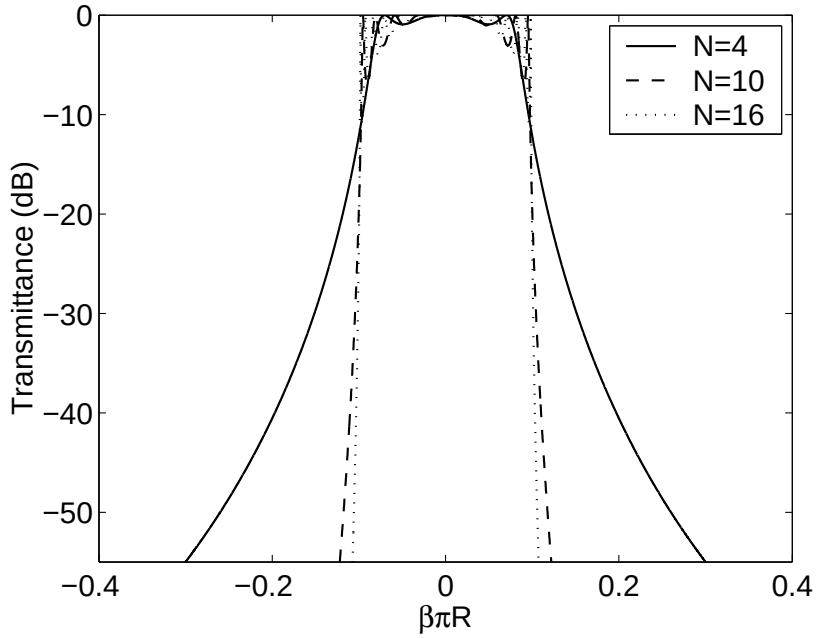

(b) $|\kappa| = 0.1$, $|\kappa_i| = 0.43$

Figure 3.1: Passbands of coupled resonator structures with an identical inter-resonator coupling $|\kappa|$ throughout and a different waveguide-resonator coupling $|\kappa_i|$. (a): The number of resonators is fixed and the coupling constants are varied. (b): The coupling constants are fixed and N is varied.

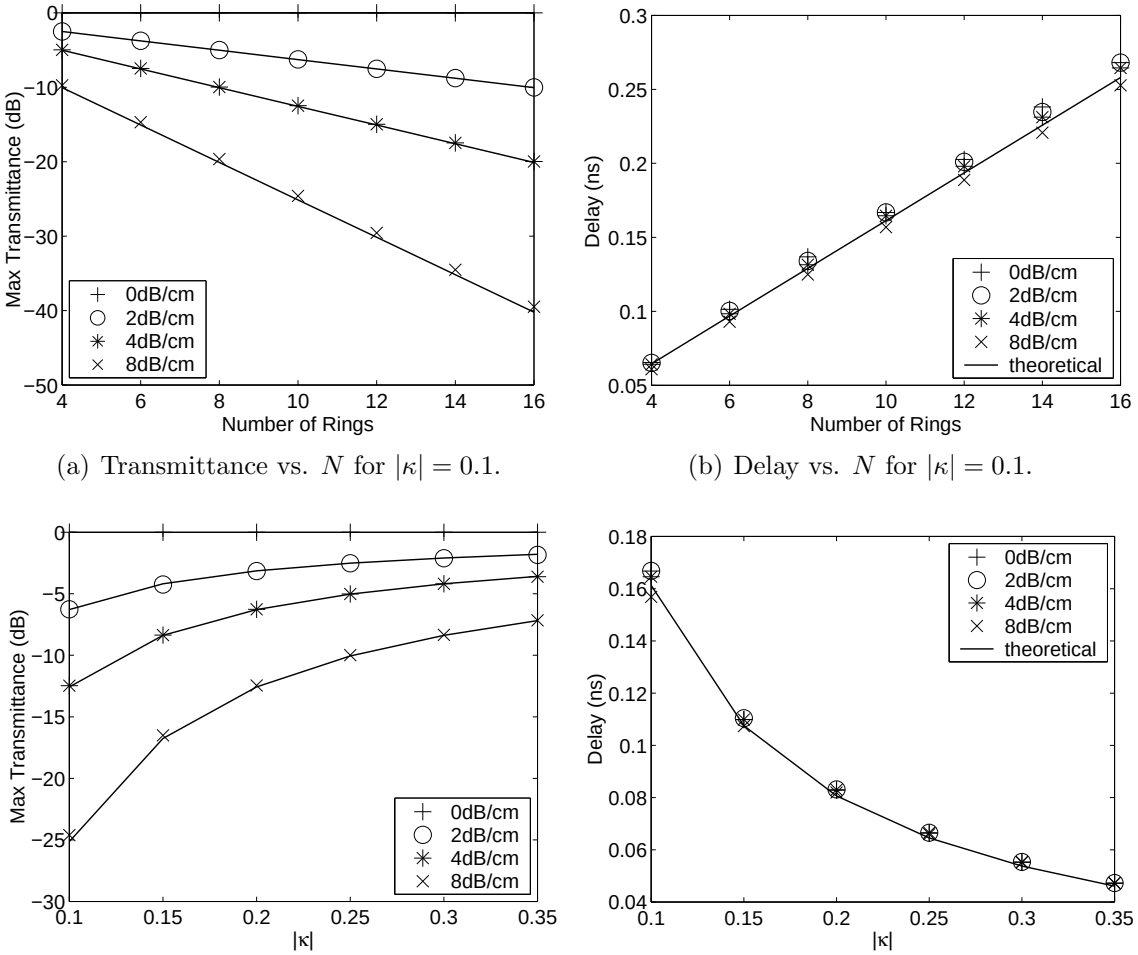

(a) Transmittance vs. N for $|\kappa| = 0.1$.

(b) Delay vs. N for $|\kappa| = 0.1$.

(c) Transmittance vs. $|\kappa|$ for $N = 10$.

(d) Delay vs. $|\kappa|$ for $N = 10$.

Figure 3.2: Comparing analytical expressions for loss and delay with numerical results using the transfer matrices for various propagation losses in the resonators. The solid lines are the theoretical results and the markers denote the numerical results. $R = 100$ μm and $n_{eff} = 1.54$.

3.3 A Figure of Merit

To compare CROW delay lines composed in a general way independent of material systems and resonator sizes, we need a quantitative benchmark to determine the quality of a delay line. While $\tau_{\max}$ is a useful criterion, it does not account for the usable bandwidth. An alternative approach is to compare the intrinsic and coupling losses in the resonators. The intrinsic losses of each resonator due to absorption and scattering are characterized by a time T_{int}. The decay of resonator power due to coupling to adjacent neighbors is characterized by T_{ext} and the associated Q factor, $Q_{ext} = \Omega T_{ext}$.

$|T_{ext}|$, from Eq. (2.20), naturally defines the characteristic lifetime of the excitation due to the coupling, since it sets the temporal width of the field in the initially excited resonator. It is also the time required for a pulse centered at Ω to transverse a single resonator, i.e., $|T_{ext}| = \Lambda / v_{g,\max}$. At $t = |T_{ext}|$, the energy at the zeroth resonator will have decayed to $|J_0(1)|^2 \approx 0.59$ of the original value.

To be useful as a delay line, $T_{ext} \ll T_{int}$, or equivalently, $Q_{ext} \ll Q_{int}$. Therefore, a useful figure of merit for CROW delay lines is

$$\text{FOM} \equiv \frac{Q_{int}}{Q_{ext}}. \tag{3.7}$$

The figure of merit is also useful for other resonator-based devices or geometries for comparing the relative role of Q_{int} and Q_{ext}, for example in the determination of the loaded Q, $1/Q_L = 1/Q_{int} + 1/Q_{ext}$.

Substituting $|T_{ext}| = \frac{\Lambda n_{eff} \pi}{2|\kappa| c}$ from Eq. (2.20) into $Q_{ext} = \Omega |T_{ext}|$, we find

$$Q_{ext} = \frac{\pi^2 n_{eff} \Lambda}{\lambda_0 |\kappa|}. \tag{3.8}$$

The figure of merit (3.7), in turn, simplifies to

$$\text{FOM} = \frac{|\kappa|}{a\pi R} = \frac{\Delta\omega_{use}\tau}{\alpha_{tot}} = \tau_{\max}\Delta\omega_{use}. \tag{3.9}$$

The second equality reveals that the FOM can be alternatively viewed as a balancing of bandwidth, loss, and delay.

3.4 Comparing Different Resonators

Table 3.2 compares 10 resonator long delay lines with $|\kappa| = 0.1$ (1% power coupling) composed of various types of resonators in different material systems at 1.55 μm. We assume n_{eff} is independent of frequency. The results emphasize the trade-offs between delay and bandwidth. For the semiconductor, polymer, and Hydex^{TM} ring resonators, and the photonic crystal cavities, we use some of the highest reported experimental Q_{int} values of a single, passive resonator in the literature to date and their corresponding resonator sizes [10, 12, 66, 67, 68, 69].

A particular issue with ultra-high Q resonators is that excess coupling losses may become dominant over the intrinsic resonator Q. The source of the excess coupling loss is that the neighboring resonators act as a dielectric perturbation to an individual resonator. In the ring microresonators with lower Q_{int} values, bending and scattering losses typically predominate [71]. Since the coupling is assumed to be lossless in our analysis, the excess loss of the coupler should be accounted for by the loss of the resonator. Therefore, for a fiber ring resonator, in which material, bending, and splice losses are negligible, the loss in calculating the Q factor in Table 3.2 is taken to be the excess loss of a commercial fused fiber coupler (~ 0.2 dB [72]).

As there are no reported excess coupling loss values for ultra-high Q toroid resonators to date, we neglect this effect in Table 3.2 and simply use the highest reported intrinsic Q value ($Q_{int} \approx 10^8$) of a single resonator [9, 73]. Extrapolating from this Q value, the loss per revolution inside the toroid resonator is about 10^{-4} dB. For excess coupling loss to be negligible, it must be $\ll 10^{-4}$ dB. Even for an excess coupling loss of 0.01 dB, the Q value in our comparison drops to 10^6, the net loss increases to 0.5 dB, τ_{max} becomes 0.82 ns, and the figure of merit is reduced to 90. However, the coupling between a fiber-taper and an ultra-high Q silica microsphere has been experimentally shown to be nearly ($> 99.97\%$) lossless [74]; therefore, the coupling of

Table 3.2: Comparison of CROW Delay Lines Consisting of $N = 10$ Resonators for $|\kappa| = 0.1$

Resonator	$\mathbf{Q_{int}}$	**Net Loss**	**Delay**	**Bandwidth**	$\tau_{\max}$	**FOM**
III-V Semiconductor Ring [66] ($n_{eff} \sim 3, R \sim 10$ μm)	5000	33 dB	31 ps	51 GHz	4 ps	1.3
Polymer Ring [12] ($n_{eff} \sim 1.57, R \sim 32$ μm)	2.4×10^4	12 dB	53 ps	30 GHz	20 ps	3.8
Silicon Ring [69] ($n_{eff} \sim 2.58, R \sim 20$ μm)	1.4×10^5	2 dB	54 ps	30 GHz	114 ps	21.2
Hydex$^{\text{TM}}$ Ring [70] ($n_{eff} \sim 1.6, R = 40$ μm)	4×10^5	0.9 dB	67 ps	24 GHz	329 ps	49
Fiber Ring[a] ($n_{eff} = 1.45, R = 10$ cm)	8×10^7	10 dB	152 ns	11 MHz	66 ns	4.3
Silica Toroid[b] [9] ($n_{eff} \sim 1.45, R = 60$ μm)	10^8	5×10^{-3} dB	91 ps	17 GHz	82 ns	9026
Semiconductor Fabry-Perot ($n_{eff} \sim 3, L = 30$ μm)	2×10^6	0.06 dB	30 ps	53 GHz	2.2 ns	724
Photonic Crystal Defect [67, 68] ($\kappa_1 = 2 \times 10^{-4}$)	4.5×10^4	5 dB	41 ps	39 GHz	37 ps	9

[a] Includes excess coupling losses.
[b] Neglects excess coupling losses.

toroid resonators may be nearly ideal as well.

CROWs based on Fabry-Perot cavities have been recently demonstrated [53], with an operational wavelength around 600 nm. The coupling between Fabry-Perot resonators can be controlled by Bragg reflection. Hence, to compare this structure with the ring resonators where the coupling is due to evanescent decay of the field outside the resonator, the resonator Q of the coupled Fabry-Perot structure is not taken as the Q of the composite structure of the cavity and Bragg layers, but rather the cavity by itself. The loss is thus determined by material and waveguide loss, which is taken to be 0.2 dB/cm for the comparison, assuming that the Bragg gratings are etched on a waveguide. The losses at the coupling regions are ignored.

Experimental progress in photonic crystal coupled cavity structures has been burgeoning over the past few years [23, 36, 50, 75, 76, 77]. To compare photonic crystal defect cavity CROWs with the ring and Fabry-Perot resonators, κ_1 is taken to be 2×10^{-4}, which is approximately equal to the value of $|\kappa|c/(n_{eff}\pi R)$ for the other integrated optical resonators considered.

3.5 Discussion

As evidenced by the comparison in Table 3.2, application requirements, such as on the loss, bandwidth, and material system, dictate the type of resonator that will be the most suitable. To achieve long delays without too much attenuation, low-loss (high-Q) resonators are required. High-Q resonators also allow for more flexibility in the design since the CROW can be made longer with a higher coupling coefficient to increase the bandwidth without incurring a severely detrimental effect on the loss. For our example of $|\kappa| = 0.1$ and cavity lengths of tens of microns, for substantial delay with an attenuation of circa 10 dB, Q values of 10^5–10^6 are necessary.

Although the use of ultra-high-Q resonators for a CROW is an attractive option, there have not been many reported experimental demonstrations of coupling more than a few of these resonators together [78]. Moreover, thus far, there have not been extensive attempts to integrate these types of resonators with other planar

components. Therefore, with the technological and experimental progress to date, a more practical approach may be to use resonators with lower Q values as the constituent elements of a CROW.

CROWs consisting of ring resonators and Fabry-Perot resonators are promising. Fabry-Perot cavities have the advantage that the coupling can be precisely controlled by Bragg reflection. However, Fabry-Perot resonators fabricated by epitaxial growth or thin film deposition cannot be readily integrated with planar technologies. A lithographically defined grating on a waveguide requires a multi-step fabrication process already well exploited in distributed feedback (DFB) and distributed Bragg reflector (DBR) structures.

Even though the patterning of gratings is well established, the option of ring resonators should not be neglected. Ring resonators are more compact than a linear chain of Fabry-Perot resonators and can be fabricated in planar integrated lightwave circuits in a single lithographic step in the case of horizontal coupling. Recently, loss-compensated ring resonators in InP-InGaAsP have been reported [79], thus a lossless or even amplifying microring CROW may be feasible. Since CROWs are typically narrow band devices, even slight deviations in resonator sizes will alter the passband spectrum in the form of the Vernier effect [64, 11]. To achieve ideal device behavior, post-fabrication tuning of the resonators through UV trimming [80, 81], the thermo-optic effect [82],or the electro-optic effect [12] maybe required. However, there have already been impressive demonstrations of flat passband, low-loss, high-order coupled microring resonator filters [10, 48, 49], illustrating that coupled ring resonator may indeed be a viable technology. Advances in the fabrication of ring resonators will continue to enable passive and active ring resonator CROW delay lines in integrated optics.

3.6 Summary

We have addressed a number of key issues in designing CROW delay lines made of ring resonators. The achievable delay, available bandwidth, and loss are given by

simple, analytical expressions that are in excellent agreement with numerical results from the transfer matrix method. We have proposed a figure of merit to compare different CROW delay lines that is a ratio between the lifetime of an individual resonator and the lifetime due to resonator coupling. This comparison offers an easy and quick gauge in determining the feasibility of and the minimum intrinsic resonator Q necessary for a CROW delay line. We examined experimental progress in optical resonators to find that CROW delay lines with bandwidths of ~ 50 GHz and delays of the order of 100 ps should be feasible with current technologies.

Chapter 4

Polymer Microring Resonators

4.1 Introduction

In this chapter, we present an introduction to optical polymer materials and several demonstrations of optical notch filters based on a single microring resonator. We shall discuss the fabrication of polymeric microring resonator notch filters using combinations of electron-beam and soft imprint lithography[1]. Moreover, we shall present a simple and effective method for the post-fabrication trimming of microresonators by photobleaching chromophores in an optical polymer[2]. Since in the absence of any means to modify the resonators, fabrication resolution of the order of tens of nanometers is required to achieve a particular resonance frequency or coupling ratio, for many practical applications, post-fabrication trimming or tuning of the resonators is desired or required.

Ring resonator notch filters in three different material systems will be presented: polystyrene (PS) on OG-125, SU-8 on OG-125, and CLD-1 in amorphous polycarbonate (APC) on silica. Intrinsic Q factors as high as 2.6×10^4 were measured, and the maximum extinction ratio of the filters was -35 dB, indicating the critical coupling condition was satisfied.

[1] ©2004 IEEE. Reprinted, with permission, from [83].
[2] ©2004 OSA. Reprinted, with permission, from [84].

4.2 Polymer Materials

In recent years, polymeric waveguide devices, including microring resonators, have attracted much attention due to potentially low material and production costs [85]. Furthermore, the development of low-loss and optically nonlinear polymers is enabling the realization of both passive and active polymeric optical devices [86, 87]. In particular, polymers provide a promising material platform for the fabrication of microring resonators since many tuning mechanisms are available. For example, Rabiei et al. have recently demonstrated electro-optic and thermo-optic tuning of microring resonators [12, 60]. UV trimming of ring resonators using polymers has also been demonstrated by changing the refractive index of a polymer cladding layer [80, 88].

Table 4.1 compares a number of different material systems used for lightwave circuits [89]. The quoted waveguide losses depend very much on the dimensions of the waveguides and the index contrast and should only be taken as approximate values. Table 4.2 lists some of the polymers that were investigated during the course of this thesis work. As summarized in the tables, polymers possess a wide-range of optical properties and can be processed with a large variety of techniques. The current major limitation of polymer materials is the difficulty in incorporating electrically pumped optical gain at the telecommunication wavelengths. Therefore, III-V compound semiconductors remain the workhorse material of choice for lasers and active photonic circuits.

Through an appropriate combination of polymers, we can tailor the dispersive properties of the waveguides given a particular dimension. Table 4.3 gives the effective and group indices of several combinations of polymers for a specific single-mode waveguide cross-section described in the table. The residue thickness corresponds to the layer of core material that is left on top of the cladding after an imprint lithography step (to be discussed in Sections 4.4 and 4.5). The higher refractive index material is the waveguide core, and the lower index is the cladding. Since most polymers do not possess a large refractive index, polymeric waveguides typically possess effective and group indices of approximately 1.4–1.7.

Table 4.1: Comparison of Material Systems for Lightwave Circuits at $\lambda = 1550$ nm

Material	**R.I.**	**WG Loss (dB/cm)**	**Fabrication**	**Tuning Methods**	**Optical Gain**
Polymer	1.3–1.7	< 0.1–5	direct photo, electron-beam, imprint lithography, or dry etch	TO, EO, photobleach, photochromic	Er-doped, quantum dots, optically pumped (research phase)
Silica [90]	1.4–1.7	< 0.1	lithography and etch, or direct laser writing	TO, UV exposure	Er-doped, optically pumped
Silicon Nitride [91, 92]	2.0–2.5	1.5–3	lithography and etch	TO	
Lithium niobate [93]	2.2	0.15	proton exchange, or ion implantation	EO	Parametric amplification
Silicon [94]	3.48	< 0.2	lithography and etch	TO, FC	Raman, Er-doped, nanocrystals, optically pumped, III-V wafer bond (research phase)
III-V Semiconductors [95]	3.2–3.5	1	lithography and etch	TO, FC	Quantum dots/wires/wells, electrically or optically pumped

R.I. = refractive index, WG Loss = waveguide loss, TO = thermo-optic, EO = electro-optic, FC = free-carrier injection

Table 4.2: A Selection of Polymers Investigated

Material	**Vendor/ Source**	**Index (1550nm)**	**Type**	**Processing Notes**
APC/CLD-1	U. Washington	1.61	guest-host	CLD-1 is an EO chromophore; dry-etchable
APC	Sigma-Aldrich	1.53	polycarbonate	polymer, dry-etchable
PS	Sigma-Aldrich	1.59	polystyrene	polymer, dry-etchable
SU-8	Microchem	1.56	epoxy	negative photo- or electron-beam resist
Cyclotene	Dow Corning	1.54	benzocyclobutene	planarization polymer, photo-resist, dry-etchable
PDMS	GE	varies	siloxane	thermally curable, UV curable formulations
UV-15	Masterbond	1.504	epoxy	UV curable
PMMA	Microchem	1.47	acrylate	positive electron-beam resist, dry-etchable
OG-125	Epotek	1.465	epoxy	UV curable
OG-134	Epotek	1.42	epoxy	UV curable
WR-513	Luvantix	1.50	partially fluorinated	UV curable
Cytop	Asahi Glass	1.34	fluoropolymer	thermally curable, dry-etchable
Teflon	Dupont	1.3	fluoropolymer	polymer
FOx	Dow Corning	1.44	spin-on glass	thermally and e-beam curable
PI	HD Microsystems	1.5–1.65	polyimide	thermally and UV curable

Table 4.3: Waveguide Dispersion in Selected Examples of Polymer Waveguides

Material System	$\delta \mathbf{n}/\mu\mathrm{m}^{\dagger}$	$\mathbf{n_{eff}}$	$\mathbf{n_g}$
SU-8 in OG-125	-0.04	1.514	1.6
PS in air	-0.0622	1.529	1.677
APC/CLD1 in air	-0.0733	1.531	1.7

†The waveguide cross-section is 1.6 μm $\times$ 1.8 μm with a 200 nm thick residue layer.

A fabrication technique that is important for polymer materials is replica molding. In replica molding, a mold of the original master device is used to cast nearly exact copies of the master. This technique allows for high-throughput replication of the master device, and unlike other wet-etch or chemical processes, it does not chemically or physically alter any dopant molecules that may be in the polymer.

In the work described in this chapter, we used soft lithography replica molding to fabricate the microring resonators. Soft lithography is a particular technique in imprint lithography where the mold is flexible [96]. In our work, the soft mold is fabricated from a silicone rubber material, poly(di-methylsiloxane) (PDMS). The PDMS molds are highly robust, and the same molds can be used repeatedly for different polymers. We have previously shown that very high fidelity between the master and molded devices can be achieved using soft lithography molding [97]. This technique has been used to fabricate polymeric Mach-Zehnder modulators and toroid resonators [73, 98].

4.3 Microring Notch Filter and Critical Coupling

Before discussing the experimental results, we shall briefly describe the microring resonator geometry. We investigated microring resonator notch filters consisting of a single resonator coupled to a waveguide as shown in Fig. 4.1. Using the notation in Fig. 4.1, the coupling between the microring and the waveguide can be described by

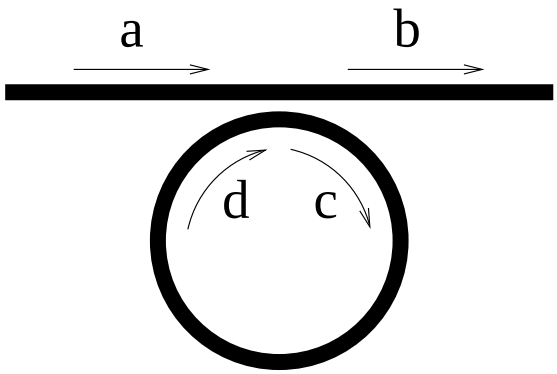

Figure 4.1: A microring resonator coupled to a waveguide. The field amplitudes are denoted by a, b, c, and d.

the matrix equation: [11, 37, 43]

$$\begin{bmatrix} b \\ c \end{bmatrix} = \begin{bmatrix} t & \kappa \\ -\kappa^* & t^* \end{bmatrix} \begin{bmatrix} a \\ d \end{bmatrix}, \tag{4.1}$$

where κ is the dimensionless length-integrated coupling coefficient and $|\kappa|^2 + |t|^2 = 1$. As the field propagates in the ring, it accumulates a phase shift and may be attenuated, so $d = \alpha c \exp(-i2\pi\beta R)$, where α is the field attenuation constant, R is the ring radius, and β is the propagation constant in the ring. Hence, the transfer function of the filter is described by [99, 100]

$$\left|\frac{b}{a}\right|^2 = \frac{|t|^2 - 2\alpha|t|\cos(2\beta\pi R) + \alpha^2}{1 - 2\alpha|t|\cos(2\beta\pi R) + \alpha^2|t|^2}. \tag{4.2}$$

In general, since α and $|t|$ in Eq. (4.2) are interchangeable, Q_{int} and Q_{ext} cannot be uniquely determined from the spectral response of the device. However, when the special condition $\alpha = |t|$ is satisfied, or alternatively when the internal power loss is equal to the coupling ($1 - \alpha^2 = |\kappa|^2$), $Q_i = Q_{ext} = 2Q_L$. This condition is known as critical coupling [100]. At critical coupling, the transfer function completely vanishes at the resonance frequencies of the ring resonator. Therefore, not only do critically coupled ring resonators allow us to unambiguously determine the intrinsic losses of a resonator through a single measurement of the spectral response of the geometry in

Fig. 4.1, they also enable optical notch filters with high extinction ratios.

4.4 Polystyrene and SU-8 Microrings

First, we shall discuss our results on unclad and clad microring resonators in the geometry of Fig. 4.1 fabricated in polystyrene (PS, $n \simeq 1.56$) and SU-8 (Microchem, $n \simeq 1.56$). The two examples corroborate the theoretical transmission spectrum described by Eq. (4.2) and illustrate the phenomenon of critical coupling.

4.4.1 Fabrication

Fig. 4.2 shows the schematic flow chart of the fabrication process. For this experiment, we created the PDMS mold from the master devices which were defined using electron-beam writing of SU-8. Fig. 4.3 shows a scanning electron microscope (SEM) image of the coupler region in the master device. The waveguides in the master devices had a height of 1.5 μm and a width of 1.9 μm. The resonator-waveguide gap size was about 350 nm.

We began the fabrication of the molded devices by spinning on a silicon wafer a 3 μm thick layer of OG-125 (Epotek, $n \approx 1.456$), an ultra-violet (UV) curable epoxy, as the under-cladding. The chip was then cured with UV light and baked at 80^0C for 2 mins. For the unclad microrings, we deposited 10 μL of PS solution (4wt% in toluene) on the chip and pressed the mold against the chip with a force of 25 N for about 20 minutes. The toluene evaporated through the PDMS mold during this time. Even though our molding process left behind a thin ($\sim$ 200 nm) residue film on the chip, this film is not detrimental on the loss of the devices if it is sufficiently thin [101]. After the mold was lifted away, the chip was baked at 80^0C for 3–5 mins. Finally, the chip was cleaved to separate the devices. The deviation in the radius of the molded and master devices was about 2%. The radius of the master was 200 μm, and the radius of the molded resonator was about 204 μm.

Fig. 4.4 shows an SEM image of the PS microring resonator. The slight uneven-

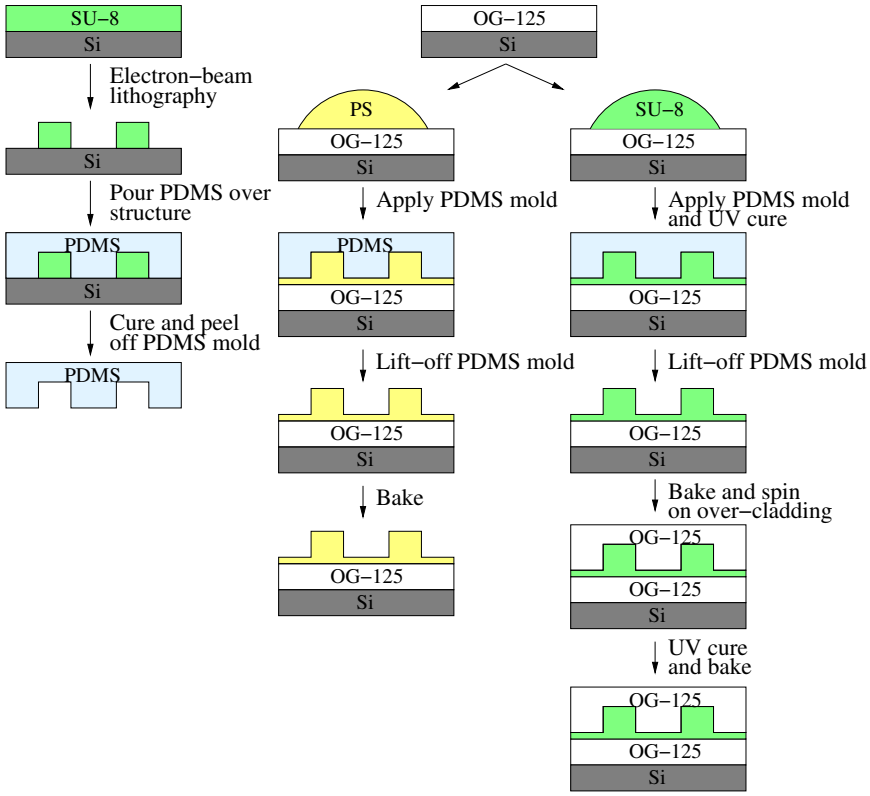

Figure 4.2: Fabrication process for the microring resonators. The leftmost column shows the fabrication of the soft PDMS mold. The center column shows the fabrication of the PS microring resonators. The rightmost column shows the fabrication of the SU-8 microring resonators.

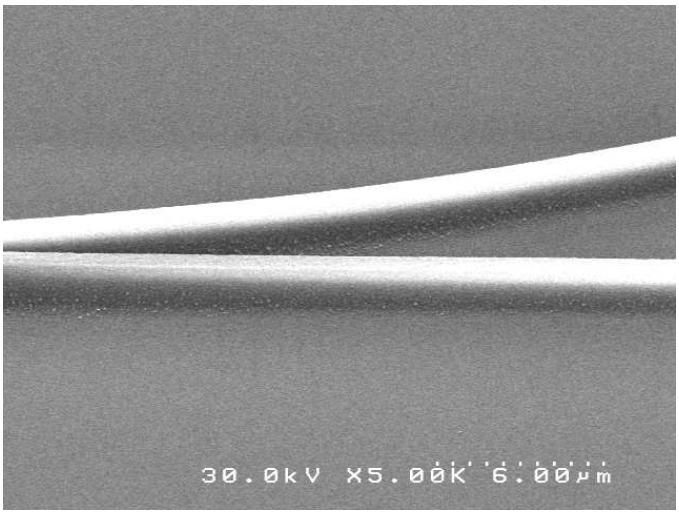

Figure 4.3: SEM image of the coupler region in the master device which was defined via electron-beam writing of SU-8

ness at the base of the waveguides was replicated from the master device and is caused by the electron-beam lithography fabrication process.

The fabrication process of the clad SU-8 resonator filters was similar to that of the PS microrings. The only differences were that the SU-8 must be UV-cured to harden and an over-cladding was applied. After the SU-8 was UV-cured, the chip was baked at 80^0C for about 3 minutes. An extra 3 μm layer of OG-125 was subsequently applied as the over-cladding. After the second application of OG-125, the chip was UV-cured again and finally baked at 80^0C for 3–5 mins.

4.4.2 Transmission Spectra

We measured the spectral response of the fabricated devices by coupling light from a tunable laser to the waveguide via a fiber taper and collecting the transmitted light through a lens (see Fig. 4.7). Fig. 4.5 shows the transmission spectra for the PS and SU-8 microring resonator filters for transverse electric (TE) polarized light. The PS and SU-8 devices had maximum extinction ratios of -12 dB and -20 dB respectively, illustrating that the critical coupling condition was essentially satisfied. The PS resonators had a FSR of 1.15 nm and a 3 dB bandwidth of 0.3 nm, and hence a finesse of 3.8. The SU-8 microrings had a FSR of 1.2nm, a 3dB bandwidth of 0.436 nm, and a finesse of 2.75. By taking the ratio between the resonance wavelength and the FWHM linewidth of the resonance, Q_L factors were found to be approximately 5200 and 3555 for the PS and SU-8 microrings respectively. These quality factors implied that Q_{int} were 1.0×10^4 and 7.1×10^3.

We also fitted the experimental data with the theoretical response described by Eq. (4.2) to find excellent agreement between them. The fit parameters for the PS microring were α(or t)= 0.689, t(or α)= 0.620, and the group index, n_g, was 1.624. The fit parameters for the SU-8 microrings were $\alpha = t = 0.536$ and $n_g = 1.562$. Extrapolating the Q factors from the attenuation in the microring resonator, we find that $Q_{int} = 1.1 \times 10^4$ for the PS microring and $Q_{int} = 6.5 \times 10^3$ for the SU-8 microring. These values implied a distributed loss of about 25 dB/cm in the resonator.

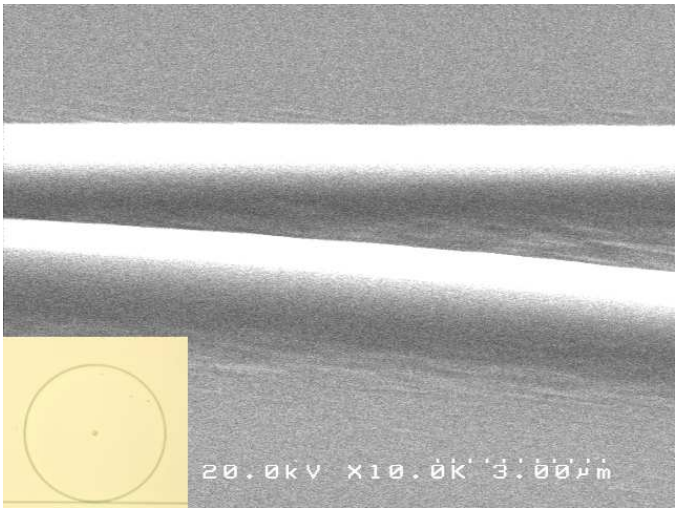

(a)

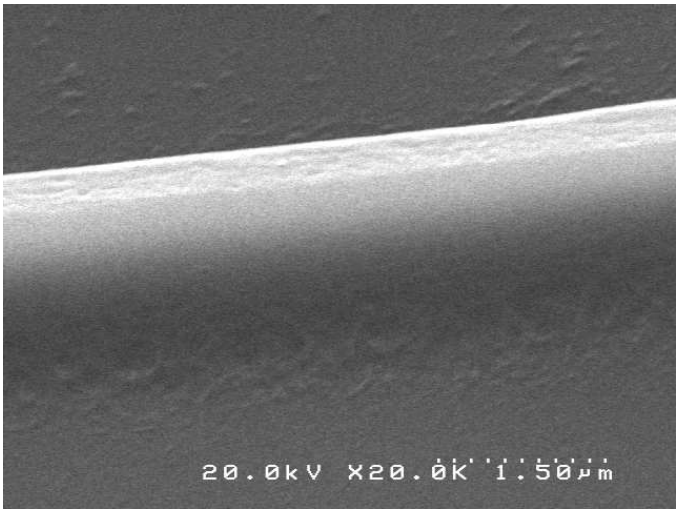

(b)

Figure 4.4: SEM images of (a) the resonator-waveguide coupling region and (b) a section of waveguide in polystyrene. Smooth side-walls are achieved using the soft lithography fabrication process. Inset of (a): An optical micrograph of the microring resonator filter

The Q factors were in good agreement with the direct measurements of the resonance linewidths.

For the microring radius and refractive index contrast in this experiment, we expected that the resonator loss would be dominated by the side-wall scattering ($\sim$ 15–20 dB/cm) and material losses ($\sim$ 5 dB/cm) rather than the bend loss [12, 102, 103]. Therefore, resonators with larger FSRs and similar Q factors can be achieved by reducing the radius.

To determine the total insertion loss of the devices, we measured the difference between the transmitted powers with and without the microring resonator devices in our experimental setup. The total off-resonance insertion losses were found to be 6.7 dB and 9.9 dB for the PS and SU-8 microring resonator filters respectively. The coupling efficiency can be improved by designing a suitable mode-converter between the fiber and our device.

4.5 CLD-1/APC Microrings

Often it is necessary to trim microresonators to tune their resonance wavelength or coupling characteristics. In this section, we describe a simple and fast method to trim high-Q, critically coupled polymer microring resonators. Again using the soft-lithography replica molding method, we fabricated microring notch filters in a polymer doped with a nonlinear electro-optic chromophore, CLD-1 [86, 104]. The trimming was accomplished by photobleaching the CLD-1 chromophores. Photobleaching of electro-optic chromophores has been previously used to tune the splitting ratio of a Y-junction and has also been used to fabricate polymer waveguides [105, 106, 107]. However, the photobleach trimming of microring resonators, which is a sensitive process and of importance in microresonator technology, has not been previously demonstrated.

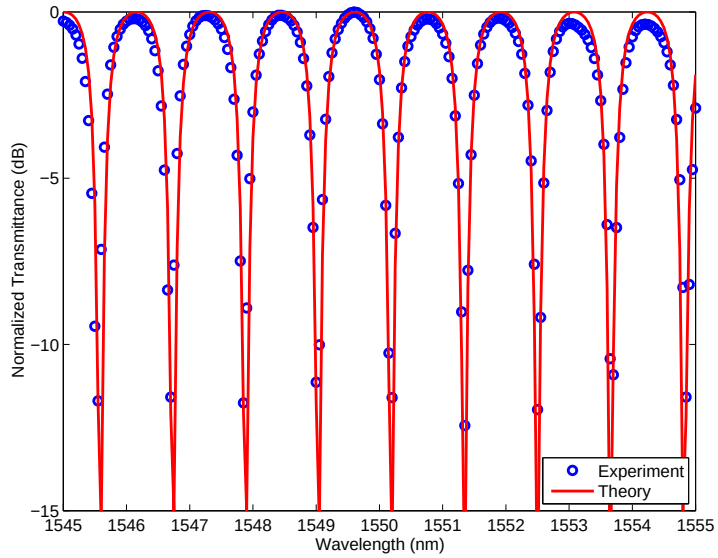

(a)

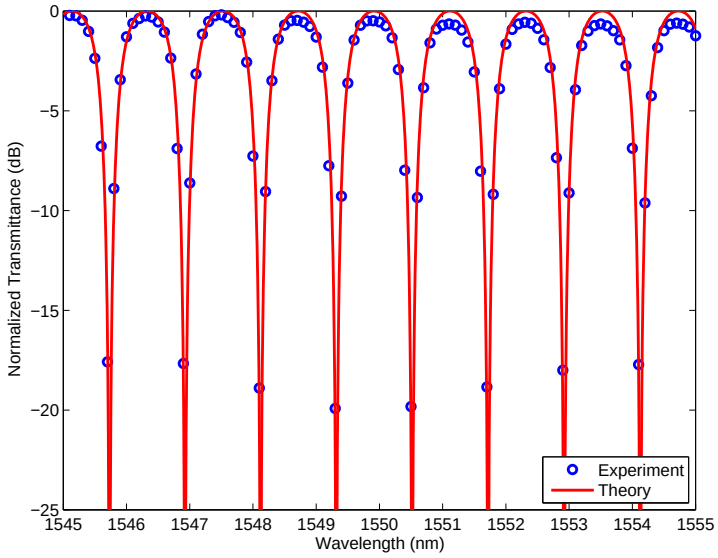

(b)

Figure 4.5: Transmission spectra for TE polarized light of (a) the air-clad polystyrene microring resonator and (b) the OG-125-clad SU-8 microring resonator

4.5.1 Fabrication

In this experiment, the soft PDMS was again cast from an electron-beam written pattern in SU-8. The polymer solution from which we mold the devices consisted of 5.5wt:vol% of CLD-1/amorphous polycarbonate (APC) in trichloroethylene (TCE)/dibromomethane (DBM). The CLD-1:APC ratio was 1:4 by weight, and the solvent consisted of TCE and DBM in a 50% ratio by volume. The resonators were molded directly on a silica on silicon substrate by applying a force of 25 N. The thickness of the thermally grown silica was 5 μm. The fabricated ring resonator had a radius of about 207 μm, and the thickness and width of the waveguides were about 1.6 μm and 1.4 μm respectively. The residue layer thickness from the molding was circa 130 nm. The waveguide-resonator gap was 430 nm.

4.5.2 Photobleach Trimming

To trim the resonator, we focussed broadband visible light onto a section in the lower half of the ring resonator in ambient conditions using the setup as illustrated in Fig. 4.7. The illumination intensity could be varied and the exposure area can be changed by using different objective lenses. The transfer characteristics of the resonator were recorded after exposures at fixed time intervals using a tunable laser. The input laser power is set to 0.1 μW to prevent additional photobleaching from the laser source during the measurement. The photobleached ring resonator is shown in Fig. 4.6. The photobleached region was transparent while the original polymer film was green in color.

Fig. 4.8 shows the total shift of the resonance wavelength as a function of the exposure time for an exposure intensity of 26 mW/cm^2 over a 0.12 mm^2 area. The experimental data was curve-fitted with an exponential model with excellent agreement. At the initial stages of the photobleaching, the fractional index change ($\Delta n/n$) and resonance wavelength shift varied approximately linearly with exposure time at a rate of -2.3×10^{-6} /s and -3.6×10^{-3} nm/s respectively. We observed a shift of

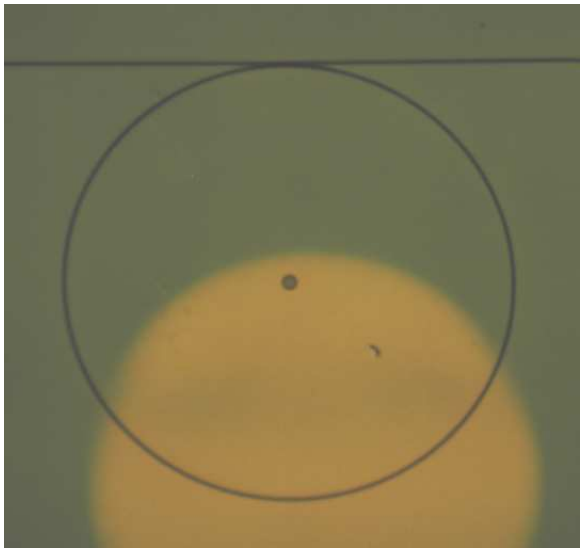

Figure 4.6: Optical micrograph of the photobleached resonator filter. The photobleached spot is the lighter region in the figure. The un-photobleached region is green in color.

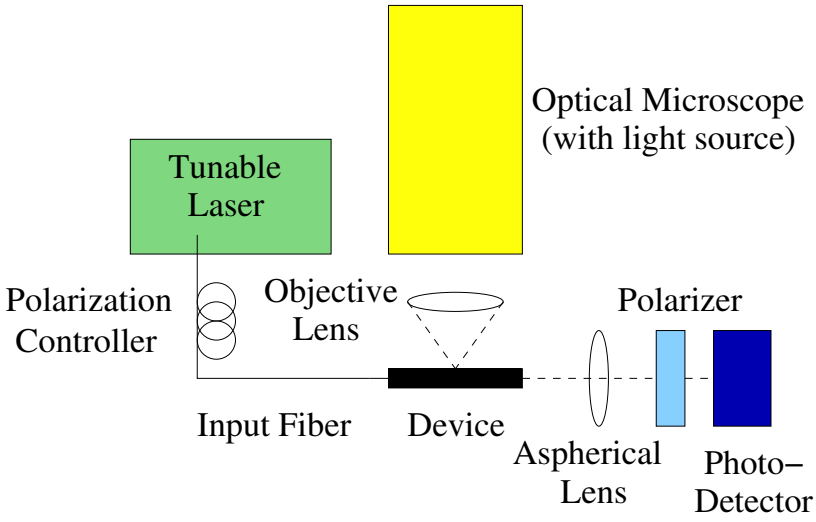

Figure 4.7: The experimental setup. The light from the microscope was focussed onto a spot on the sample for a fixed period of time, after which the transmission spectrum was measured using a tunable laser.

-8.73 nm after about 1.75 hours of exposure, though the exponential fit suggests a maximum wavelength shift of -9.8 nm, or fractional index change of -6.3×10^{-3}, should be possible. Fig. 4.9(a) shows the temporal evolution of the spectrum as a function of the exposure time. At long exposure times, the filter 3 dB bandwidth can be broader from that at $t = 0$ by about 20%. The decrease in the loaded Q factor, Q_L, could have been caused by a slight decrease in the index at the coupling region over time and also a slight change in the loss of the resonator induced by the photobleaching of the chromophores.

Fig. 4.9(b) shows the transfer characteristics after different exposure times for an illumination intensity of about 34 mW/cm^2 over an area of 0.28 mm^2. The resonance peaks are shifted by about 0.2 nm from each other. The width of the notch was essentially maintained as the resonance is shifted. For the device, the loss and refractive index vary with the photobleaching such that the extinction ratio increased from -15 dB to about -35 dB indicating the critical coupling condition is more closely satisfied. The device has a 3 dB bandwidth of 0.12 nm, an FSR of 1.11 nm, and hence a loaded quality factor, Q_L, of about 1.3×10^4 and a finesse of 10. Hence, $Q_{int} = 2Q_L$ for the ring resonator was about 2.6×10^4 at 1550 nm, which is among the highest reported for CLD-1 doped microrings [12].

The change in the refractive index due to photobleaching was most likely caused by photochemical degradation of the chromophores [105, 107, 108]. Previous studies on CLD-1/APC showed the composite has an absorption peak centered at around 670 nm [86, 104]. In ambient conditions, the photoexcited chromophores can react with oxygen and subsequently become damaged [86, 104, 107]. As confirmed by our experiment, the photodecomposition of the chromophores led to the decrease in the refractive index of CLD-1/APC. However, it is well established that the photochemical stability of CLD-1/APC can be significantly improved in an environment void of oxygen and purged with an inert gas such as argon [86, 104]. Therefore, for practical applications, after the device is trimmed, it should be hermetically packaged to ensure long-term stability.

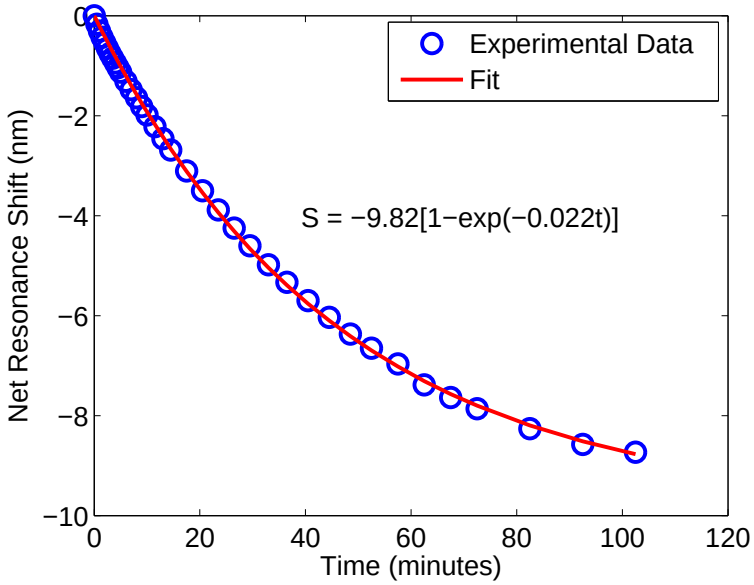

Figure 4.8: Net resonance wavelength shift as a function of exposure time. The exposure intensity was about 25 mW/cm^2 over a 0.12 mm^2 area. The experimental data is fitted with an exponential function as indicated. S is the shift in wavelengths in nm, t is the exposure time in minutes.

4.6 Summary

In this chapter, we have shown how soft lithography replica molding can be used to fabricate critically coupled microring resonators with $Q_{int} \sim 2 \times 10^4$ using a variety of polymer materials. We expect that the insertion losses of the devices can be further reduced by improving the input/output coupling, reducing the side-wall scattering, and reducing the material losses of the optical polymers. We have also demonstrated that a very wide resonance wavelength tuning range can be achieved by photobleaching CLD-1 chromophores in APC microring resonators. The trimming rate and range can be controlled by the concentration of the chromophores, the size of the exposure area, and the optical intensity. The chromophores that have not been photobleached can still be poled to render the polymer electro-optic [107, 109]. The soft-lithography fabrication method and the post-fabrication trimming are applicable to other types of polymer optical devices.

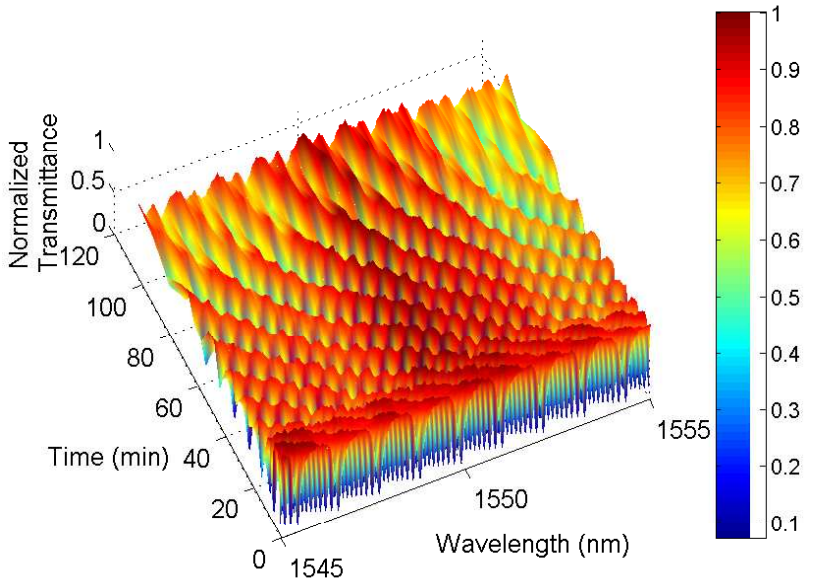

(a)

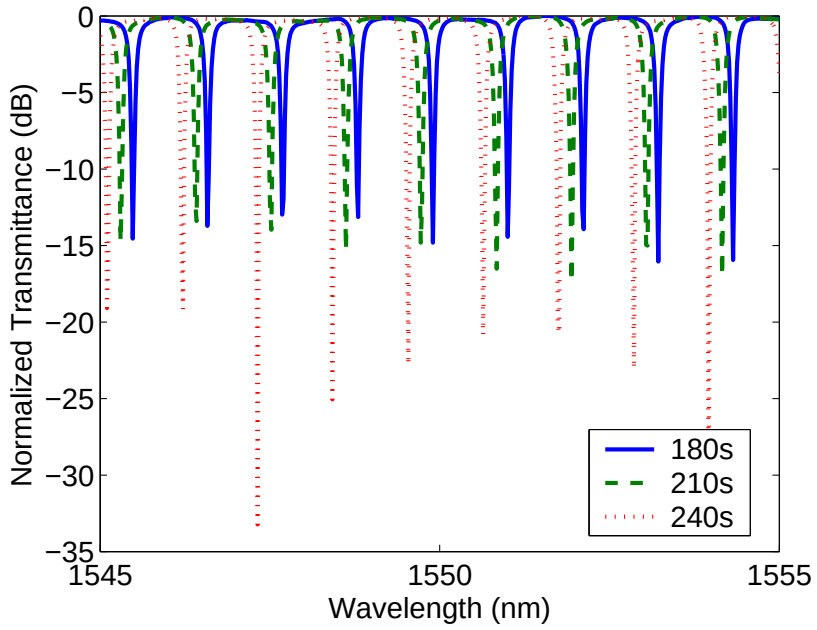

(b)

Figure 4.9: Tuning of the microring resonances. (a) The temporal evolution of the transmission spectrum for TE polarized light. The intensity of the exposure light source was about 35 mW/cm^2 and the exposure area was 0.28 mm^2. (b) The transmission spectra after certain exposure times under the same conditions as (a). The resonances shifted by about -0.2 nm after each 30 s.

Chapter 5

Microring Coupled-Resonator Optical Waveguides

5.1 Introduction

In this chapter[1,2], we present measurements of the transmission and dispersion properties of CROWs consisting of weakly coupled polymer microring resonators. The fabrication and the measurement methods of the CROWs are discussed as well. The experimental results agree well with the theoretical loss, waveguide dispersion, group delay, group velocity, and group velocity dispersion. The intrinsic quality factors of the microrings were about 1.5×10^4 to 1.8×10^4, and we measured group delays greater than 100 ps with a group velocity dispersion between -70 and 100 ps/(nm $\cdot$ resonator). With clear and simple spectral responses and without a need for the tuning of the resonators, the polymer microring CROWs demonstrate the practicability of using a large number of microresonators to control the propagation of optical waves.

For CROWs to be highly dispersive or to slow down light, a large number of weakly coupled, identical resonators are required. However, the major challenge in realizing CROWs and using multiple resonators for dispersion engineering [28, 111] has been the fabrication of low-loss resonators with strict size tolerances. The problem is compounded when the resonators are weakly coupled because of the narrow linewidth of

[1] ©2006 OSA. Reprinted, with permission, from [48].
[2] ©2006 IEEE. Reprinted, with permission, from [110].

the coupled resonators. One solution is to tune the resonators individually, but controlling the tuning becomes more complicated as the number of resonators increases. There have been several examples of high-order (> 10) coupled microresonators using microrings and photonic crystal defect cavities [10, 49, 76, 77]. However, the dispersion and delay were often not directly measured [10, 24, 77], and in the case of photonic crystal cavities, the resonators had low quality factors and the transmission spectra may be quite complex [24, 76].

5.2 Theory

In Chapters 2 and 3, we developed a transfer matrix method to analyze ring resonator CROWs and derived a set of analytical expressions for the delay and loss of CROWs. We shall briefly review those theoretical results, which will be useful in our comparisons with our experiments.

As described in Chapter 2, the dispersion relation of a microring CROW is

$$\sin(\beta\pi R) = \pm|\kappa|\cos(K\Lambda), \tag{5.1}$$

where $\beta = n_{eff}(\omega)\omega/c$ is the propagation constant in the ring, R is the radius, $\kappa = i|\kappa|$ is the dimensionless field coupling coefficient between two rings, K is the Bloch wavevector and Λ is the periodicity of the structure. In the limit of weak coupling, $|\kappa| \ll 1$, the dispersion relation reduces to

$$\omega(K) = \Omega\left[1 \pm \frac{|\kappa|}{m\pi}\cos(K\Lambda)\right], \tag{5.2}$$

where Ω is the resonance frequency of an uncoupled resonator in radians/s and $m = \Omega n_{eff}(\Omega)R/c$ is the azimuthal modal number.

Using Eq. (5.2), the group velocity, v_g of a CROW, given by $1/v_g = \partial K/\partial\omega$, is

$$\frac{1}{v_g} = \frac{n_{eff}}{\Lambda\sin(K\Lambda)}\left[\pm\frac{R\pi}{c|\kappa|} - \frac{\cos(K\Lambda)}{n_{eff}^2}\frac{\partial n_{eff}}{\partial\omega}\right]. \tag{5.3}$$

At the center of the CROW transmission band, where $\omega = \Omega$ and $K\Lambda = \pi/2$, the magnitude of the group velocity is maximum and is equal to

$$|v_g(\Omega)| = \frac{c|\kappa|\Lambda}{\pi R n_{eff}(\Omega)}. \tag{5.4}$$

The time delay of a pulse propagating through the CROW, τ, is determined by the distance traversed in the CROW and the group velocity,

$$\tau = \frac{N\Lambda}{v_g}, \tag{5.5}$$

where N is the number of resonators. At the center of the CROW band, the delay is equal to

$$\tau_d = \frac{N\pi R n_{eff}(\Omega)}{c|\kappa|}. \tag{5.6}$$

The loss of a CROW is given by the product of the time delay, the phase velocity of the light in the resonators, and the loss per unit length in the resonators. At the center of the band, the loss, α_Ω, is

$$\alpha_\Omega = \frac{\alpha_l N\pi R}{|\kappa|}, \tag{5.7}$$

where α_l is the loss per length in the rings.

We shall define the slowing factor, S, to be the ratio of the group velocity in free space to the group velocity in the CROW, $S = c/v_g$, such that at the band center,

$$S_\Omega = \frac{\pi n_{eff}(\Omega)}{2|\kappa|}. \tag{5.8}$$

Therefore, to obtain a large slowing factor, weak inter-resonator coupling is necessary.

Using the conventional definition of the group velocity dispersion (GVD), the GVD is given by the change of the delay time with respect to the wavelength [112].

Neglecting the dependence of n_{eff} on ω, the GVD per resonator, D, is

$$D \equiv \frac{1}{N}\frac{\partial \tau}{\partial \lambda} = \frac{\Lambda^3 (2\pi c)^2}{v_g^3 \lambda^2}\left(\frac{1}{\lambda_0} - \frac{1}{\lambda}\right), \tag{5.9}$$

where $\lambda_0 = 2\pi\Omega/c$ is the resonance wavelength. As evidenced by Eq. (5.9), the GVD is maximum at the band edges where $v_g \to 0$ and minimum at the band center where $\lambda = \lambda_0$. The GVD switches sign across the band center, such that for $v_g > 0$, it is negative for $\lambda < \lambda_0$ and positive for $\lambda > \lambda_0$.

From our spectral and delay measurements of CROWs, we shall verify Eqs. (5.4)-(5.9) and determine the transmission and dispersive properties of the ring resonators.

5.3 Fabrication

We fabricated CROWs with as many as 12 weakly coupled microring resonators in polymethyl-methacrylate (PMMA, $n = 1.49$) by direct electron-beam writing. As CROWs require numerous nearly identical resonators, PMMA is ideal for their fabrication since it is a high resolution electron-beam resist. A low index perfluoropolymer, Cytop$^{\text{TM}}$ ($n = 1.34$, Asahi Glass), was used as the lower cladding. The material system of PMMA and Cytop$^{\text{TM}}$ is used in commercial polymer optical fibers [113] and has previously been used for simple waveguides [114]. The PMMA microrings did not have an upper cladding in order to keep the radius as small as possible.

Fig. 5.1 summarizes the Cytop$^{\text{TM}}$ and PMMA preparation process for the electron-beam writing. We began the fabrication process by depositing a 5.2 μm thick layer of Cytop$^{\text{TM}}$ CTL-809M on a 250 μm thick silicon substrate. To ensure flatness and uniformity over the wafer, the deposition of the Cytop$^{\text{TM}}$ was accomplished via a series of spinning and thermal curing steps. First, we spun the Cytop$^{\text{TM}}$ on the silicon at 1500 RPM. Adhesion promoters were not necessary. Next, the Cytop$^{\text{TM}}$ was baked at 65°C for 60 s, 95°C for 60 s, and 180°C for 20 mins. The ramping of the bake temperature was critical in attaining flat and uniform surfaces. The spinning and baking steps were then repeated two more times, with a final bake at 180°C for 3

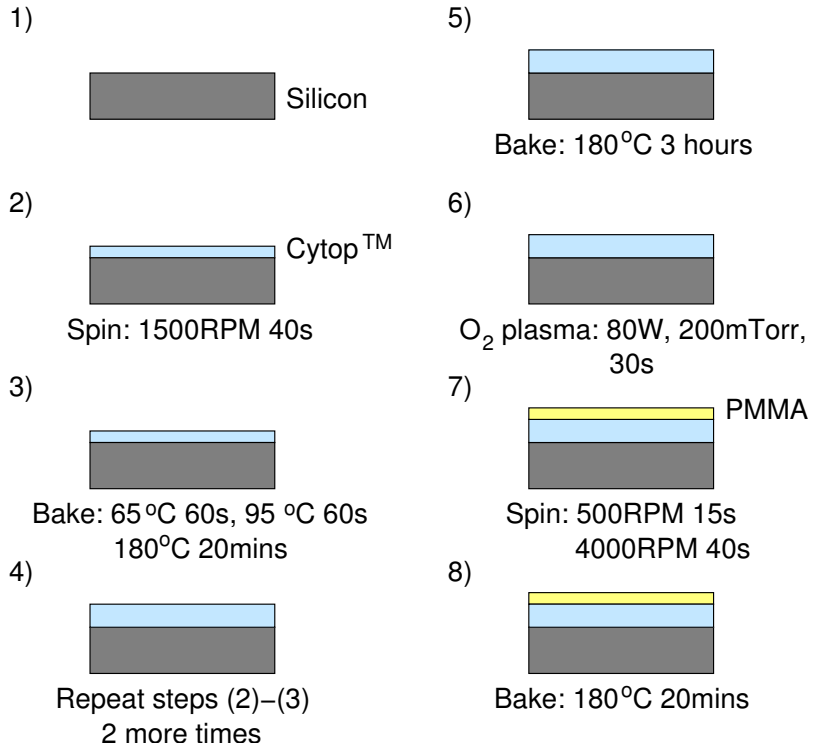

Figure 5.1: Summary of the Cytop^{TM} and PMMA preparation process for the electron-beam writing

hours.

After the chip cooled down, an oxygen plasma treatment (Anatech SP100) of the Cytop^{TM} was necessary for the adhesion of Cytop^{TM} to PMMA. The plasma exposure was 30 s long at an RF power of 80 W and O_2 pressure of 200 mTorr. After an optional 60 s exposure to hexamethyldisilazane (HMDS), a 2.6 μm of PMMA 950K C10 (Microchem) was spun onto the chip at 500 RPM for 15 s and then 4000 RPM for 40 s. A pre-exposure bake at 180°C for 20 min ensured solvents were evaporated and improved the adhesion between the Cytop^{TM} and PMMA.

We next patterned the microrings via direct electron-beam writing (Leica EBPG 5000). Since PMMA is a positive resist, we defined the cladding regions with the electron-beam lithography. We used an acceleration voltage of 100 kV and an electron-beam current of 3.5 nA at a dosage varying from 785 to 815 μC/cm^2. After the electron-beam exposure, we developed the sample in a 1:3 methyl isobutyl ketone (MIBK):isopropanol (IPA) solution. Finally, we separated the devices by cleaving.

Fig. 5.2 shows several optical and scanning electron microscope pictures of the fabricated devices. The electron-beam lithography produced waveguides with fairly smooth sidewalls. Fig. 5.2(d) shows the device end facet which was defined by scribing and breaking. The slight waviness of the Cytop^{TM} near the PMMA waveguide is an artifact of charging during the scanning electron microscope imaging. The quality of the end facet indicates good adhesion between the PMMA and Cytop^{TM} and between the Cytop^{TM} and silicon. It also shows that both PMMA and Cytop^{TM} possess the mechanical properties suitable to cleaving. The waveguides had a width of 2.9 μm and a height of 2.6 μm. The cladding regions were 4 μm wide. The radius of the rings was 60 μm such that the bend loss, as calculated using a radial beam propagation method, would be < 1 dB/cm. There was no coupling gap between the resonators and between the waveguide and first/last resonator. However, due to the radius of curvature of the rings as well as the waveguide design and index contrast, even without a coupling gap, weak coupling between the resonators was achieved.

5.4 Transmission and Group Delay Measurements

We measured both the transmission spectra and group delays of the fabricated microring CROWs. The spectral measurements were straightforward wherein we detected the transmitted output power as a function of the wavelength scanned by a tunable laser (HP 81640A). The group delay measurement was performed using a RF phase-shift technique [11, 115].

Fig. 5.3 is a schematic of the setup of the group delay measurement. An RF lock-in amplifier (SR844) generated the drive voltage to a modulator (Uniphase MA150-001975) and detected the phase-shift between the drive and measured signals. Light from the tunable laser source was coupled into the device under test (DUT) via a standard single-mode fiber. The transmitted light was collected with a multi-mode fiber coupled to a high-speed (2.5 GHz) InGaAs avalanche photodiode (APD, Fujitsu FRM5W231DRF). To determine the absolute time delay through the CROW, we measured the reference phase-shift due to the propagation through the input and

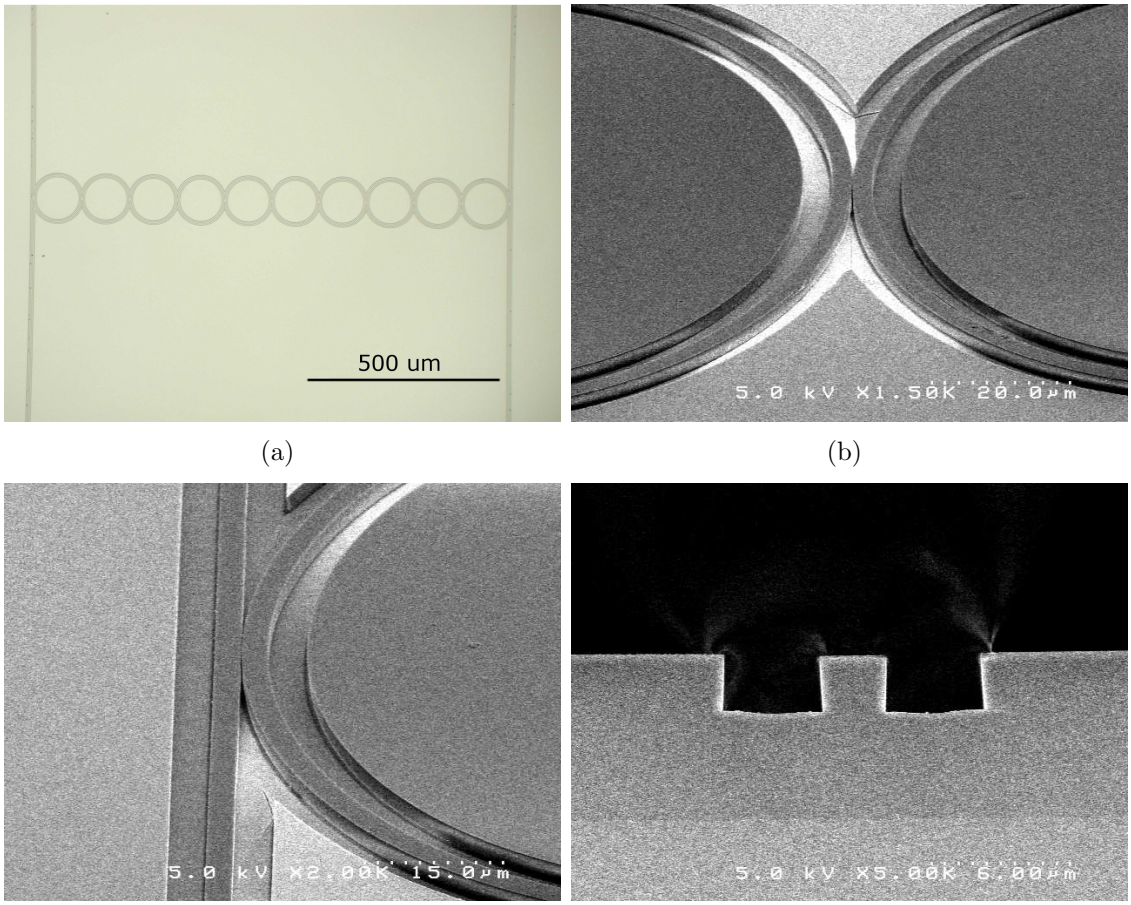

(a) (b)

(c) (d)

Figure 5.2: Optical microscope [(a)] and scanning electron microscope [(b)–(d)] images of the fabricated devices in PMMA on Cytop^{TM} on silicon. (a): 10 coupled microring resonators. The ring radius is 60 μm. (b): The coupling region between two rings. (c): The coupling region between the input/output waveguide and the microring. (d): A waveguide end facet produced by cleaving.

output waveguides only and calibrated for any intrinsic, intensity-dependent system response. Thus, the measured group delay through the CROW is given by

$$\tau_m = \frac{\theta_m - \theta_{ref}}{360^\circ} \frac{1}{f_{mod}}, \tag{5.10}$$

where θ_m is the measured phase-shift angle in degrees, θ_{ref} is the reference angle in degrees, and f_{mod} is the modulation frequency in Hz. By changing the wavelength of the tunable laser source, we measured the group delay as a function of the optical frequency.

The accuracy of the group delay depends on the accuracy of the measured phase-shift. For a fixed error in the measured angle, the error in the group delay is smaller for a higher modulation frequency by Eq. (5.10). However, a high modulation frequency may cause significant distortions in the delay and amplitude measurements with the lock-in amplifier, because the two side-bands generated about the optical carrier may experience vastly different transmission characteristics in a narrow-band device. This distortion is less pronounced if f_{mod} is kept significantly smaller than the bandwidth of the device [11]. The measured angle can also have an ambiguity equal to multiples of 360°, equivalent to a delay of $1/f_{mod}$. Hence, a higher modulation frequency would more easily lead to uncertainty in the group delay due to possible 360° phase-shifts.

For our experiments, we used a modulation frequency of 200 MHz, which was about 100 times narrower than the full-width half-maximum (FWHM) linewidth of the CROWs. A maximum delay of 5 ns can be measured at this modulation frequency without encountering the 360° ambiguity. However, the phase error in our measurement was about ±0.5°, equivalent to a ±7 ps uncertainty in the time delay. The trade-off between the modulation frequency and the accuracy of the group delay is intrinsic to this measurement technique.

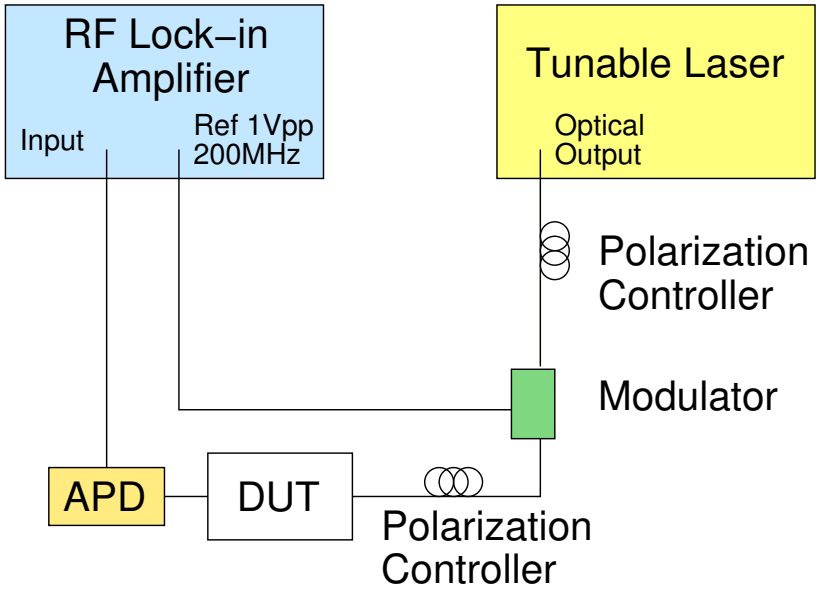

Figure 5.3: Schematic of the group delay measurement setup. The RF lock-in amplifier generates a 1 V peak-to-peak voltage at 200 MHz to drive the modulator. DUT is the device under test, and APD is the avalanche photodiode.

5.5 Magnitude Response

5.5.1 Transmission Spectra

Fig. 5.4 shows the transmission spectrum at the drop port of a 10 microring long CROW for TE polarized light. There are no spurious peaks in the spectrum, indicating that the resonators were nearly identical. However, slight variations in the resonators and polarization mixing may have caused the broad envelope in the spectrum.

We compared our measured results with the theoretical results computed from the transfer matrices [34]. For the theoretical calculations, we assumed the resonators to be identical and neglected the dependence of n_{eff} on the wavelength. The lineshapes of both the drop and through ports are sensitive to the propagation loss in the rings, but while the drop port is sensitive to the inter-resonator coupling, the through port is more sensitive to the coupling between the input/output waveguides and the rings. Therefore, by fitting the drop and through spectra as well as the group delay, we could estimate the complete set of parameters that describe an ideal CROW composed

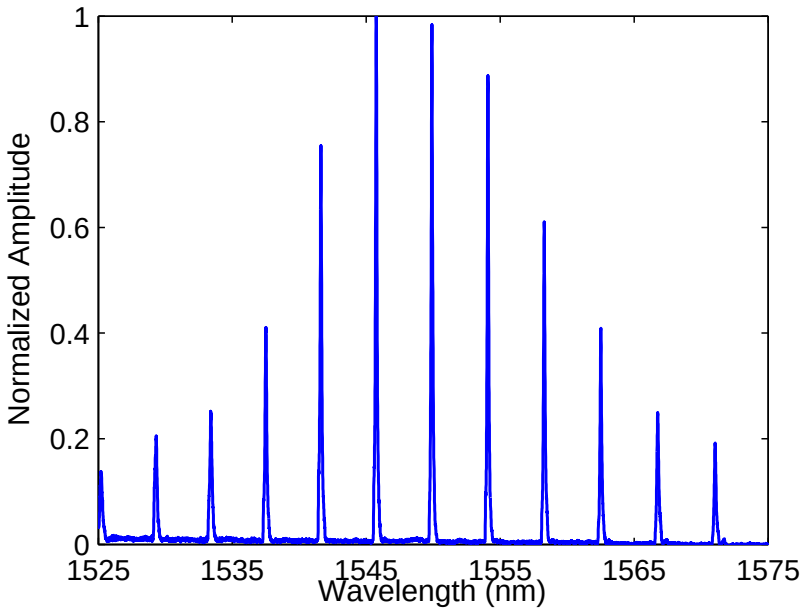

Figure 5.4: The drop port transmission spectrum of TE polarized light through a CROW of 10 coupled microring resonators

of identical resonators: the propagation loss in the resonators, the inter-resonator coupling coefficient, and the waveguide-resonator coupling coefficient.

Fig. 5.5 shows the experimentally measured spectra at the drop and through ports at the resonance near 1550 nm in Fig. 5.4. The inset shows the drop port spectrum in dB scale. The measured extinction ratio of circa -20 dB was limited by the noise floor of our detector. For the fit, the inter-resonator field coupling coefficient is $|\kappa| = 0.12$, the waveguide-resonator field coupling coefficient is $|\kappa_i| = 0.15$, and the propagation loss is 17 dB/cm. The through port spectrum shows the Fabry-Perot resonances defined by the device end facets. The multiple notches in the spectrum indicate there were indeed variations in the resonators, which were not as apparent in the lineshape of the drop port. However, these variations were small enough such that we were able to obtain simple, clear spectral responses as in Fig. 5.4. The ring resonators were under-coupled to the input waveguide so the extinction of the notch in Fig. 5.5 is only about -1.5 dB.

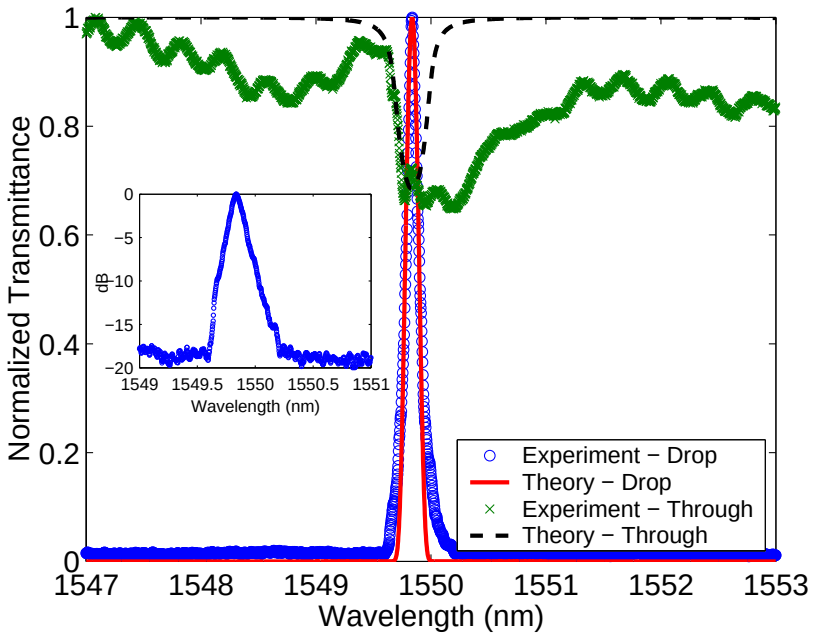

Figure 5.5: Experimental and theoretical spectra at the drop and through ports for the transmission peak near $\lambda = 1550$ nm in Fig. 5.4. The fit parameters are $|\kappa| = 0.12$, $|\kappa_i| = 0.15$, and $\alpha_l = 17$ dB/cm. Inset: The measured drop port spectrum in dB scale

5.5.2 Losses

In general, the CROWs we fabricated had inter-resonator coupling coefficients, $|\kappa|$, of about 0.1 to 0.15. The propagation losses of the ring resonators were about 15 to 18 dB/cm, resulting in intrinsic quality factors of 1.5×10^4 to 1.8×10^4. Most of the propagation loss was likely due to side-wall scattering since the index contrast between the core and the air cladding was quite large. The material losses of PMMA are about 1.5 to 2 dB/cm [116, 117] and the theoretical bend loss was less than 1 dB/cm. Due to the losses in the CROWs, ripples in the passband were not observed. Passband ripples can introduce distortions to and limit the bandwidth of propagating optical pulses [11, 22]. The ripples may be reduced by choosing a suitable waveguide-resonator coupling coefficient [35], or the passband can be optimally flattened through the apodization of the inter-resonator coupling coefficients [5, 11, 22].

The fiber-to-fiber insertion loss at the through port was about -15 to -20 dB off-resonance, and on-resonance, the loss was about -16 to -21 dB. The fiber-to-fiber

insertion loss at the drop port depends on the number of resonators in the CROW and varied from about −35 dB for 4 resonators to −45 dB for 12 resonators. The ratio of the drop power to the difference between the on and off resonance through power gives equivalent losses of 2.4 to 3.5 dB per resonator, in excellent agreement with the loss of 2.3 to 3 dB per resonator calculated with Eq. (5.7).

The measured spectrum and loss per resonator suggest that while slight variations in the resonators existed, the microrings comprising the CROWs were nearly identical. Our results show that the maximum number of microrings that can be coupled together is not limited by the fabrication accuracy but rather by the resonator losses.

5.6 Dispersive Properties

To comprehensively characterize the CROWs, we obtained the dispersive properties of the ring resonators and the CROW as well. In this section, we shall extrapolate the group and effective indices of resonator waveguides, the group delay and slowing factors in the CROWs, and the CROW GVD from our spectral and delay measurements.

5.6.1 Group Index

The group index of the resonator waveguides, n_g, is related to the free spectral range of the resonator,

$$\Delta f_{FSR} = \frac{c}{2\pi n_g R}, \tag{5.11}$$

where Δf_{FSR} is the free spectral range in frequency and the group index is defined as

$$n_g(\lambda_1) = n_{eff}(\lambda_1) - \lambda_1 \frac{\partial n_{eff}}{\partial \lambda}_{|\lambda_1}. \tag{5.12}$$

Therefore, from the transmission spectrum, we may obtain the group index as a function of the wavelength. Fig. 5.6 shows the group index extrapolated from the transmission spectrum in Fig. 5.4. We have also plotted the theoretical group in-

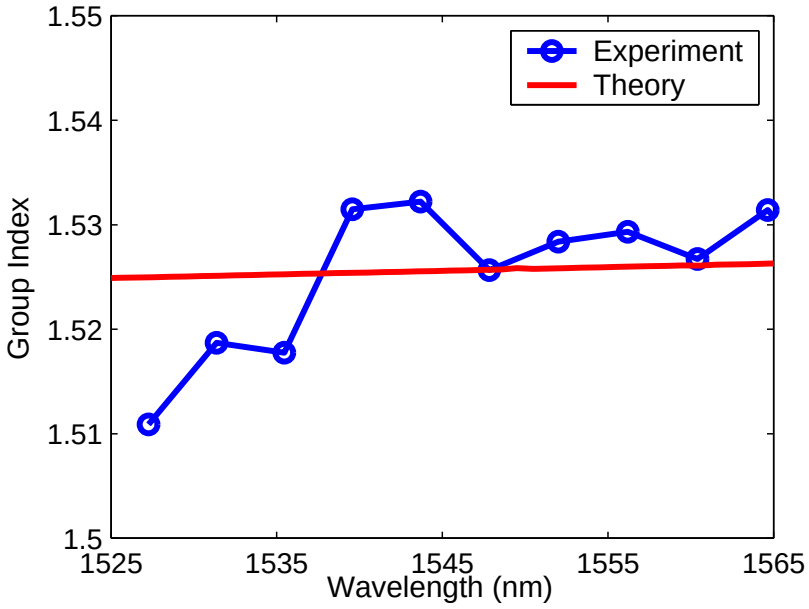

Figure 5.6: The experimentally measured and theoretically calculated group index for the PMMA on Cytop^{TM} ring resonators. The experimental values are extrapolated from the spectrum in Fig. 5.4.

dex of the ring resonators calculated using a mode-solver. There is generally good agreement between the theoretical and experimental values. The calculated group index is approximately 1.525 and the measured group index ranges from 1.51 to 1.53. The variation in the measured group index may be due to slight inaccuracies in the wavelength and material dispersion, which was not accounted for in the mode-solver calculations.

5.6.2 Effective Index and Group Delay

The effective index, n_{eff}, from the mode-solver calculations is approximately 1.42 in this wavelength range. We may also obtain the effective index by using Eq. (5.6), since the group velocity at the center of the CROW band depends on the effective index and not the group index. Table 5.1 lists the inter-resonator coupling coefficients, measured group delays and slowing factors for TE polarized light in CROWs of various lengths that were fabricated. By plotting $\tau_d|\kappa|$ versus N, according to Eq. (5.6), the slope is proportional to the effective index averaged over the wavelength

Table 5.1: Coupling Coefficients, Group Delays, and Slowing Factors for CROWs of Various Lengths

Number of Microrings (N)	**Coupling** $\lvert\kappa\rvert$	**Group Delay** $\tau_{\mathbf{d}}$(ps)	**Slowing Factor** ($\mathbf{S_\Omega}$)
4	0.15	25.9	16.2
6	0.25	23	9.6
8	0.15	49	15.2
10	0.12	80	19.9
12	0.10	110	22.9

range considered. Thus, we can compare the experimental effective index with the theoretical value and verify Eq. (5.6).

Fig. 5.7 shows the $\tau_d|\kappa|$ as a function of N. The data fits very well with a linear function, with a slope of 0.9182 ps, translating to an effective index of 1.46. The value agrees with the calculated value of 1.42 within the experimental error, indicating that Eq. (5.6) accurately expresses the time delay at the band center of a CROW.

As listed in Table 5.1, the resonators in the CROWs were generally weakly coupled, with an inter-resonator intensity coupling of about 1 to 2%. The weak inter-resonator coupling led to slowing factors at the maximum of the transmission peaks of about 15 to 25. The FWHM of the transmission peaks was approximately 15 to 20 GHz. The coupling coefficient was highly sensitive to the electron-beam writing conditions and the PMMA/Cytop$^{\mathrm{TM}}$ layers such that the coupling coefficient was not replicated exactly from device to device. Nonetheless, as evidenced by Fig. 5.7, the group delays of the devices were consistent with each other.

5.6.3 Group Velocity Dispersion

Finally, we can determine the group velocity dispersion of the CROW from the group delay measurements. Theoretically, the GVD is given by Eq. (5.9). The GVD switches sign across the resonance frequency Ω and is highest at the band edges where the group velocity is small. We extracted the GVD by taking the derivative of the

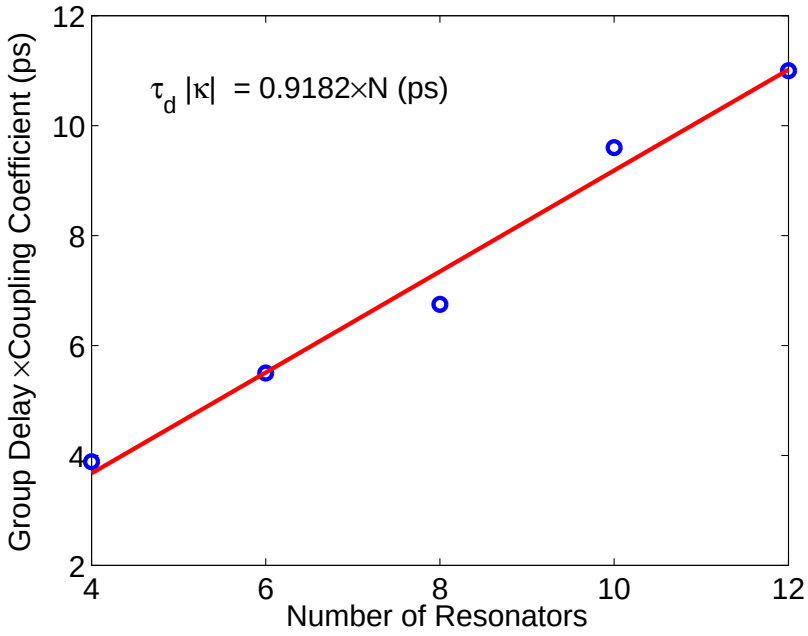

Figure 5.7: The product of the time delay at band center and the inter-resonator coupling, $\tau_d|\kappa|$, is plotted against the number of resonators using the results summarized in Table 5.1. The slope of the graph gives $\pi R n_{eff}/c$ according to Eq. (5.6).

measured group delay with respect to the wavelength.

Fig. 5.8 summarizes the transmission, group delay, phase response, and GVD for the TE polarization of a CROW consisting of 12 microrings, for which the delay properties are listed in Table 5.1. The phase response was obtained by integrating the delay with respect to the frequency. The curvatures of the theoretically calculated group delay and GVD change at the band edges due to the losses in the resonators [118]. The measured GVD follows the general trend described by Eq. (5.9). In Fig. 5.8, the GVD changes from negative to positive across the resonance peak. The high group delay and GVD at the edges of the peak may not be physical, since the transmission amplitude was low at these wavelengths. The change in the GVD and group delay curvatures at the band edges in the calculated results could not be measured, most likely because of the low transmission amplitude.

Unsurprisingly, the GVD of the CROW can be very high. The measured GVD varied from -100 to 70 ps/(nm $\cdot$ resonator) across the FWHM of the peak, with zero GVD at 1511.18 nm, near the resonance peak at 1511.15 nm. The measured GVD is

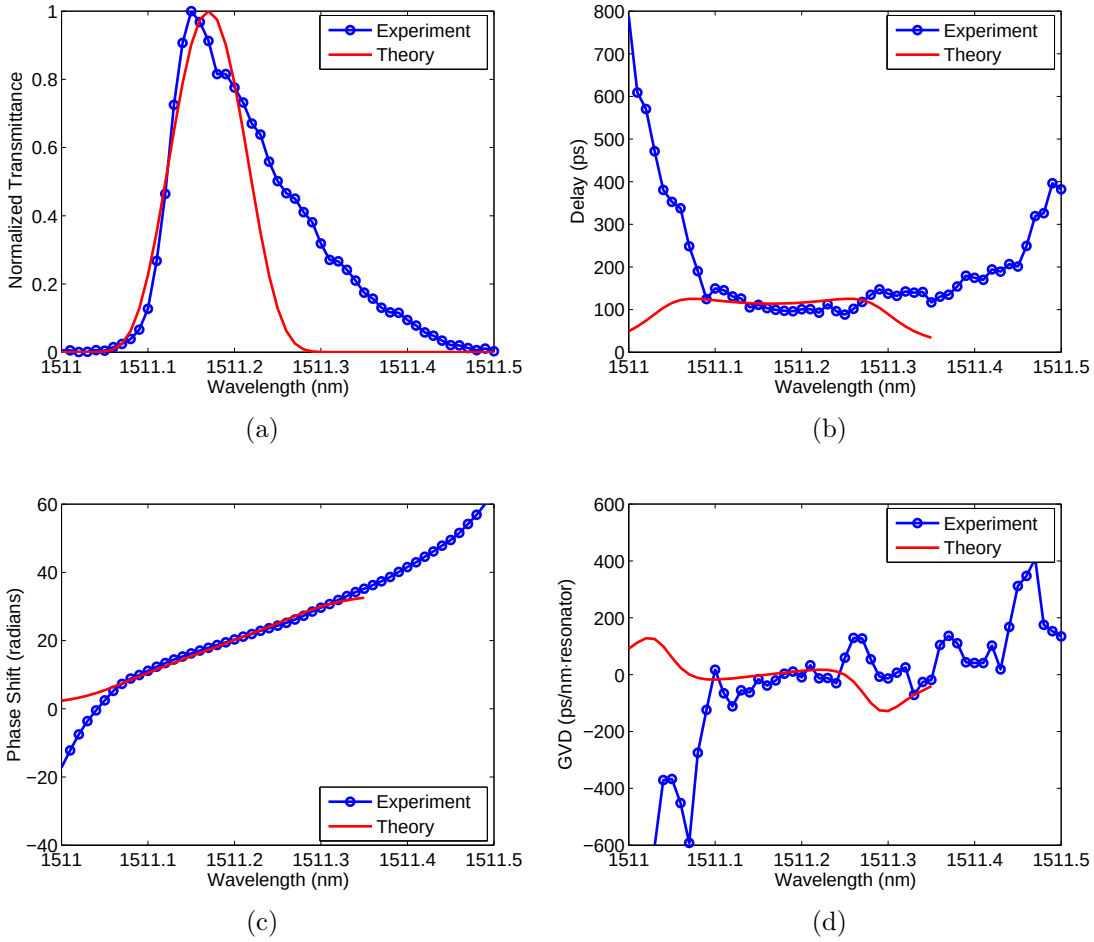

Figure 5.8: (a) The transmission amplitude, (b) the group delay, (c) the phase response, and (d) the group velocity dispersion of TE polarized light in a 12 microring long CROW with delay properties listed in Table 5.1.

significantly higher than the theoretically calculated GVD which ranges from -17 to 17 ps/(nm $\cdot$ resonator) across the FWHM of the transmission peak. The dispersion of the resonator waveguide alone does not account for the difference. The per resonator GVD due to waveguide dispersion is

$$D_{wg} = \frac{\pi R}{c|\kappa|}\frac{\partial n_g}{\partial \lambda}, \tag{5.13}$$

which is approximately 2.2×10^{-4} ps/(nm $\cdot$ resonator). The discrepancy may be a result of the deviation from the ideal scenario of identical resonators. The asymmetry of the transmission peak suggests the resonators were not perfectly identical and perhaps the polarization was not purely TE. Since the GVD, given by Eq. (5.9), scales as $1/v_g^3$, any slight deviation of the group velocity will result in a large change in the dispersion.

Compared to other engineered waveguide structures reported to date, such as photonic crystal waveguides and fibers, because of the weak inter-resonator coupling, the CROWs we have demonstrated possess a significantly higher GVD, even though the refractive indices of the polymer materials are relatively low. The measured GVD values of about ± 100 ps/(nm $\cdot$ resonator) is equivalent to $\pm 8.3 \times 10^8$ ps/(nm $\cdot$ km), and the calculated GVD of ± 17 ps/(nm $\cdot$ resonator) is equivalent to $\pm 1.4 \times 10^8$ ps/(nm $\cdot$ km). The CROWs we have presented are about 10^7 times more dispersive than conventional optical fibers, 10^6 times more dispersive than highly dispersive photonic crystal fibers [119], and approximately 100 to 1000 times more dispersive than photonic crystal waveguides reported to date [120, 121]. Compared to previously reported GVD values of photonic crystal CROWs [122], the GVD of our microring CROWs is about an order of magnitude greater. With such large values of both normal and anomalous dispersion, CROWs may find applications in dispersion management and nonlinear optics [112, 123, 124, 125, 27, 26].

5.7 Summary

We have fabricated microring CROWs in polymer materials and have measured their spectral and dispersive properties. Direct electron-beam writing of the PMMA on Cytop^{TM} produces nearly identical microrings such that no external tuning of the ring resonators is necessary, greatly simplifying the fabrication and characterization process. The simple and clear transmission spectra of the microring CROWs are in sharp contrast to other resonators such as disks, spheres, and photonic crystal defects. The maximum number of coupled rings and the maximum achievable delay are limited by the loss in the resonators and not by any fabrication inaccuracies. Group delays greater than 100 ps were measured in the CROWs, with slowing factors of circa 15 to 25. The group velocity dispersion of the CROWs can be very high, about ± 100 ps/(nm $\cdot$ resonator), with most of the dispersion arising from the CROW device structure rather than from the material or waveguide dispersion. Our demonstration illustrates the feasibility of using a large number of microresonators to engineer the transmission and dispersion of optical waves.

Chapter 6

Active CROWs: Gain Enhancement and Noise

6.1 Introduction

As fabrication technologies improve, very high-order, even on the order of a hundred, coupled resonators are now achievable [49]. One of the remaining important challenges, as illustrated by our results in the last chapter, is to overcome the optical loss in CROWs. In Chapter 3, we found the loss accumulated in these devices *can* scale with the number of resonators in the structures and the time delay (we shall show in this chapter that this is not always the case). Therefore, to compensate for the accumulated losses, an amplifying section that is placed after a CROW may have to be long, perhaps much longer than the CROW itself. Thus, to minimize the device footprint, it would be advantageous to continuously amplify a wave propagating in an active CROW.

In the remainder of this thesis, we shall investigate theoretically and experimentally active, amplifying CROWs. The present chapter examines theoretically the effect of resonant gain enhancement and noise[1]. Using a tight-binding analysis, we shall show that, contrary to expectation, the net gain of a wave in a CROW does not necessarily depend on its group velocity but is strongly affected by the excitation and termination of the CROW. These results can be applied to losses as well, though optical gain makes laser oscillation possible and must be considered with more

[1]

care. Using the same formalism, we shall find the expression for the noise caused by spontaneous emission.

6.2 Time Domain Tight-Binding Equations

To provide a generalized approach to analyze the amplifying and noise properties of CROWs, we shall use a time domain tight-binding or coupled-mode formalism. While time domain coupled-mode equations are commonly used to analyze coupled resonators, their derivations are often heuristic [5, 37]. In this section, we shall outline the derivation of these time domain coupled-mode or tight-binding equations from Maxwell's equations. The derivation will make explicit the assumptions that are made in obtaining the simple coupled oscillator equations found in the literature.

To analyze gain/loss as well as noise, we first define the polarization density of the structure as

$$\mathbf{P}(\mathbf{r},t) = \epsilon_0\chi(\mathbf{r})\mathbf{E} + \epsilon_0\mathbf{p}(\mathbf{r},t), \tag{6.1}$$

where $\chi(\mathbf{r})$ is the susceptibility and $\mathbf{p}(\mathbf{r},t)$ is the small amplitude fluctuation of $\mathbf{P}(\mathbf{r},t)$ which we will use later in our analysis of noise. Generally speaking, in active structures, the susceptibility is a function of time, since the carrier or population densities are modified by the optical field. We shall simplify the analysis to a quasi-static picture where the optical signal varies on a much longer time scale than the carrier dynamics, so the gain and loss can be taken as constants. Furthermore, in the regime of small values of gain, we can neglect nonlinearities due to saturation so $\chi(\mathbf{r})$ is linear and can be expressed as $\chi(\mathbf{r}) = \epsilon(\mathbf{r}) + i\sigma(\mathbf{r})$. $\epsilon(\mathbf{r})$ is the dielectric profile of the structure and $\sigma(\mathbf{r})$ accounts for the gain or loss depending on its sign (positive for gain and negative for loss). $\epsilon(\mathbf{r})$ and $\sigma(\mathbf{r})$ are dimensionless. Substituting the polarization density into Maxwell's equations, we arrive at

$$\nabla\times\nabla\times\mathbf{E}(\mathbf{r},t) + \frac{1}{c^2}\left[\epsilon(\mathbf{r}) + i\sigma(\mathbf{r})\right]\ddot{\mathbf{E}}(\mathbf{r},t) = -\frac{1}{c^2}\ddot{\mathbf{p}}(\mathbf{r},t). \tag{6.2}$$

In the tight-binding or coupled-mode approach, we assume the fields in a CROW,

$\mathbf{E}(\mathbf{r},t)$, can be expressed as a superposition of the localized resonator modes, $\mathbf{E}_\Omega(\mathbf{r})$. Strictly speaking, in the presence of loss or gain, the structure does not support true eigenmodes [127, 128]. However, we shall assume that the index contrast is sufficiently high and the loss/gain small so that these "quasi-modes" are well approximated by an expansion over the lossless resonator modes. Therefore, for a CROW consisting of N identical resonators, the field is

$$\mathbf{E}(\mathbf{r},t) = \exp(i\omega t)\sum_{n=1}^{N} a_n(t)\mathbf{E}_\Omega(\mathbf{r} - n\Lambda\hat{z}), \tag{6.3}$$

where ω is the frequency of oscillation of the electric field, $a_n(t)$ is a time-dependent amplitude coefficient, $\hat{z}$ is the direction of periodicity, and Λ is the period. Depending on the specific problem we solve, ω may be a particular eigenfrequency or the frequency of an externally driving field. $a(t)$ varies slowly compared to the optical frequency. We note that the localized resonator modes themselves satisfy the equation,

$$\nabla \times \nabla \times \mathbf{E}_\Omega(\mathbf{r}) = \frac{\Omega^2}{c^2}\epsilon_\Omega(\mathbf{r})\mathbf{E}_\Omega(\mathbf{r}), \tag{6.4}$$

where Ω is the resonance frequency and $\epsilon_\Omega(\mathbf{r})$ is the dielectric constant of the single resonator.

Substituting Eqs. (6.3) and (6.4) into Eq. (6.2) and applying the slowly-varying envelope approximation, $|\ddot{a}_n| \ll 2\omega|\dot{a}_n|$, we drop the $\ddot{a}_n$ terms. The slowly-varying envelope approximation is valid only in the case of weak inter-resonator coupling, meaning that

$$\int \mathrm{d}^3\mathbf{r}\mathbf{E}^*_\Omega(\mathbf{r} - \Lambda\hat{z})f(\mathbf{r})\mathbf{E}_\Omega(\mathbf{r}) \ll \int \mathrm{d}^3\mathbf{r}\mathbf{E}^*_\Omega(\mathbf{r})f(\mathbf{r})\mathbf{E}_\Omega(\mathbf{r}), \tag{6.5}$$

where $f(\mathbf{r}) = \epsilon(\mathbf{r})$ or $|\sigma(\mathbf{r})|$. Typically, $|\sigma(\mathbf{r})|$ is much smaller than $\epsilon(\mathbf{r})$. However, at certain material resonances, the imaginary part of the susceptibility can dominate so the resonators can be coupled through $\sigma(\mathbf{r})$ as well.

Subsequently, we integrate the result over $\int \mathrm{d}^3\mathbf{r}\mathbf{E}^*_\Omega(\mathbf{r} - m\Lambda\hat{z})$ and keep only up to nearest neighbor interaction terms (i.e., only the $n = m, m \pm 1$ terms). We further

approximate that the $\dot{a}_{m\pm1}$ terms are negligible compared the $\dot{a}_m$ term, which is again only valid in the weak coupling regime. To simplify the expressions, we may adopt the normalization condition $\int \mathrm{d}^3\mathbf{r}\mathbf{E}^*_\Omega(\mathbf{r})\cdot\epsilon_\Omega(\mathbf{r})\mathbf{E}_\Omega(\mathbf{r}) = 1$. At this point, we arrive at

$$\begin{aligned} 2i\omega\dot{a}_m(1+\Delta\alpha+i\sigma_m) &= a_m\left[(\omega^2-\Omega^2)+\omega^2(\Delta\alpha+i\sigma_m)\right] \\ &+ a_{m+1}\left[\omega^2(d+i\Delta\sigma)-\Omega^2 b\right] + a_{m-1}\left[\omega^2(d^*+i\Delta\sigma*)-\Omega^2 b^*\right] - \ddot{p}_m\exp(-i\omega t), \end{aligned} \tag{6.6}$$

where the various constants are given by

$$\Delta\alpha = \int \mathrm{d}^3\mathbf{r}\mathbf{E}^*_\Omega(\mathbf{r})\cdot[\epsilon(\mathbf{r})-\epsilon_\Omega(\mathbf{r})]\mathbf{E}_\Omega(\mathbf{r}) \tag{6.7a}$$

$$b = \int \mathrm{d}^3\mathbf{r}\mathbf{E}^*_\Omega(\mathbf{r})\cdot\epsilon_\Omega(\mathbf{r}-\Lambda\hat{z})\mathbf{E}_\Omega(\mathbf{r}-\Lambda\hat{z}) \tag{6.7b}$$

$$d = \int \mathrm{d}^3\mathbf{r}\mathbf{E}^*_\Omega(\mathbf{r})\cdot\epsilon(\mathbf{r})\mathbf{E}_\Omega(\mathbf{r}-\Lambda\hat{z}) \tag{6.7c}$$

$$\sigma_m = \int \mathrm{d}^3\mathbf{r}\mathbf{E}^*_\Omega(\mathbf{r})\cdot\sigma(\mathbf{r})\mathbf{E}_\Omega(\mathbf{r}) \tag{6.7d}$$

$$\Delta\sigma_m = \int \mathrm{d}^3\mathbf{r}\mathbf{E}^*_\Omega(\mathbf{r})\cdot\sigma(\mathbf{r})\mathbf{E}_\Omega(\mathbf{r}-\Lambda\hat{z}) \tag{6.7e}$$

$$p_m = \int \mathrm{d}^3\mathbf{r}\mathbf{E}^*_\Omega(\mathbf{r}-m\Lambda\hat{z})\cdot\mathbf{p}(\mathbf{r}). \tag{6.7f}$$

To simplify the algebra, we have assumed $\epsilon(\mathbf{r}) \approx \epsilon(\mathbf{r}\pm\Lambda\hat{z})$, which is true only for infinitely long structures. The approximation holds the worst for the first and last resonator in a finite CROW. This means that the constants in Eq. (6.7) at the first and last resonator are slightly different compared to resonators in the center of the chain.

If $\Delta\alpha$, $|\sigma_m| \ll 1$ and $\omega \approx \Omega$, such that both the gain and the coupling are weak, Eq. (6.6) becomes

$$i\dot{a}_m = a_m\left[(\omega-\Omega')+i\frac{\omega\sigma_m}{2}\right] + \kappa_t a_{m+1} + \kappa_t^* a_{m-1} - \frac{\ddot{p}_m}{2\omega}\exp(-i\omega t), \tag{6.8}$$

where $\Omega' = \Omega - \omega\Delta\alpha/2$, and $\kappa_t = \omega/2(d-b)$, or

$$\kappa_t = \frac{\omega}{2}\int \mathrm{d}^3\mathbf{r}\mathbf{E}_\Omega^*(\mathbf{r})\left[\epsilon(\mathbf{r}+m\Lambda\hat{z}) - \epsilon_\Omega(\mathbf{r}-\Lambda\hat{z})\right]\mathbf{E}_\Omega(\mathbf{r}-\Lambda\hat{z}). \tag{6.9}$$

In reaching Eq. (6.8), we neglected terms that vary with $\Delta\sigma_m$ by assuming that the coupling through the real part of the susceptibility dominates. However, in the case where $\Delta\sigma_m$ cannot be neglected, the coupling constant will be a complex with an imaginary part given by $i\omega\Delta\sigma_m/2$.

Because a CROW consisting of weakly coupled resonators is a narrowband device, if we consider only the noise in the frequency range of a single propagation band, the noise term, $p_m(t)$ can be approximated as a slowly varying quantity, so it can be expressed as $p_m(t) = 2s_m(t)\exp(i\omega t)$ and $\ddot{p}_m \approx -2\omega^2 s_m(t)\exp(i\omega t)$. With this final approximation and choosing the phase such that $\mathbf{E}_\Omega$ is real and $\kappa_t = \kappa_t^*$, we finally arrive at the typical time domain coupled oscillator equation,

$$\dot{a}_m = a_m\left[-i(\omega-\Omega') + \frac{1}{\tau_i}\right] - i\kappa_t(a_{m+1}+a_{m-1}) - i\omega s_m(t), \tag{6.10}$$

where we have defined $1/\tau_i \equiv \omega\sigma_m/2$. $\tau_i > 0$ represents gain while $\tau_i < 0$ represents loss.

Throughout our derivation, we have highlighted the approximations that are embodied by Eq. (6.10). These approximations are justified in the regime of weak inter-resonator coupling and small values of gain or loss. In the limit of high gain or high field intensities, light propagation becomes nonlinear because of saturation. To deal with large coupling strengths, transfer matrices as described in Chapters 2 and 7 are an alternative analytical approach.

6.3 Gain Enhancement and Boundary Conditions

In this section, we will use the coupled oscillator equation, Eq. (6.10), derived in the previous section to understand the role of coupled resonances on the net gain

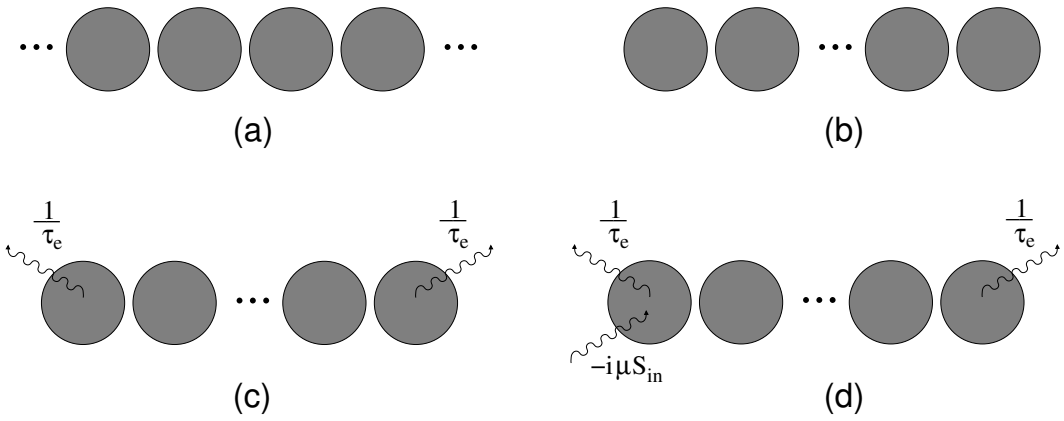

Figure 6.1: Various configurations of coupled resonators: (a) infinitely long CROWs, (b) finite CROWs in isolation, (c) finite CROWs with out-coupling at the ends, and (d) finite CROWs with an input optical field with out-coupling at the ends

of an amplifying CROW. We shall neglect the noise contribution here and examine the steady-state response, so $s_m(t) = 0$ and $\dot{a}_m = 0$ in Eq. (6.10). Our results will show that gain enhancement is strongly dependent on the boundary conditions and excitation of the coupled resonators. We will examine the scenarios illustrated in Fig. 6.1: (a) infinite structures, (b) finite structures in isolation of additional dissipative pathways, (c) finite structures with additional dissipation (such as input/output waveguides), and (d) finite structures driven by input optical fields.

6.3.1 Infinitely Long Structures

An infinitely long CROW is schematically depicted in Fig. 6.1(a). The eigenmodes of infinitely long structures satisfy Bloch boundary conditions so $a_{m+1} = a_m \exp(-iK\Lambda)$, where K is the Bloch wave-vector. K can be complex and can be expressed as $K = K_R + iK_I$. Substituting this form of the solution into Eq. (6.10), we have equations for the real and imaginary parts of Eq. (6.10):

$$(\omega - \Omega') = -2\kappa_t \cos(K_R\Lambda)\cosh(K_I\Lambda), \tag{6.11a}$$

$$-\frac{1}{\tau_i} + 2\kappa_t \sin(K_R\Lambda)\sinh(K_I\Lambda) = 0. \tag{6.11b}$$

In the absence of loss or gain, $K_I = 0$ in the propagation band. Therefore, the group velocity, $v_g = \mathrm{d}\omega/\mathrm{d}K = 2\kappa_t \Lambda \sin(K_R \Lambda)$, and Eq. (6.11b) becomes

$$\sinh(K_I \Lambda) = \frac{\Lambda}{2\tau_i v_g}. \tag{6.12}$$

As $v_g \to 0$, $K_I \to \infty$, meaning that the field is most amplified (or attenuated) at the band-edges. For small values of $K_I\Lambda$, near the band-center, $K_I\Lambda \approx \frac{\Lambda}{2\tau_i v_g}$ and scales linearly with v_g. Therefore, for infinitely long structures, the gain (loss) of the Bloch modes of the coupled resonators are enhanced compared to the the gain (or loss) of the constituent resonators by a factor of $1/v_g$. This result agrees well with conventional arguments in describing band-edge laser action and gain enhancement in photonic crystals where the analysis often begins with the Bloch modes of the structures [129, 130, 131].

6.3.2 Finite Structures

Naturally, infinitely long structures are not realizable in practice. In this subsection, we shall show that even if the finite structures contain a very large number of periods, the modes can behave significantly differently compared to the Bloch modes. In particular, the termination or boundary conditions play perhaps the most important role in determining the net gain (loss) in the coupled resonator chains.

The field amplitudes in finite structures can be solved by expressing Eq. (6.10) in terms of a matrix equation. For convenience, we define $\mathbf{a} \equiv \begin{bmatrix} a_1 & a_2 & . & . & . & a_N \end{bmatrix}^T$. In the following sections, we shall find the fields of finite CROWs with various boundary conditions.

6.3.2.1 Clamped Boundaries

First, we examine the modes of a finite CROW with no external coupling to dissipation channels in addition to the intrinsic gain/loss rate of $1/\tau_i$. This situation is depicted in Fig. 6.1(b). In this scenario, because of the finite length the CROW, the fields are

"clamped" to zero at the boundaries, or $a_0 = 0$ and $a_{N+1} = 0$. The matrix equation that describes this system is

$$i\omega\mathbf{a} = \begin{bmatrix} i\Omega' + \frac{1}{\tau_i} & -i\kappa_t & 0 & 0 & ... & 0 & 0 \\ -i\kappa_t & i\Omega' + \frac{1}{\tau_i} & -i\kappa_t & 0 & ... & 0 & 0 \\ . & . & . & . & . & . & . \\ . & . & . & . & . & . & . \\ . & . & . & . & . & -i\kappa_t & i\Omega' + \frac{1}{\tau_i} \end{bmatrix} \mathbf{a}. \tag{6.13}$$

The eigenvalues, ω_n, and the elements of the eigenvectors, a_m, of Eq. (6.13) are [1]

$$\omega_n = \left(\Omega' - \frac{i}{\tau_i}\right) - 2\kappa_t \cos\left(\frac{n\pi}{N+1}\right), \quad n = 1 \ldots N \tag{6.14a}$$

$$\mathsf{a}_m^{(n)} = \sin\left(m\frac{n\pi}{N+1}\right), \quad m = 1 \ldots N. \tag{6.14b}$$

From Eq. (6.14a), the real part of ω_n gives the dispersion relation of the structure as $N \to \infty$. However, the imaginary part of all the eigenvalues are identical and equal $-i/\tau_i$, independent of the $n\pi/(N+1)$. Therefore, regardless of how many resonators are in the chain, all the modes experience equal amplification and dissipation rates. Unlike the Bloch modes of Section 6.3.1, there is no additional enhancement of the gain (loss) that arises from the coupling between the resonators compared to the intrinsic gain (loss) of the individual resonators. Physically, this result is not surprising because these boundary conditions imply the modes of the finite CROW are isolated from the external world, so the fields of the CROW grow (or decay) at the same rate as its constituent resonators.

6.3.2.2 Free Boundaries

Next, we shall allow for additional dissipation in the CROW. Most typically, this corresponds to the scenario where light is coupled out somewhere in the CROW via waveguides for example. We will now examine the specific case where this out-coupling occurs at the first and last element in the CROW as shown in Fig. 6.1(c),

though our approach can be easily generalized to out-coupling at other elements. Because we shall allow for additional dissipation at the ends of the CROW, the fields are no longer clamped at the boundaries and are "free."

For these boundary conditions, we can express the fields as

$$i\omega\mathbf{a} = \begin{bmatrix} i\Omega' + \frac{1}{\tau_i} - \frac{1}{\tau_e} & -i\kappa_t & 0 & 0 & ... & 0 & 0 \\ -i\kappa_t & i\Omega' + \frac{1}{\tau_i} & -i\kappa_t & 0 & ... & 0 & 0 \\ . & . & . & . & . & . & . \\ . & . & . & . & . & . & . \\ . & . & . & . & . & -i\kappa_t & i\Omega' + \frac{1}{\tau_i} - \frac{1}{\tau_e} \end{bmatrix} \mathbf{a}, \tag{6.15}$$

where $1/\tau_e > 0$ is the additional loss rate to the external world. In general, the eigenvalues of Eq. (6.15) are found numerically. However, we can readily find an explicit analytical expression using our results from Eq. (6.14) if $1/\tau_e$ can be accounted for perturbatively.

Perturbatively, the first-order correction to Eq. (6.14a) due to $1/\tau_e$ is given by $\mathsf{a}_n^T W \mathsf{a}_n$, where a_n is the normalized eigenvector and W is the perturbation. The resultant eigenvalues are

$$\omega_n \approx \Omega' + 2\kappa_t \cos\left(\frac{n\pi}{N+1}\right) + i\left[-\frac{1}{\tau_i} + \frac{2}{\tau_e}\frac{\sin^2\left(\frac{n\pi}{N+1}\right)}{\sum_{m=1}^{N}\sin^2\left(m\frac{n\pi}{N+1}\right)}\right]. \tag{6.16}$$

Eq. (6.16) shows that $1/\tau_i$ again does not scale with $n/(N+1)$, thus there is no gain enhancement that depends on $1/v_g$. However, the rate of amplification is indeed higher at the band-edges ($n \approx 0, N$) compared to the band-center, because for $\tau_i > 0$, the imaginary part of ω_n is more negative at the band-edges compared to the band-center. Nonetheless, this increased gain at the band-edges is wholly determined by the external coupling.

Fig. 6.2 illustrates this result, where we have the numerically computed eigenvalues of Eq. (6.15) and the eigenvalues described by Eq. (6.16) for the parameters described in the caption. The parameters are normalized to Ω'. The rate of amplifi-

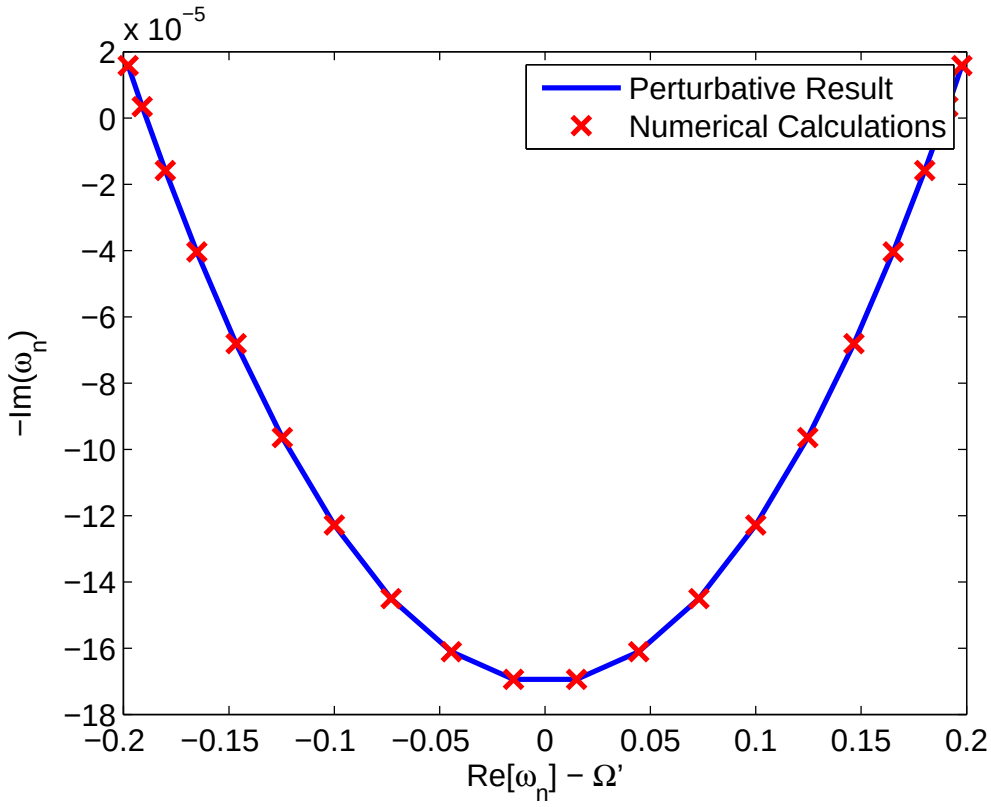

Figure 6.2: $-\mathrm{Im}[\omega_n]$ vs. $\mathrm{Re}[\omega_n] - \Omega'$ for a CROW with out-coupling at the two ends. $\tau_e = 10^4$, $\tau_i = 5 \times 10^4$, $\kappa_t = 0.1$, and $N = 20$.

cation is given by $-\mathrm{Im}[\omega_n]$ and is plotted against $\mathrm{Re}[\omega_n] - \Omega'$. As evidenced by the figure, the frequencies near the band-edge experience an increased rate of amplification proportional to the out-coupling rate.

Physically, we can interpret the $1/\tau_e$ term in Eq. (6.16) as the effective rates of dissipation or out-coupling of the various CROW modes described by Eq. (6.14). This effective rate is smallest at the band-edges and largest at the band-center as though the termination is lower loss (more "reflective") for the lower v_g modes [132].

6.3.2.3 Forced Coupled Oscillators

Thus far, we have only examined eigenmodes of infinite and finite CROWs. The eigenmodes are useful when an input optical wave indeed excites superpositions of these modes. In this section, we examine the transmission of a CROW amplifier

where the first resonator is excited by an input wave and the output is detected at the last resonator as in Fig. 6.1(d).

To model the presence of an input source, we add a driving term to the first resonator, $-i\mu S_{in}$, where μ describes the strength of the coupling between the input wave and the resonator. Thus, the matrix equation becomes

$$\begin{aligned} i\omega\mathbf{a} &= \begin{bmatrix} i\Omega' + \frac{1}{\tau_i} - \frac{1}{\tau_e} & -i\kappa_t & 0 & 0 & ... & 0 & 0 \\ -i\kappa_t & i\Omega' + \frac{1}{\tau_i} & -i\kappa_t & 0 & ... & 0 & 0 \\ . & . & . & . & . & . & . \\ . & . & . & . & . & . & . \\ . & . & . & . & . & -i\kappa_t & i\Omega' + \frac{1}{\tau_i} - \frac{1}{\tau_e} \end{bmatrix} \mathbf{a} - i\mu \begin{bmatrix} S_{in} \\ 0 \\ . \\ . \\ 0 \end{bmatrix} \\ &\equiv \mathsf{M}\mathbf{a} - i\mu\mathbf{s}_{in}. \end{aligned} \tag{6.17}$$

Therefore, the amplitudes in the resonators are given by

$$\mathbf{a} = -i\mu(i\omega\mathsf{I} - \mathsf{M})^{-1}\mathbf{s}_{in} \equiv -i\mu\mathsf{T}\mathbf{s}_{in}. \tag{6.18}$$

The transmitted amplitude, S_t, is proportional to the amplitude in the last resonator which is given by $a_N = -i\mu\mathsf{T}_{N,1}S_{in}$.

The constant of proportionality between S_t and a_N is determined from the conservation of energy in the absence of gain and loss. For example, we can consider a single resonator where the rates of out-coupling to the input and output waveguides are identical. If the magnitude of the field amplitude at the output is equal to the input on resonance, then from Eq. (6.10)

$$-\frac{2}{\tau_e}a_1 - i\mu S_{in} = 0. \tag{6.19}$$

The factor of 2 is due to out-coupling to both input and output waveguides. If $|S_t|^2 = |S_{in}|^2$, as in the case of ring resonators in the add-drop configuration [5], then $|S_t|^2 = |2/(\tau_e\mu)a_1|^2$ and $|\bar{\kappa}| = |2/(\tau_e\mu)|$ is the fraction of field amplitude inside the

resonator leaked out to the output waveguide. For standing wave resonators, $|S_t|^2$ is divided into four output channels (two at the start of the CROW and two at the end) [133]. Therefore, generalizing to a CROW using Eq. (6.18), the transmitted amplitude is

$$\left|\frac{S_t}{S_{in}}\right|^2 = \left|\frac{2}{\tau_e}\mathsf{T}_{N,1}\right|^2. \tag{6.20}$$

The matrix element, $\mathsf{T}_{N,1}$, is explicitly given by [134]

$$\mathsf{T}_{N,1} = \frac{\kappa_t \sin(\phi)}{i/\tau_e^2 \sin((N-1)\phi) + 2\kappa_t/\tau_e \sin(N\phi) - i\kappa_t^2 \sin((N+1)\phi)} \tag{6.21a}$$

$$\cos(\phi) = -\frac{(\omega - \Omega')}{2\kappa_t} - \frac{i}{2\kappa_t\tau_i}, \tag{6.21b}$$

for $\tau_i \neq 0$. At the band-edges, $\cos(\phi_{be}) = \pm 1 - i/(2\kappa_t\tau_i)$, and at the band-center, $\cos(\phi_{bc}) = -i/(2\kappa_t\tau_i)$. This equation can be solved numerically. However, from Eqs. (6.20) and (6.21), we see that the transmitted amplitude depends solely on $\kappa_t\tau_e$ at a fixed ϕ. Thus, the net gain or loss experienced by the transmitted field can be changed via τ_e.

Fig. 6.3 shows the numerically calculated transmission amplitude using Eq. (6.21) for various values of $1/\tau_e$. The other parameters for the calculations are described in the figure caption. As evidenced by the plot, the net gain of a wave and its transmittance is controlled by τ_e.

Although Eq. (6.21) should in general be solved numerically, we can easily find some approximate results in the case of loss, $\tau_i < 0$, for which the equation does not possess any poles. In the regime where $1/(\kappa_t|\tau_i|) \ll 1$ and $N/(2\kappa_t|\tau_i|) \gg 1$, after some algebra, the transmitted amplitude at the band-center is approximately given by

$$\left|\frac{S_t}{S_{in}}\right|_{bc} \approx \frac{4e^{\frac{N}{2\kappa_t\tau_i}}}{1/(\kappa_t\tau_e) + 2 + \kappa_t\tau_e} \qquad \tau_i < 0. \tag{6.22}$$

Eq. (6.22) gives the transmittance with loss and is in agreement with the heuristic argument presented in Chapter 3 when $\kappa_t \approx 1/\tau_e$. Fig. 6.4 shows the transmittance as a function of the number of resonators at the band-center frequency, $\omega = \Omega'$,

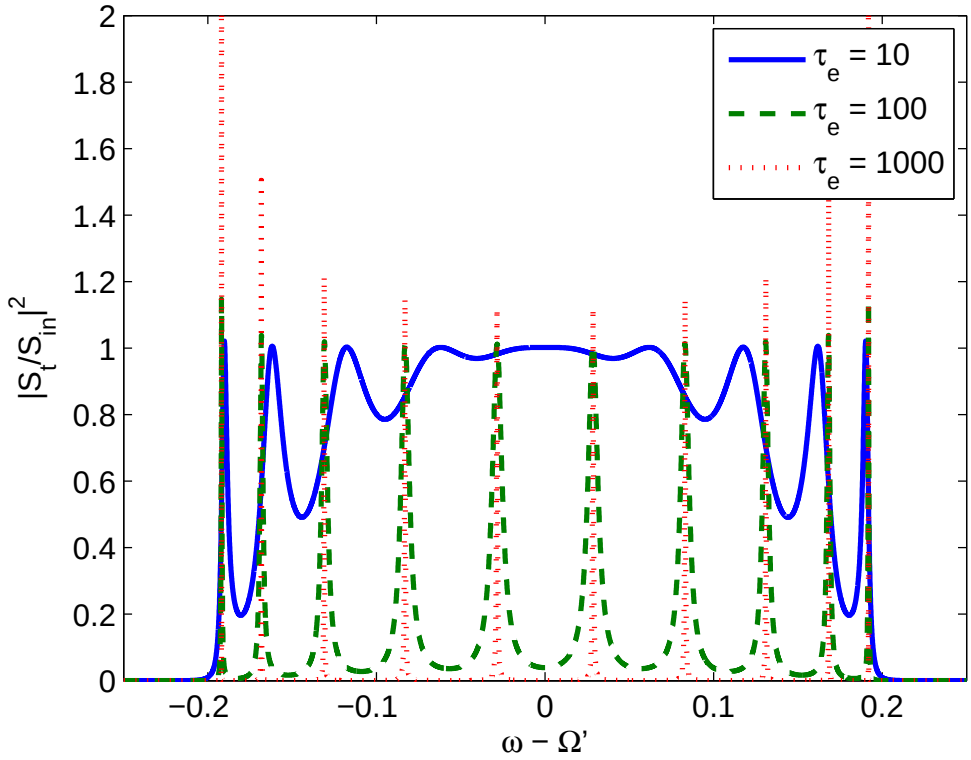

Figure 6.3: The transmittance, $|S_t/S_{in}|^2$, of CROWs for various values of τ_e. The other parameters are $\tau_i = 5 \times 10^4$, $\kappa_t = 0.1$, and $N = 10$. Only the portion of $|S_t/S_{in}|^2 \leq 2$ is shown for comparison.

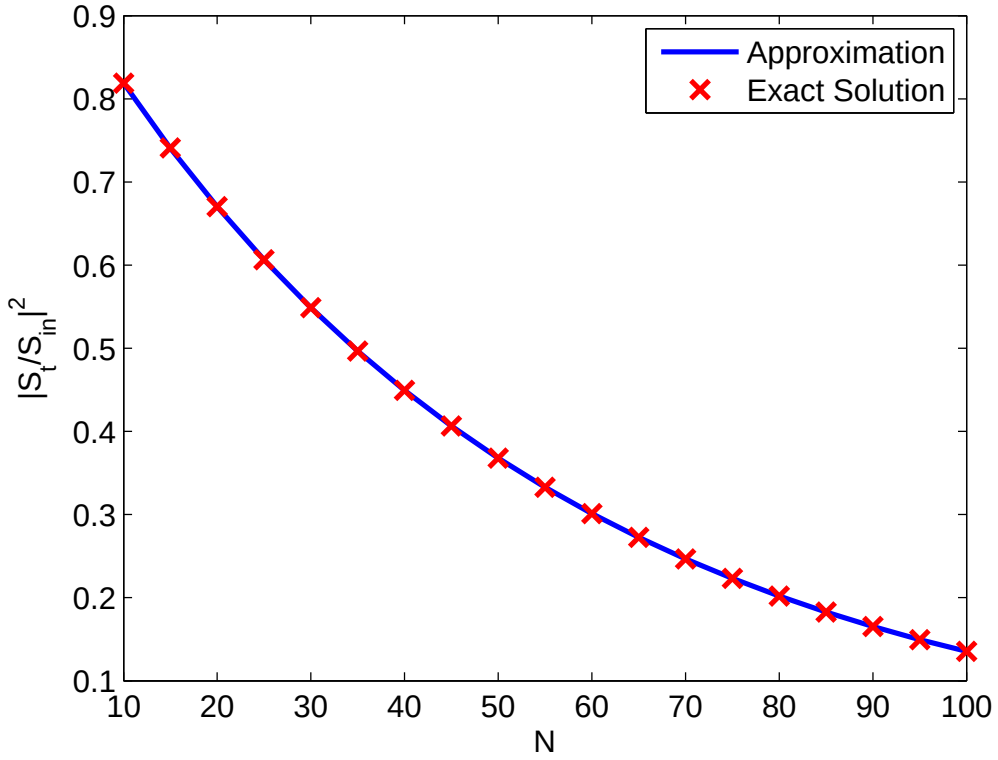

Figure 6.4: The exact solution of the transmittance from Eq. (6.21) and the approximation given by Eq. (6.22) as a function of the number of resonators (N) at the band-center frequency with optical loss. The other parameters are $\tau_i = -5 \times 10^3$, $\kappa_t = 0.01$, $\tau_e = 1/\kappa_t = 100$.

computed using Eq. (6.21) and Eq. (6.22). The plot shows that Eq. (6.22) is an excellent approximation to Eq. (6.21).

6.4 Spontaneous Emission Noise

In optically amplifying devices, it is important to consider the effect of noise from the spontaneous emission which degrades the signal-to-noise ratio. Using the formalism we developed in Section 6.2, we can explicitly examine the effect of spontaneous emission in a CROW. We will make frequent use of the Fourier transform in this

section, which we define as

$$f(t) = \int_{-\infty}^{\infty} \tilde{f}(\tilde{\omega}) \exp(i\tilde{\omega}t) \mathrm{d}\tilde{\omega}, \tag{6.23a}$$

$$\tilde{f}(\tilde{\omega}) = \frac{1}{2\pi} \int_{-\infty}^{\infty} f(t) \exp(-i\tilde{\omega}t) \mathrm{d}t. \tag{6.23b}$$

We begin in the tight-binding picture with Eq. (6.10). Spontaneous emission causes small fluctuations in the polarization density in the medium and is represented by $s_m(t)$. From Eq. (6.10), we can see that the spontaneous emission is manifested as a small amplitude input at each resonator, which can then propagate and be amplified in the CROW. A simple way to analyze the noise is to work in the frequency domain such that we will have a linear set of equations. Taking the Fourier transform of Eq. (6.10), we have

$$i\tilde{\omega}\tilde{a}_m = \tilde{a}_m \left[-i\Delta + \frac{1}{\tau_i} \right] - i\kappa_t(\tilde{a}_{m+1} + \tilde{a}_{m-1}) - i\omega\tilde{s}_m, \tag{6.24}$$

where $\tilde{a}_m$, $\tilde{a}_{m\pm1}$, $\tilde{s}_m$ are the Fourier amplitudes of a_m, s_m, and $a_{m\pm1}$ respectively, $\tilde{\omega}$ is a frequency much lower than the optical frequency, and $\Delta \equiv \omega - \Omega'$. Eq. (6.24) can now be solved as a matrix equation to find $\tilde{a}_m$ given the $\tilde{s}_m$'s.

6.4.1 Normalization of $\tilde{s}_m(\tilde{\omega})$

The normalization of $\tilde{s}_m$ is related to the amount of spontaneous emission. We can readily determine $\tilde{s}_m$ of each resonator by assuming there is no additional input wave and taking $\kappa_t = 0$. For clarity, we separate the contributions of the gain/absorption (due to induced transitions) and the intrinsic loss of the resonator:

$$1/\tau_i = 1/\tau_g - 1/\tau_l, \tag{6.25}$$

where $1/\tau_g$ gives the amplification/absorption rate of the active medium and $1/\tau_l$ is the intrinsic loss rate. $1/\tau_g$ depends on the inversion of the material and can be

negative or positive depending on the pumping. $1/\tau_l$ is a positive quantity.

At the material transparency, $1/\tau_g = 0$, the spontaneously emitted wave, $\tilde{a}_{sp}$, at the resonant frequency is

$$i\tilde{\omega}\tilde{a}_{sp,m} = -\frac{1}{\tau_l}\tilde{a}_{sp,m} - i\Omega\tilde{s}_m, \tag{6.26}$$

and its magnitude is

$$|\tilde{a}_{sp,m}|^2 = \frac{\Omega^2}{\tilde{\omega}^2 + 1/\tau_l^2}|\tilde{s}_m|^2. \tag{6.27}$$

The instantaneous energy of the spontaneous emission is

$$U_{sp,m}(t) = |a_{sp,m}(t)|^2 \int \mathrm{d}^3\mathbf{r}\epsilon_0\epsilon_\Omega(\mathbf{r})\,|E_\Omega(\mathbf{r})|^2 = |a_{sp,m}(t)|^2\,V \tag{6.28}$$

where $V \equiv \epsilon_0 \int d^3\mathbf{r}\epsilon_\Omega(\mathbf{r})\,|E_\Omega(\mathbf{r})|^2$. Therefore, from the Weiner-Khintchine theorem, the average energy is

$$\begin{aligned}\langle U_{sp,m}\rangle &= \lim_{T\to\infty}\frac{1}{T}\int_{-T/2}^{T/2}\mathrm{d}tU_{sp,m}(t)\\ &= \lim_{T\to\infty}\frac{2\pi V}{T}\int \mathrm{d}\tilde{\omega}|\tilde{a}_{sp,m}(\tilde{\omega})|^2,\end{aligned} \tag{6.29}$$

where T is interpreted as the measurement integration time [1]. However, the spontaneous emission power into an ideal single uncoupled resonator is $P_{sp,m} \approx R_{sp,m}\hbar\Omega$, where $R_{sp,m}$ is the rate of spontaneous emission. $R_{sp,m}$ is a function of the pump rate and can be modified compared to bulk dielectrics by the Purcell factor [127]. As the coupling to its neighbors increases, $R_{sp,m}$ of a single cavity will be modified. For simplicity, let us assume that the resonators are sufficiently weakly coupled that $R_{sp,m}$ does not change appreciably in the coupled resonator chain. Since the spontaneous emission dissipates from the resonator at a rate of $2/\tau_l$,

$$\langle U_{sp,m}\rangle = \frac{P_{sp,m}\tau_l}{2} = \frac{R_{sp,m}\hbar\Omega\tau_l}{2}. \tag{6.30}$$

Therefore, using Eqs. (6.27), (6.29), and (6.30), as $1/\tau_l \to 0$ (i.e., small values of

intrinsic loss), we arrive at the normalization condition

$$\lim_{T\to\infty} \frac{|\tilde{s}_m(0)|^2}{T} = \frac{\hbar R_{sp,m}}{4\pi^2 V\Omega}, \tag{6.31}$$

where we have used the identity $\lim_{\epsilon\to 0} \epsilon/(x^2+\epsilon^2) = \pi\delta(x)$. It is important to note that $R_{sp,m}$, τ_l, and τ_g are not independent of each other and are related through the cavity losses and the carrier densities. In the next section, we will use the result in Eq. (6.31) to derive the signal-to-noise ratio in active CROWs.

6.4.2 Signal-to-Noise Ratio

An important metric of propagating optical signals in any amplifying structure with gain is the signal-to-noise ratio (SNR). SNR in non-resonant and Fabry-Perot amplifiers as well as noise in multi-element lasers have been studied [1, 128, 135, 136, 137]. Here, we use our tight-binding formalism to derive expressions for the SNR of a CROW amplifier. In particular, we will focus on the case described in Section 6.3.2.3 where the CROW is excited by an input wave at the first resonator and the signal is detected at the output at the last resonator. Our approach can be easily extended to other excitation conditions and boundary conditions.

We begin with the matrix form of Eq. (6.24) with an input in the first resonator,

so

$$\begin{bmatrix} -i(\tilde{\omega}+\Delta)+\frac{1}{\tau_i}-\frac{1}{\tau_e} & -i\kappa_t & 0 & 0 & ... & 0 & 0 \\ -i\kappa_t & -i(\tilde{\omega}+\Delta)+\frac{1}{\tau_i} & -i\kappa_t & 0 & ... & 0 & 0 \\ . & . & . & . & . & . & . \\ . & . & . & . & . & . & . \\ . & . & . & . & . & -i\kappa_t & -i(\tilde{\omega}+\Delta)+\frac{1}{\tau_i}-\frac{1}{\tau_e} \end{bmatrix} \tilde{\mathbf{a}}$$

$$-i\omega \begin{bmatrix} \tilde{s}_1 \\ \tilde{s}_2 \\ . \\ . \\ \tilde{s}_N \end{bmatrix} - i\mu \begin{bmatrix} \tilde{S}_{in} \\ 0 \\ . \\ . \\ 0 \end{bmatrix} = 0, \tag{6.32a}$$

$$\tilde{\mathbf{a}} = -i\omega \mathsf{P}^{-1}\tilde{\mathbf{s}} - i\mu \mathsf{P}^{-1}\tilde{\mathbf{s}}_{in}, \tag{6.32b}$$

where P is the $N \times N$ matrix in Eq. (6.32a), $\tilde{\mathbf{s}}$ are the spontaneous emission noise sources, and $\tilde{\mathbf{s}}_{in}$ is the input signal. For an input of the form $\tilde{\mathbf{s}}_{in} = \begin{bmatrix} \tilde{S}_{in} & 0 & 0...0 \end{bmatrix}^T$, the amplitude at the Nth resonator is

$$|a_N(\tilde{\omega})|^2 = \mu^2 |\mathsf{P}^{-1}_{N,1}\tilde{S}_{in}|^2 + \omega^2 \sum_{j=1}^{N} |\mathsf{P}^{-1}_{N,j}\tilde{s}_j|^2 - \left[\omega\mu (\mathsf{P}^{-1}_{N,1})^* \sum_{j=1}^{N} \mathsf{P}^{-1}_{N,j}\tilde{s}_j \tilde{S}^*_{in} + c.c \right]. \tag{6.33}$$

Eq. (6.33) gives the total magnitude of the field at the Nth resonator. We note that the first term on the right side is the signal, the second term is the spontaneous emission, and the last term corresponds to the beating between the input and the spontaneous emission. For strong input powers and weak amplification, the beat noise dominates. We shall proceed to analyze this ideal case where the spontaneous emission signal beat noise is dominant. The other noise term can be dealt with easily in a similar fashion.

The noise current from the beating is given by

$$i_n(\tilde{\omega}) = -\eta\omega\mu(\mathsf{P}_{N,1}^{-1})^* \sum_{j=1}^{N} \mathsf{P}_{N,j}^{-1}\tilde{s}_j\tilde{S}_{in}^* + c.c., \tag{6.34}$$

where η is the responsivity of the detector and accounts for the normalization of a_n. The mean electrical noise power is given by $\langle i_n^2 \rangle$, which, using the Weiner-Khintchine theorem, is

$$\begin{aligned}\langle i_n^2 \rangle =& \eta^2 \lim_{T\to\infty} \frac{1}{T} \int \mathrm{d}\tilde{\omega} 2\omega^2\mu^2 |\mathsf{P}_{N,1}^{-1}\tilde{S}_{in}|^2 \sum_{j,k=1}^{N} \mathsf{P}_{N,j}^{-1}(\mathsf{P}_{N,k}^{-1})^*\tilde{s}_j\tilde{s}_k^* \\ &+ \omega^2\mu^2 2\mathrm{Re}\left[(\mathsf{P}_{N,1}^{-1})^{*2}\tilde{S}_{in}^{*2} \sum_{j,k=1}^{N} \mathsf{P}_{N,j}^{-1}\mathsf{P}_{N,k}^{-1}\tilde{s}_j\tilde{s}_k\right].\end{aligned} \tag{6.35}$$

Since the spontaneous emission noise is not correlated in amplitude and phase, $\int d\tilde{\omega}\tilde{s}_l^*(\tilde{\omega})\tilde{s}_m(\tilde{\omega}) \propto \delta_{l,m}$, where $\delta_{l,m} = 0$ for $l \neq m$ and 1 for $l = m$. Therefore, Eq. (6.35) simplifies to

$$\langle i_n^2 \rangle = \eta^2 \lim_{T\to\infty} \frac{1}{T} \int d\tilde{\omega} 2\omega^2\mu^2 |\mathsf{P}_{N,1}^{-1}\tilde{s}_{in}|^2 \sum_{j=1}^{N} |\mathsf{P}_{N,j}^{-1}\tilde{s}_j|^2. \tag{6.36}$$

If we only consider a narrow-band signal and noise contributions within this narrow bandwidth, the integral in the above equation can be approximated by the product of the integrand at $\tilde{\omega} = 0$ and the bandwidth, $\Delta\tilde{\omega}$. So

$$\begin{aligned}\langle i_n^2 \rangle &\approx \eta^2 \lim_{T\to\infty} \frac{1}{T} \left[2\omega^2\mu^2 |\mathsf{P}_{N,1}^{-1}\tilde{S}_{in}|^2 \sum_{j=1}^{N} |\mathsf{P}_{N,j}^{-1}\tilde{s}_j|^2 \Delta\tilde{\omega}\right]_{\tilde{\omega}=0} \\ &= \omega^2\mu^2 |\mathsf{T}_{N,1}\tilde{S}_{in}(0)|^2 \sum_{j=1}^{N} |\mathsf{T}_{N,j}|^2 \frac{\hbar R_{sp,j}}{2\pi^2 V\Omega}\Delta\tilde{\omega},\end{aligned} \tag{6.37}$$

where we have substituted the result from Eq. (6.31) and the matrix T was defined in Section 6.3.2.3.

To find the SNR, we first note that the signal is given by

$$\langle i_{in}^2 \rangle = \eta^2 \mu^4 \lim_{T\to\infty} \frac{2\pi}{T} \int \mathrm{d}\tilde{\omega} |\mathsf{P}_{N,1}^{-1} \tilde{S}_{in}|^4 \approx \eta^2 \mu^4 \lim_{T\to\infty} \frac{2\pi}{T} |\mathsf{T}_{N,1} \tilde{S}_{in}(0)|^4 \Delta\tilde{\omega}, \tag{6.38}$$

where the second part of the equation is with the narrowband approximation. Therefore, if the resonators are identical so $R_{sp,j} = R_{sp}$, the SNR is

$$\mathrm{SNR} = \frac{4\pi^3 V \Omega \mu^2 |\mathsf{T}_{N,1}|^2}{\hbar\omega^2 R_{sp} \sum_{j=1}^{N} |\mathsf{T}_{N,j}|^2} \cdot \lim_{T\to\infty} \frac{|\tilde{S}_{in}(0)|^2}{T}. \tag{6.39}$$

$\lim_{T\to\infty} |\tilde{S}_{in}(\tilde{\omega})|^2/T$ is the power spectral density of the input, so the rightmost term in the above equation refers to the input power at ω.

Physically, Eq. (6.39) states that the beat noise at any frequency at the output is simply the sum of the transmitted magnitudes of spontaneous emission originating from each resonator in the CROW. The key difference between a CROW and a non-resonant amplifier is that the SNR can vary dramatically at different signal frequencies because T can be a strong function of the wavelength. To have an acceptable SNR, the matrix elements, $|\mathsf{T}_{N,j}|^2$, should have a small magnitude. This can be achieved if resonators are not high loss to begin with so the gain can be kept weak. A reduced pump rate also reduces R_{sp}.

Fig. 6.5 shows the normalized SNR factor, $G = \frac{R_{sp0}|\mathsf{T}_{N,1}|^2}{R_{sp}\sum_{j=1}^{N}|\mathsf{T}_{N,j}|^2}$ as a function of wavelength for various values of τ_g. R_{sp0} is the spontaneous emission rate when $\tau_i = 0$ or $\tau_{g0} = \tau_l$. For weak, unsaturated gain, $R_{sp0}/R_{sp} \approx \tau_g/\tau_{g0}$ since both R_{sp} and $1/\tau_g$ vary linearly with the pump rate. τ_l is taken to be a constant at 10^4. As evidenced by the figure, a higher gain leads to a reduction in the SNR. The SNR is also highest at the band-center and lowest at the band-edges.

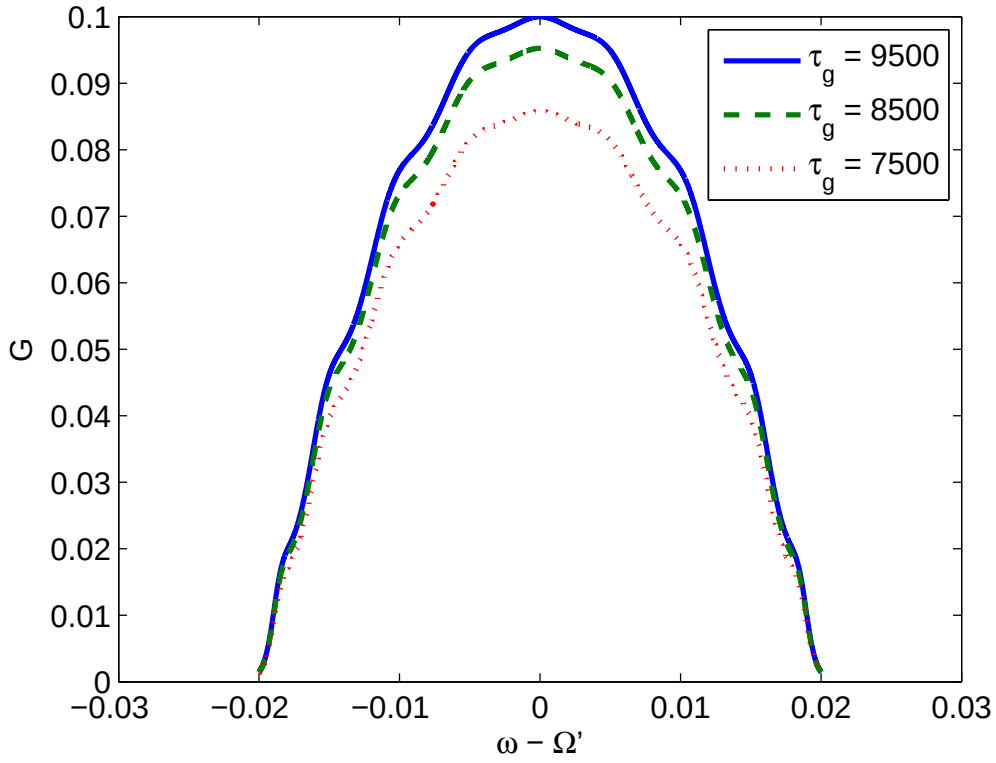

Figure 6.5: The normalized SNR factor, G, as a function of wavelength at various gain levels. For the calculations, $\tau_l = 10^4$, $\kappa_t = 0.01$, $\tau_e = 100$, $N = 10$.

6.4.3 Noise Figure

A second parameter that characterizes the performance of an amplifier is the noise figure. The noise figure, NF, is defined as

$$\mathrm{NF} = \frac{\mathrm{SNR}_{\mathrm{in}}}{\mathrm{SNR}_{\mathrm{out}}}, \tag{6.40}$$

where $\mathrm{SNR}_{\mathrm{in}}$ is the SNR at the input of the amplifier and $\mathrm{SNR}_{\mathrm{out}}$ is the SNR at the output. To determine NF, we simply need to define our input as $S_{in} = S_{sig} + S_{\delta}$, where S_{sig} is the field amplitude of the signal and S_{δ} is the field amplitude of the noise.

Substituting this form of the input into Eq. (6.38), and assuming a narrow bandwidth signal, we find

$$\mathrm{SNR}_{\mathrm{in}} = \frac{|\tilde{S}_{sig}(0)|^2}{2|\tilde{S}_{\delta}(0)|^2}. \tag{6.41}$$

At the output, using Eq. (6.39), we have

$$\mathrm{SNR}_{\mathrm{out}} = \frac{4\pi^3 V\Omega\mu^2|\mathsf{T}_{N,1}|^2}{\hbar\omega^2 R_{sp}\sum_{j=1}^{N}|\mathsf{T}_{N,j}|^2} \cdot \lim_{T\to\infty}\frac{|\tilde{S}_{sig}(0)|^2 + |\tilde{S}_{\delta}(0)|^2}{T}. \tag{6.42}$$

Therefore, the noise figure, in the limit $|\tilde{S}_{\delta}(0)|^2 \ll |\tilde{S}_{sig}(0)|^2$, is

$$\mathrm{NF} = \frac{\hbar\omega^2 R_{sp}\sum_{j=1}^{N}|\mathsf{T}_{N,j}|^2}{4\pi^3 V\Omega\mu^2|\mathsf{T}_{N,1}|^2} \cdot \lim_{T\to\infty}\frac{T}{2|\tilde{S}_{\delta}(0)|^2}. \tag{6.43}$$

In the scenario where the noise is at the standard quantum limit (i.e., shot noise), S_{δ} is the due to the vacuum fluctuations of the electric field. The quantization of the field gives

$$\hat{S}_{\delta}(t) = \sqrt{\frac{\hbar\omega}{V}}\hat{A}(t), \tag{6.44}$$

where $\hat{S}(t)$ is now an operator and $\hat{A}(t)$ is the photon annihilation operator [138]. The expectation value is

$$\frac{1}{2}\langle\hat{S}_{\delta}^{\dagger}\hat{S}_{\delta} + \hat{S}_{\delta}\hat{S}_{\delta}^{\dagger}\rangle = \frac{\hbar\omega}{2V}, \tag{6.45}$$

since the noise arises from the vacuum, $|0\rangle$, photon state. On the other hand, the classical equivalence is

$$\begin{aligned}\langle S_\delta^2 \rangle &= \lim_{T\to\infty} \frac{2\pi}{T} \int \mathrm{d}\tilde{\omega} |\tilde{S}_\delta(\tilde{\omega})|^2 \\ &\approx \lim_{T\to\infty} \frac{2\pi}{T} |\tilde{S}_\delta(0)|^2 \Delta\tilde{\omega}.\end{aligned} \tag{6.46}$$

Therefore, equating Eq. (6.45) with Eq. (6.46), we have

$$\lim_{T\to\infty} \frac{|\tilde{S}_\delta(0)|^2}{T} = \frac{\hbar\omega}{4\pi V \Delta\tilde{\omega}}. \tag{6.47}$$

Taking $\Delta\tilde{\omega} = 2\kappa_t$, the bandwidth of a CROW band, and $\omega \approx \Omega$, the noise figure is

$$\mathrm{NF} = \frac{\kappa_t R_{sp} \sum_{j=1}^{N} |\mathsf{T}_{N,j}|^2}{\pi^2 \mu^2 |\mathsf{T}_{N,1}|^2}. \tag{6.48}$$

Fig. 6.6 shows an estimate of the noise figure for a loss-compensated CROW where $1/\tau_i = 0$. R_{sp} is given by $R_{sp} = N_2 V_{cav}/t_{sp}$, where N_2 is the population density of the excited state of the gain medium, V_{cav} is the active volume of the resonator, and t_{sp} is the spontaneous emission lifetime. Taking $N_2 = 10^{18}$ cm^{-3}, $V_{cav} = 10$ μm $\times$ 10 μm $\times$ 50 nm, and $t_{sp} = 1$ ns, we compute Eq. (6.48) at the band-center frequency for various values of inter-resonator coupling coefficients at a fixed input/output coupling constant of $\tau_e = 1000$ and $\mu = 0.045$. The noise figure depends strongly on the input/output coupling as well as the inter-resonator coupling. Nonetheless, using these rough estimates, we see that through a suitable choice of coupling coefficients, loss-compensated CROWs of the order of tens of resonators long can maintain noise figures of less than 5.

6.5 Discussion

We have elucidated the effect of the boundary conditions on the net gain in a CROW and the spontaneous emission on the SNR. Our results imply that the trans-

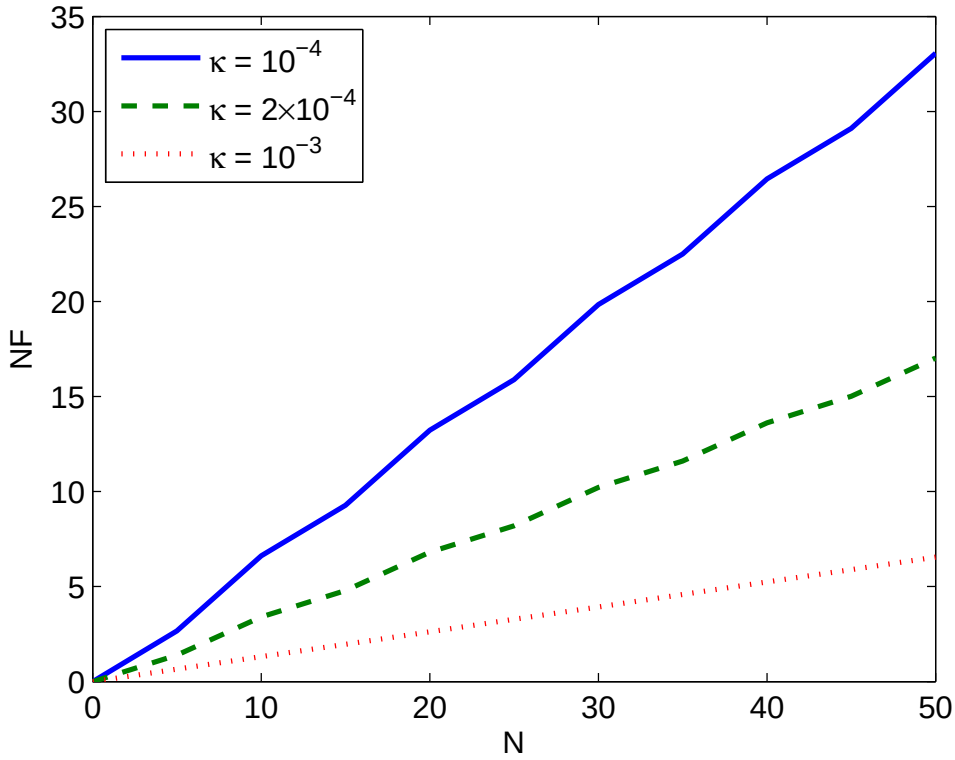

Figure 6.6: The noise figure (NF) as a function of the number of resonators (N) in an active CROW at the band-center frequency where the losses are exactly compensated. The parameters for the calculations are described in the text.

mission spectra, gain/loss, and noise of CROWs depend significantly on the exact configuration of the CROWs and how they are excited. The dispersion relation of an infinite structure, in the presence of gain (or loss), does not necessarily model a periodic structure of finite length regardless of the number of periods that constitute the device. While the real part of the phase accumulated in a finite CROW can be similar to an infinite structure, the imaginary part of the phase (loss/gain) can differ significantly.

Our results show gain (loss) enhancement in CROWs does not strictly depend on v_g, but can instead be understood as the combined effect of the gain (loss) of the individual cavities and the resonance due to the finite length of the structure. Since the effective reflectivity of a semi-infinite CROW is highest at the band-edges [132], the "large" resonator set up in the direction of periodicity consisting of all the cavities in the CROW is lowest loss for the band-edge or low v_g modes. In the same way that transmission spectrum ripples can be minimized by modifying only the input/output coupling coefficients in a CROW [132], the gain (and loss) can also be controlled. The dependence of optical loss on the structural termination has been observed in photonic crystals [139] and the dependence of the laser frequencies and cleaved facets has been analyzed in distributed feedback lasers [140]. The effect of the termination on the optical properties of periodic structures should be explored in greater detail.

Our calculations of active CROWs with an input at the first resonator and output show that the frequencies near the band-center have the highest SNR. Fortuitously, the band-center is also the region of lowest group velocity dispersion, and its dispersive properties are the most robust to disorder in the coupling constants [141, 142]. Naturally then, the most ideal frequencies for the propagation of optical signals with small v_g should be those near the CROW band-center. In contrast, other types of periodic structures, such as gratings and photonic crystals, the small group velocities occur near the band-edges and are accompanied by a large group velocity dispersion. It is also unclear the value of the SNR at those frequencies.

Although we have not formulated a complete picture of amplification in CROWs, which would require additional equations to describe the carrier densities and a quan-

tum mechanical treatment of the transition rates (to derive the gain/loss, noise), we briefly note that the impact of v_g on the induced optical transition rates and the gain. For a simple two-level atom model, the induced transition rate, W_i is proportional to the optical intensity [138] which is higher for reduced group velocities. To show this, we observe that for a monochromatic wave in a homogeneous medium, its intensity is

$$I(\omega) = \frac{cn_{ph}\hbar\omega}{nV}, \tag{6.49}$$

where n_{ph} is then the number of photons in the mode oscillating at ω, V is the modal volume, and n is the effective index of the medium. However,

$$n_{ph} = \rho(\omega)\mathrm{d}\omega = \rho(K)\mathrm{d}K, \tag{6.50}$$

where $\rho(\omega)$ is the photon density of states in frequency and $\rho(K)$ is the density of states in wavenumber. Because $v_g = \mathrm{d}\omega/\mathrm{d}K$ and $\rho(K) = N\Lambda/2\pi$ [142], substituting into Eq. (6.50), we have

$$n_{ph} = \frac{N\Lambda}{2\pi}\frac{\delta\omega}{v_g(\omega)}. \tag{6.51}$$

Thus, a small group velocity leads to a higher stimulated emission rate. However, the optical gain does not strictly depend on W_i. Rather, the optical amplification rate is the fractional increase in the intensity of a wave per unit time, i.e., $\dot{I}/I = \dot{n}_{ph}/n_{ph}$ [138]. Since $\dot{n}_{ph}$ is also proportional W_i, the $1/v_g$ contribution cancels. This implies that although W_i scales with $1/v_g$, the gain does not necessarily. In CROW lasers, the lowest v_g or band-edge modes need not oscillate first or at all.

6.6 Summary

We have presented a derivation of the time domain tight-binding equations describing the modes and wave propagation in CROWs. Only in the limit of weak coupling and weak gain does the tight-binding equation resemble the simple coupled oscillator equations commonly found in literature. Using this formalism, we find that

the termination and excitation of a CROW has a profound impact on the net gain of an optical wave inside the structure. A finite CROW can have significantly different amplification and loss properties compared to an infinitely long chain of resonators. Finally, we have derived the signal-to-noise ratio (SNR) and the noise figure of amplifying CROWs using the tight-binding approach.

Chapter 7

Slowing Light with Fabry-Perot Resonator Arrays

7.1 Introduction

For electrically controllable amplification and coupling, CROWs with suitable metal contacts and thermal dissipation are necessary. To this end, planar structures with a small to moderate refractive index contrast are the simplest to implement. On the other hand, to achieve significant slowing of optical pulses in CROWs, and indeed in any medium, the optical delay should be achieved over as short a device length as possible in the direction of propagation. In many realizations of CROWs, such as coupled Bragg grating defects [53], photonic crystal defect cavities [50], or ring resonators [10, 48, 49], maximizing the slowing factor necessitates using a high refractive index contrast material system to keep the resonators compact and the inter-resonator coupling strength weak.

A high refractive index contrast poses some practical challenges. First, a high index contrast significantly increases scattering loss due to sidewall roughness. Second, more complex fabrication procedures may be required for the devices. For example, small (sub-micron) feature sizes and a large etch depth ($\sim$ microns) or even suspended membranes as in photonic crystal cavities may be needed. Third, the high index contrast leads to a greater mismatch between an optical fiber mode and the mode of the CROW, further increasing the insertion losses of the system.

In this chapter[1], we propose to use an array of evanescently coupled Fabry-Perot resonators as a low index contrast slow light structure. Despite the low index contrast, a high slowing factor is obtained by decoupling the length of the device in the propagation direction from the size of the resonators. Certain implementations of such CROWs are depicted in Fig. 7.1(a) and (b). A large slowing factor is possible because along z, the direction of propagation, the period of the device can be short, say about 5 μm for evanescently coupled single-mode waveguides. This periodicity is similar to what is achievable in high-index contrast photonic crystal, ring, or disk resonators. In the y direction, propagating optical waves are resonant with the cavities. Moreover, optical gain and electronic control can be readily incorporated into the coupled waveguide array by leveraging diode laser array technologies [1, 143]. An optical signal can couple into the first array element in a side-coupled or end-coupled configuration as in Fig. 7.1(c)–(d). The output can then be out-coupled in a similar manner out of the last element of the array. The difference between the side-coupled and end-coupled structures is the presence of reflectors in the first and last waveguides in the end-coupled geometry. The differences in the input and output coupling mechanisms and configurations lead to a qualitative change of the transmission properties.

This chapter presents a transfer matrix method to analyze CROWs in the form of low index contrast coupled waveguide resaontor arrays. We will first show how the conventional coupled mode approach commonly used to analyze waveguide arrays [1] can be extended to the treatment of coupled Fabry-Perot resonators to derive the CROW dispersion relation. We will then show how the transfer matrix formalism can be used to study arrays with side-coupled or end-coupled input and output ports. Finally, we will discuss the dispersion and transmission in the presence of optical gain. Due to the compact length along the propagation direction in evanescently coupled arrays, large slowing factors of the order of 10^2–10^3 can be achieved even with a weak index contrast of $\sim 0.1\%$. The large slowing factor, coupled with weak index contrast, makes this structure a promising candidate for active CROWs.

[1]

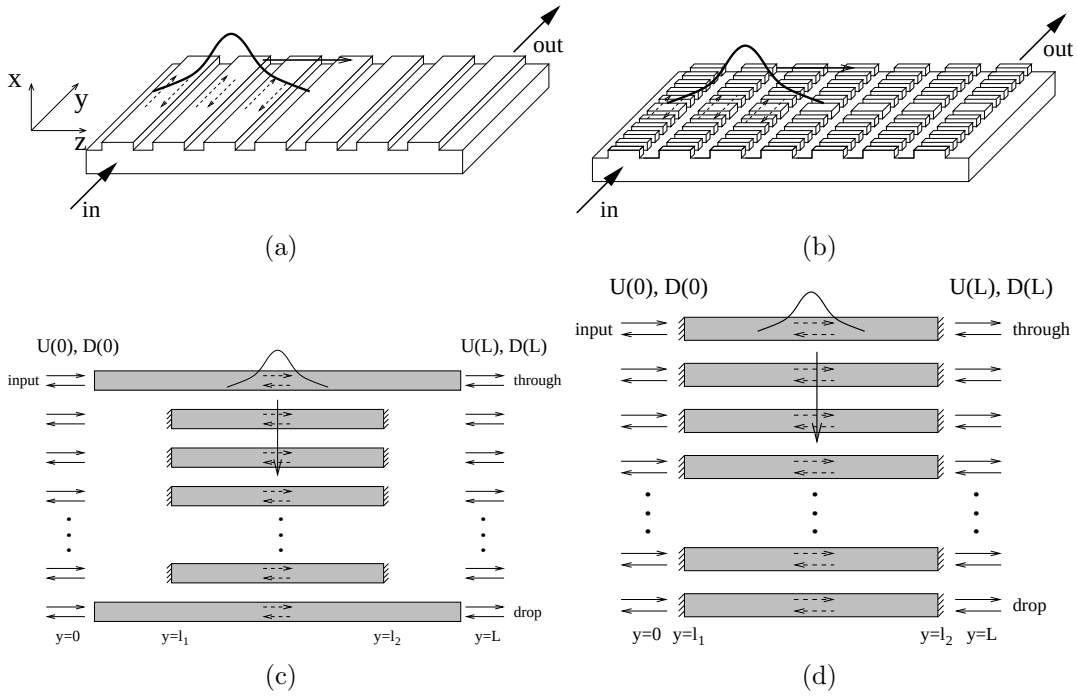

Figure 7.1: Schematic of (a) waveguide laser and (b) DFB laser arrays in a planar geometry as implementations of CROWs. The input/output can be (c) side-coupled or (d) end-coupled into/out of the array. The slanted lines represent reflectors that define each resonator.

7.2 Coupled-Mode Theory

Weakly coupled waveguide arrays are commonly analyzed using spatial coupled-mode theory [1]. In this section, we will briefly review the approach and show how the dispersion relation of a tight-binding form [19] can be recovered from the analysis.

Using the co-ordinate system in Fig. 7.1, for an array of N coupled, identical waveguides, we write the dielectric constant of the structure as

$$\epsilon(\mathbf{r}) = \bar{\epsilon}(\mathbf{r}) + \sum_{n=1}^{N} \Delta\epsilon(\mathbf{r}_\perp - n\Lambda\hat{z}), \tag{7.1}$$

where $\bar{\epsilon}(\mathbf{r})$ is the dielectric constant in the absence of any waveguides, $\mathbf{r}_\perp$ represents the transverse co-ordinates (x, z), $\Delta\epsilon(\mathbf{r}_\perp)$ defines each waveguide, and Λ is the period in the z direction. In coupled-mode theory, we write the total field as a superposition of the modes of the constituent waveguides,

$$\mathcal{E}(\mathbf{r}) = \sum_{n=1}^{N} c_n(y)\mathcal{E}_n(x, z)\exp(-i\beta_0 y), \tag{7.2}$$

where $\mathcal{E}(\mathbf{r})$ is electric field in the array, $c_n(y)$ are coefficients of expansion, $\mathcal{E}_n(x, z)$ and $\beta_0 = \omega n_{\text{eff}}(\omega)/c$ are the mode profile and propagation constant of the nth waveguide in the uncoupled case respectively.

Expressing the y-dependent part of the total field as a column vector, we write

$$\mathbf{E}(y) \equiv \begin{bmatrix} c_1(y)e^{-i\beta_0 y} \\ c_2(y)e^{-i\beta_0 y} \\ \cdot \\ \cdot \\ \cdot \\ c_N(y)e^{-i\beta_0 y} \end{bmatrix} \equiv \begin{bmatrix} E_1(y) \\ E_2(y) \\ \cdot \\ \cdot \\ \cdot \\ E_N(y) \end{bmatrix}. \tag{7.3}$$

Neglecting interaction between non neighboring waveguides, the coupled-mode

equations can thus be written in matrix form as

$$\frac{d\mathbf{E}}{dy} = \mathbf{C}\mathbf{E}, \quad \text{where} \quad \mathbf{C} = -i \begin{bmatrix} \beta_0 + M_l & \kappa_l & 0 & 0 & ... & 0 & 0 \\ \kappa_l & \beta_0 + M_l & \kappa_l & 0 & ... & 0 & 0 \\ . & . & . & . & . & . & . \\ . & . & . & . & . & . & . \\ . & . & . & . & . & \kappa_l & \beta_0 + M_l \end{bmatrix}. \quad (7.4)$$

Here κ_l is the per-length nearest neighbor coupling coefficient and M_l is the per-length self-coupling coefficient given by

$$\kappa_l = \frac{\omega\epsilon_0}{4} \int_{-\infty}^{\infty} \mathcal{E}_n^*(\mathbf{r}_\perp) \left[\epsilon(\mathbf{r}_\perp) - \Delta\epsilon(\mathbf{r} - n\Lambda)\right] \mathcal{E}_{n+1}(\mathbf{r}_\perp) d\mathbf{r}_\perp \quad (7.5a)$$

$$M_l = \frac{\omega\epsilon_0}{4} \int_{-\infty}^{\infty} \mathcal{E}_n^*(\mathbf{r}_\perp) \left[\epsilon(\mathbf{r}_\perp) - \Delta\epsilon(\mathbf{r} - n\Lambda)\right] \mathcal{E}_n(\mathbf{r}_\perp) d\mathbf{r}_\perp, \quad (7.5b)$$

where we have used the normalization

$$\frac{\beta_0}{2\omega\mu} \int_{-\infty}^{\infty} \mathcal{E}_m^*(\mathbf{r}_\perp) \mathcal{E}_n^*(\mathbf{r}_\perp) d\mathbf{r}_\perp = \delta_{m,n}. \quad (7.6)$$

The propagation constants of the array modes, β, are determined by the solution of the eigenvalue equation

$$(\mathbf{C} + i\beta\mathbf{I})\mathbf{E} = 0, \quad (7.7)$$

where $\mathbf{I}$ is the $N \times N$ unit matrix, and ω represents the frequency of interest.

Implicit in Eq. (7.4) is the boundary condition $c_0 = c_{N+1} = 0$ (which corresponds to no field propagating in the two end waveguides). Furthermore, we assume the s^{th} mode of the waveguide array takes the form $\mathcal{E}^{(s)}(\mathbf{r}) = \sum_{n=1}^{N} a_n^{(s)} \mathcal{E}_n(x, z) \exp(-i\beta^{(s)} y)$. The associated eigenmodes and propagation constants are given by

$$\beta^{(s)} = \beta_0 + M_l + 2\kappa_l \cos\left(\frac{s\pi}{N+1}\right) \quad (7.8a)$$

$$a_n^{(s)} = \sin\left(\frac{ns\pi}{N+1}\right), \quad (7.8b)$$

where $s = 1...N$ and $n = 1...N$ are integers and n enumerates positions of the waveguides.

Thus far, the coupled-mode theory we have used is in the spatial domain where we have solved for the N propagation constants of the waveguide array supermodes, $\beta^{(s)}$, at a fixed (given) frequency embodied by $\beta_0 = \omega n_{\text{eff}}(\omega)/c$. If we introduce reflection at the end of each waveguide in an array of resonators, the feedback along the y direction discretizes $\beta^{(s)}$ such that the modes of the resonator arrays satisfy $\beta^{(s)}L = m\pi$, where L is the length of the array length in y and m is an integer. Hence, to find the dispersion relationship of a resonator array, we use Eq. (7.8a) to determine the frequencies (or values of β_0) for which $\beta^{(s)}L = m\pi$.

Fig. 7.2 clarifies the effects of imposing an additional set of boundary conditions in y to the coupled-mode treatment of an array of waveguides. For the calculations, we have assumed 8 coupled resonators/waveguides with a coupling constant of 8×10^{-4} μm^{-1}. Without the feedback in the y direction, we compute $N = 8$ values of $\beta^{(s)}$ at each frequency, thus arriving at the linear dispersion relations (the sloped lines) shown on the left half of the figure. The condition $\beta^{(s)}L = m\pi$ ($L = 500\mu\text{m}$ and $m = 2097$), denoted by the vertical line in the plot, "selects" the resonance frequencies of the resonator array, which are marked by "×"s. These resonance frequencies in turn correspond to particular values of $s\pi/(N+1)$ shown on the right side of Fig. 7.2. Through this process, the waveguide dispersions from the time-independent coupled-mode theory are converted to the dispersion relation of the coupled resonators.

Assuming that Ω is the resonance frequency of an uncoupled resonator, such that $\beta_0(\Omega)L = \Omega n_{\text{eff}}(\Omega)L/c = m\pi$, setting $\beta^{(s)}L = m\pi$ gives

$$\omega^{(s)} = \Omega \frac{n_{\text{eff}}(\Omega)}{n_{\text{eff}}(\omega^{(s)})} \left[1 - \frac{M_l L}{m\pi} - 2\frac{\kappa_l L}{m\pi} \cos\left(\frac{s\pi}{N+1}\right)\right]. \tag{7.9}$$

As expected, for N coupled cavities, there are N discrete resonant frequencies.

As $N \to \infty$, the array modes described by Eq. (7.9) form a continuum and the array eigenmodes of the structure can be treated as the Bloch modes of the system. A Bloch mode is a periodic function in which the field in the $(n+1)^{th}$ period differs

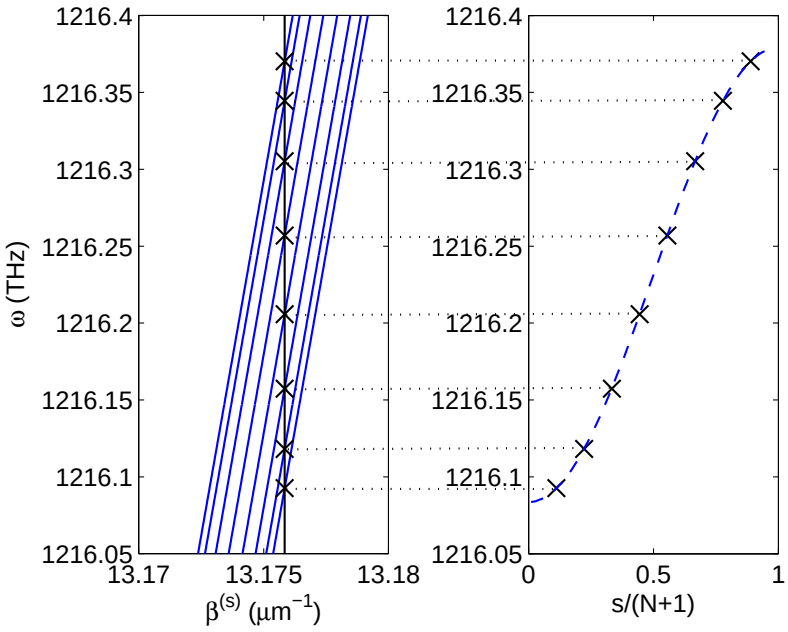

Figure 7.2: A schematic illustrating the role of the additional resonance or boundary condition in y. On the left, The resonance condition $\beta^{(s)}L = m\pi$ selects the resonance frequencies from the dispersion relations of the waveguide array. These frequencies correspond to particular values of $s\pi/(N+1)$ on the right.

from the n^{th} period by a phase factor of $K\Lambda$, where K is the (continuous) Bloch wave number and Λ is the period. Because the fields described by Eq. (7.8b) are standing waves along z, they can be decomposed into superposition of counter-propagating traveling waves along $\hat{z}$. Therefore, by comparison with Eq. (7.8b), we can replace

$$\lim_{N\to\infty} s\pi/(N+1) \to K\Lambda. \tag{7.10}$$

This leads to the dispersion of a CROW based on an array of coupled Fabry-Perot resonators

$$\omega(K) = \Omega\left[1 - \frac{M}{m\pi} - 2\frac{\kappa}{m\pi}\cos\left(K\Lambda\right)\right], \tag{7.11}$$

where we have assumed $n_{\text{eff}}(\omega) = n_{\text{eff}}(\Omega) = n$ is a constant, and $\kappa_l L = \kappa$ and $M_l L = M$ are dimensionless coupling coefficients. The frequency dependence of κ and M are given by Eq. (7.5); however, since the bandwidth of a CROW is not expected to be large ($\omega/\Omega \ll 1$), the coupling coefficients can be assumed to be

constant.

The dispersion relation described by Eq. (7.11) is of the same form as the CROW dispersion from the tight-binding approximation and the dispersion calculated using transfer matrices for ring resonators in Chapter 2. The key difference between Fabry-Perot and ring resonators is that only two K vectors correspond to a particular eigen-frequency for the Fabry-Perot resonators while there are four K vectors for the rings. Physically, this is because a ring resonator supports two degenerate modes on resonance (i.e., even and odd, or clockwise and counter-clockwise), while a Fabry-Perot resonator supports one mode on resonance.

The slowing factor, given by the ratio of the speed of light to the maximum group velocity in the CROW, is

$$S = \frac{c}{v_{g_{|\max}}} = \frac{nL}{2\kappa\Lambda} = \frac{n}{2\kappa_l\Lambda}. \tag{7.12}$$

Unlike coupled grating defects or ring resonators, the period Λ of the CROW is decoupled from L. Since for weakly coupled single-mode waveguides $\kappa_l \approx 10^{-4} - 10^{-3}$ μm^{-1} and Λ can be ~ 5 μm even for modest index contrast ($\Delta n/n \approx 10^{-3}$–$10^{-2}$), large slowing factors of the order of a few hundred to a thousand are possible.

7.3 Transfer Matrix Analysis

While the modes and the dispersion relation of a waveguide array CROW can be determined from the coupled-mode theory of a waveguide array, the transmission spectrum does not immediately follow from the calculations. One approach to calculate the spectrum is to expand the input excitation field in terms of the eigenmodes of the CROW and propagate the modes individually. A second, more convenient approach, which we shall describe in this section, is to use a transfer matrix formalism. This method can account for an arbitrary input excitation at the array end-facet, applies to asymmetric structures, and can also be used for arrays with side-coupled input/output waveguides.

To use the transfer matrix formalism, we describe the propagation of light through the structure with a $2N \times 2N$ matrix. The matrix acts on a column vector describing both the forward and backward propagating fields at each waveguide as shown in Fig. 7.1(c)–(d). We denote the fields at each interface by

$$\mathbf{U}(y) = [E_1^{(+)}(y) \quad E_2^{(+)}(y) \dots E_N^{(+)}(y)]^T, \quad \mathbf{D}(y) = [E_1^{(-)}(y) \quad E_2^{(-)}(y) \dots E_N^{(-)}(y)]^T, \tag{7.13}$$

where $E_n^{(+)}(y)$ and $E_n^{(-)}(y)$ are the forward and backward propagating fields respectively in each element at a particular value of y. Thus, the fields at $y = L$ are related to those at $y = 0$ by

$$\begin{bmatrix} \mathbf{U}(L) \\ \mathbf{D}(L) \end{bmatrix} = \mathbf{S}^{(2)} \mathbb{Q} \mathbf{S}^{(1)} \begin{bmatrix} \mathbf{U}(0) \\ \mathbf{D}(0) \end{bmatrix}. \tag{7.14}$$

Here $\mathbf{S}^{(1,2)}$ are matrices describing the reflectors at $y = l_1$ and $y = l_2$, which can arise from Fresnel or Bragg reflection. $\mathbb{Q}$ is the transfer matrix that describes the coupling and propagation in the array region.

To simplify the numerics and make the system more tractable, we assume that light is not coupled from one element to the next in the reflector sections (from $y = 0$ to $y = l_1$ and from $y = l_2$ to $y = L$). This assumption is valid for reflection from cleaved facets and for well-confined waveguide modes in short gratings. For the inter-cavity coupling (from $y = l_1$ to $y = l_2$), we are primarily interested in the weak coupling regime, where only nearest-neighbor coupling is significant. The inclusion of the more general effect (e.g., nearest neighbor coupling in the grating sections) will lead to quantitative, but not qualitative changes in our results.

The form of $\mathbf{S}^{(q)}$ (where $q = 1, 2$) is given by

$$\mathbf{S}^{(q)} = \left[\begin{array}{c|c} \mathbf{S}_{11}^{(q)} & \mathbf{S}_{12}^{(q)} \\ \hline \mathbf{S}_{21}^{(q)} & \mathbf{S}_{22}^{(q)} \end{array}\right] = \left[\begin{array}{cccc|cccc} \mathsf{P}_{11}^{(q)} & & & & \mathsf{P}_{12}^{(q)} & & & \\ & \mathsf{F}_{11}^{(q)} & & & & \mathsf{F}_{12}^{(q)} & & \\ & & \ddots & & & & \ddots & \\ & & & \mathsf{F}_{11}^{(q)} & & & & \mathsf{F}_{12}^{(q)} \\ & & & & \mathsf{P}_{11}^{(q)} & & & \mathsf{P}_{12}^{(q)} \\ \hline \mathsf{P}_{21}^{(q)} & & & & \mathsf{P}_{22}^{(q)} & & & \\ & \mathsf{F}_{21}^{(q)} & & & & \mathsf{F}_{22}^{(q)} & & \\ & & \ddots & & & & \ddots & \\ & & & \mathsf{F}_{21}^{(q)} & & & & \mathsf{F}_{22}^{(q)} \\ & & & & \mathsf{P}_{21}^{(q)} & & & \mathsf{P}_{22}^{(q)} \end{array}\right], \tag{7.15}$$

where $\mathbf{S}_{ij}^{(q)}$ are $N \times N$ diagonal sub-matrices, and $\mathsf{F}_{ij}^{(q)}$ are derived from the 2×2 transfer matrices for the reflectors. In other words, for the middle waveguides (where $n \neq 1, N$) we have

$$\begin{bmatrix} E_n^{(+)}(l_1) \\ E_n^{(-)}(l_1) \end{bmatrix} = \begin{bmatrix} \mathsf{F}_{11}^{(1)} & \mathsf{F}_{12}^{(1)} \\ \mathsf{F}_{21}^{(1)} & \mathsf{F}_{22}^{(1)} \end{bmatrix} \begin{bmatrix} E_n^{(+)}(0) \\ E_n^{(-)}(0) \end{bmatrix}, \tag{7.16}$$

$$\begin{bmatrix} E_n^{(+)}(L) \\ E_n^{(-)}(L) \end{bmatrix} = \begin{bmatrix} \mathsf{F}_{11}^{(2)} & \mathsf{F}_{12}^{(2)} \\ \mathsf{F}_{21}^{(2)} & \mathsf{F}_{22}^{(2)} \end{bmatrix} \begin{bmatrix} E_n^{(+)}(l_2) \\ E_n^{(-)}(l_2) \end{bmatrix}. \tag{7.17}$$

For an array of $N - 2$ resonators with side-coupled waveguides for input and output coupling, $\mathsf{P}_{12}^{(q)} = \mathsf{P}_{21}^{(q)} = 0$ and $\mathsf{P}_{11}^{(q)} = (\mathsf{P}_{22}^{(q)})^{-1}$ describes the accumulation of phase. This lead to $\mathsf{P}_{11}^{(1)} = \exp(-i\beta_0 l_1)$ and $\mathsf{P}_{11}^{(2)} = \exp(-i\beta_0(L - l_2))$. Otherwise, for input coupling at the end-facet of an array of N resonators, $\mathsf{P}_{ij}^{(q)} = \mathsf{F}_{ij}^{(q)}$. The elements $\mathsf{F}_{ij}^{(q)}$ can be readily calculated for an arbitrary type of mirror (e.g., Bragg reflectors, cleaved facets).

In the waveguide/coupler section of the structure in Fig. 7.1(c)–(d), one can use

the coupled mode theory described in the previous section:

$$\frac{d}{dy}\begin{bmatrix}\mathbf{U}(y)\\ \mathbf{D}(y)\end{bmatrix} = \begin{bmatrix}\mathbf{C} & \emptyset\\ \emptyset & \mathbf{C}^{\dagger}\end{bmatrix}\begin{bmatrix}\mathbf{U}(y)\\ \mathbf{D}(y)\end{bmatrix}. \tag{7.18}$$

Therefore,

$$\begin{bmatrix}\mathbf{U}(l_2)\\ \mathbf{D}(l_2)\end{bmatrix} = \begin{bmatrix}\mathbf{Q} & \emptyset\\ \emptyset & \mathbf{Q}^{\dagger}\end{bmatrix}\begin{bmatrix}\mathbf{U}(l_1)\\ \mathbf{D}(l_1)\end{bmatrix} \equiv \mathbb{Q}\begin{bmatrix}\mathbf{U}(l_1)\\ \mathbf{D}(l_1)\end{bmatrix}, \tag{7.19a}$$

$$\mathbf{Q} = \exp\left(\mathbf{C}L\right). \tag{7.19b}$$

Combining Eqs. (7.15) and (7.19), the transfer matrix for the overall system is given by

$$\begin{bmatrix}\mathbf{U}(L)\\ \mathbf{D}(L)\end{bmatrix} = \begin{bmatrix}\mathbf{S}_{11}^{(2)} & \mathbf{S}_{12}^{(2)}\\ \mathbf{S}_{21}^{(2)} & \mathbf{S}_{22}^{(2)}\end{bmatrix}\begin{bmatrix}\mathbf{Q} & \emptyset\\ \emptyset & \mathbf{Q}^{\dagger}\end{bmatrix}\begin{bmatrix}\mathbf{S}_{11}^{(1)} & \mathbf{S}_{12}^{(1)}\\ \mathbf{S}_{21}^{(1)} & \mathbf{S}_{22}^{(1)}\end{bmatrix}\begin{bmatrix}\mathbf{U}(0)\\ \mathbf{D}(0)\end{bmatrix} \equiv \begin{bmatrix}\mathbf{G}_{11} & \mathbf{G}_{12}\\ \mathbf{G}_{21} & \mathbf{G}_{22}\end{bmatrix}\begin{bmatrix}\mathbf{U}(0)\\ \mathbf{D}(0)\end{bmatrix}, \tag{7.20}$$

where $\mathbf{G} \equiv \mathbf{S}^{(2)}\mathbb{Q}\mathbf{S}^{(1)}$.

Rearranging terms in Eq. (7.20) and assuming $\mathbf{D}(L) = 0$ (no field is incident from the right), we have

$$\mathbf{U}(L) = \left(\mathbf{G}_{11} - \mathbf{G}_{12}\mathbf{G}_{22}^{-1}\mathbf{G}_{21}\right)\mathbf{U}(0) \tag{7.21a}$$

$$\mathbf{D}(0) = \left(-\mathbf{G}_{22}^{-1}\mathbf{G}_{21}\right)\mathbf{U}(0), \tag{7.21b}$$

which relates the input and output fields of our structure.

The transfer matrices can account for an arbitrary input field at $y = 0$ and can be used to calculate the reflection and transmission coefficients of any resonator. However, in most cases, we are primarily interested in exciting the first element and the transmission and reflection coefficients in the first and last elements only. In this case, the boundary conditions are $\mathbf{U}^T(0) = \begin{bmatrix}1 & 0 & 0 & 0 & ... & 0\end{bmatrix}$ and $\mathbf{D}^T(L) = \begin{bmatrix}0 & 0 & 0 & 0 & ... & 0\end{bmatrix}$. Using Eq. (7.21) and the boundary conditions, the transmission

and reflection coefficients are

$$R_1 = \frac{D_1(0)}{U_1(0)} \qquad R_N = \frac{D_N(0)}{U_1(0)} \tag{7.22}$$

$$T_1 = \frac{U_1(L)}{U_1(0)} \qquad T_N = \frac{U_N(L)}{U_1(0)} \tag{7.23}$$

with $U_n(y)$ representing the n^{th} element of $\mathbf{U}(y)$, and R_1 and T_1 are the reflection and transmission coefficients at the input/through port as marked in Fig. 7.1, while R_2 and T_2 are the coefficients at the drop/output port.

The transmission and reflection spectra for a CROW with 5 resonators with side-coupled input and output waveguides are shown in Fig. 7.3. The reflectors in the calculations consist of Bragg gratings with alternating layers of thicknesses $d_H = 119$ nm and $d_L = 123$ nm, with effective indices $n_H = 3.25$ and $n_L = 3.15$ respectively. The gratings are 24 μm or 100 periods long. The waveguide sections have an effective index of 3.25 and are 50 μm long. The coupling constant is $\kappa_l = 4 \times 10^{-3}$ μm^{-1}. These parameters can be accomplished by 1.25 μm wide waveguides with an effective index of 3.25, spaced about 900 nm apart, surrounded by a cladding of index 3.15. The resultant length of the coupled resonators in the direction of periodicity is about 10 μm.

By design, the standing wave cavities supports a resonance mode at a free-space wavelength of 1.551 μm. It is apparent that the transmission properties of our structures resemble that of microring CROWs. In close vicinity of the resonance frequency Ω, the transmission across cavities is increased. In contrast to CROWs consisting of traveling wave cavities (e.g., ring/disk resonators), the maximum transmission in the present situation is 25% rather than unity as in the case of ring resonators. This is attributed to the lack of degenerate modes at Ω in a standing-wave cavity, so the fields in the cavity can decay into the two waveguides in both the forward and backward directions [144, 145]. This poses a limitation on a passive system, but will not be a main concern for systems with optical gain. In passive systems, the maximum transmission shown in Fig. 7.3(b) can be improved by increasing the reflectivity of the Bragg gratings through increasing the number of periods and/or the index con-

trast. The ripples in the spectrum can be reduced by apodizing the coupling constants [11, 132, 146] .

7.4 Optical Gain

The most straight-forward implementation of the Fabry-Perot CROWs is an array of waveguides with cleaved facets providing the feedback for the resonators. Since the Fresnel reflection coefficient is only $\sim 30\%$, a large optical gain is necessary to compensate for the losses. Gain introduces an imaginary component to the coupling constants, κ_l and M_l, and can be used to tune the CROW dispersion if the gain-loss modulation is strong [147].

Optical amplification (and loss) can be built into the coupled-mode theory by writing the dielectric constant as a complex function:

$$\epsilon(\mathbf{r}) = \bar{\epsilon}(\mathbf{r}) + \sum_{n=1}^{N} \left[\Delta\epsilon(\mathbf{r} - n\Lambda) + i\frac{2\epsilon_{\text{eff}}}{\beta_0}\Delta\gamma(\mathbf{r} - n\Lambda) \right], \tag{7.24}$$

where $\Delta\gamma$ denotes the gain coefficient in the waveguides, and ϵ_{eff} normalizes γ/β_0 to $\epsilon(\mathbf{r})$ and is the effective dielectric constant of the waveguides. The gain is a periodic function in z in practice because the gain in the waveguide core and cladding areas will not be identical.

We assume the uncoupled modes of the individual waveguides are $\mathcal{E}_n(x,z)\exp(-i\beta_0 y)$. Using the normalization condition Eq. (7.6), the coupling constants in the presence of gain are

$$\tilde{\kappa}_l = \kappa_l + i\frac{\omega\epsilon_0\epsilon_{\text{eff}}}{2\beta_0}\sum_{j=1}^{N}\int_{-\infty}^{\infty}\mathcal{E}_n^*(\mathbf{r}_\perp)\Delta\gamma(\mathbf{r} - j\Lambda)\mathcal{E}_{n+1}(\mathbf{r}_\perp)d\mathbf{r}_\perp \equiv \kappa_l + i\kappa_l' \tag{7.25a}$$

$$\tilde{M}_l = M_l + i\frac{\omega\epsilon_0\epsilon_{\text{eff}}}{2\beta_0}\sum_{j=1}^{N}\int_{-\infty}^{\infty}\mathcal{E}_n^*(\mathbf{r}_\perp)\Delta\gamma(\mathbf{r} - j\Lambda)\mathcal{E}_{n}(\mathbf{r}_\perp)d\mathbf{r}_\perp \equiv M_l + iM_l', \tag{7.25b}$$

where κ_l and M_l are the coupling constants in the passive structure and are given in

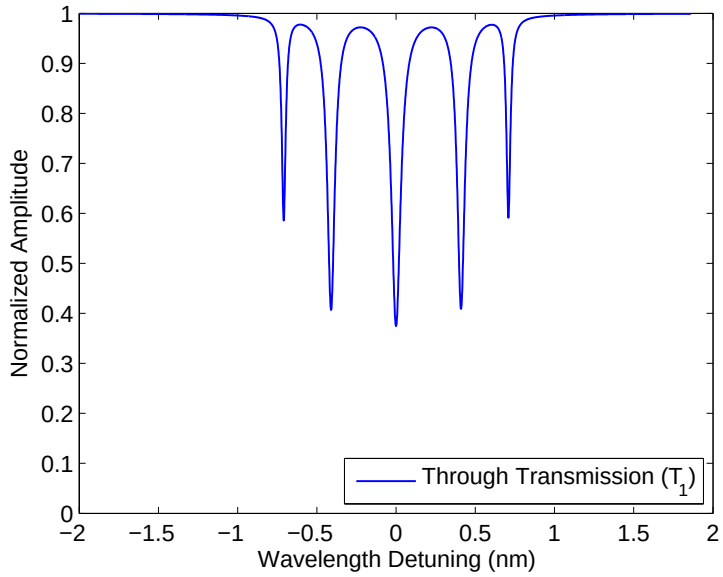

(a)

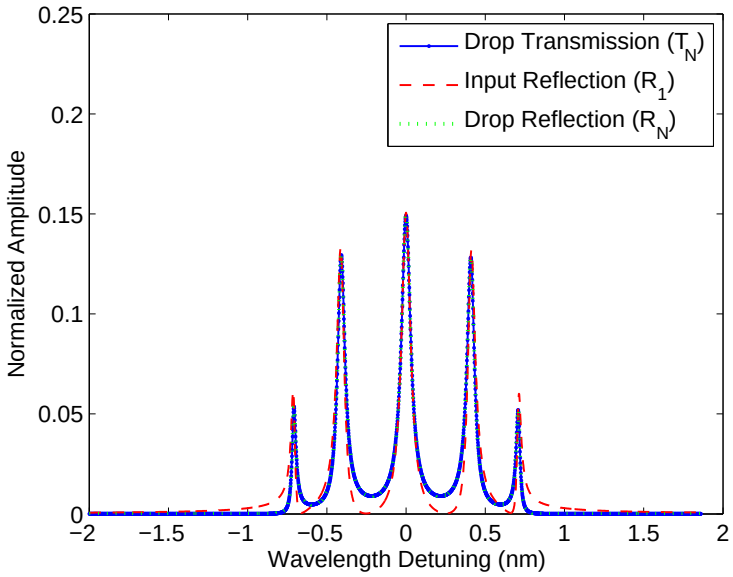

(b)

Figure 7.3: (a) The transmission spectrum at the through port and (b) the transmission and reflection spectra at the input and drop ports for the side-coupled array. The calculation parameters are described in the text.

Eq. (7.5).

The coupling coefficients are now complex. In typical semiconductor materials, $\Delta\gamma$ is of the order of $10^{-3} - 10^{-2}$ μm^{-1}, while β_0 is of the order of 10 μm^{-1}. On the other hand, even in low index contrast systems, $\Delta\epsilon$ is on the order of 10^{-1} ($\Delta n \sim 0.01$). Therefore, in most cases, $\kappa_l'/\kappa_l, M_l'/M_l \ll 1$.

If the Bloch vectors are complex (i.e., to account for net gain/loss in the direction of propagation), $K = K_R + iK_I$, then the dispersion relation for the CROW is

$$\omega(K) = \Omega\left[1 - \frac{M}{m\pi} - 2\frac{\kappa}{m\pi}\cos\left(K_R\Lambda\right)\cosh(K_I\Lambda) - 2\frac{\kappa'}{m\pi}\sin\left(K_R\Lambda\right)\sinh(K_I\Lambda)\right]. \tag{7.26}$$

K_I can be determined from the net gain of the supermodes of the waveguide array:

$$\gamma(K) = M_l' + 2\kappa_l'\cos(K_R\Lambda)\cosh(K_I\Lambda) - 2\kappa_l\sin(K_R\Lambda)\sinh(K_I\Lambda). \tag{7.27}$$

Approximating the gain of the supermodes is roughly equal to the gain of the individual waveguides, $\gamma(K) \approx M_l'$, $K_I\Lambda$ is given by

$$\coth(K_I\Lambda) = \frac{\kappa_l}{\kappa_l'}\tan(K_R\Lambda), \tag{7.28}$$

where $K_I\Lambda = 0$ when $K_R\Lambda = 0, \pi/2, \pi$.

Near the band center, which is the frequency range of interest as the CROW group velocity dispersion is minimum, $K_I\Lambda$ is of the order of 10^{-3} and is negligibly small. Hence, the dispersion relation does not change significantly with gain. However, in real systems, the refractive index is expected to change with the gain through thermal and carrier injection effects. If these effects induce a large gain-loss modulation in the CROW, then the dispersion relation can be significantly modified with the optical gain [147].

In the approximation that the coupling constant remains constant with gain, the gain can be modelled in the transfer matrices by the inclusion of a complex propagation constant $\beta_0 + i\gamma_0$. Fig. 7.4 shows the transmission and phase responses for various values of gain calculated using the transfer matrices by adding an imaginary

component to the propagation constant for an array of 15 stripes. The input is end-coupled into first element of the array as in Fig. 7.1(d). The length of the waveguides is 500 μm, and the coupling constant is $8 \times 10^{-4}/\mu$m. The gain values correspond to 85%, 90%, 95%, and 99.8% of the mirror losses $1/(2L)\ln(r^2)$, where $r^2 = 0.28$ is about the reflectivity of cleaved facets. The coupling strength can be achieved with 3 μm wide waveguides separated by about 1 μm with an index contrast of $\Delta n/n \sim 0.05$, resulting in slowing factors of about 600.

7.5 Summary

We have presented a means of slowing light with low index contrast CROWs using coupled waveguide and laser resonator arrays. Low index contrast systems have the advantage of having smaller side-wall scattering losses for a given roughness and typically requiring simpler fabrication processes (e.g., larger feature sizes, shallower etch depth). We have analyzed evanescently coupled arrays and shown that they can achieve slowing factors of several hundred times with bandwidths of tens of GHz. Optical amplification, naturally present in laser arrays, overcomes the severe limitation of high optical attenuation characteristic of most passive slow light structures. Combining evanescent coupling in the propagation direction with Bragg or Fresnel reflection in the orthogonal direction provides an approach for engineering more complex periodic structures to slow light.

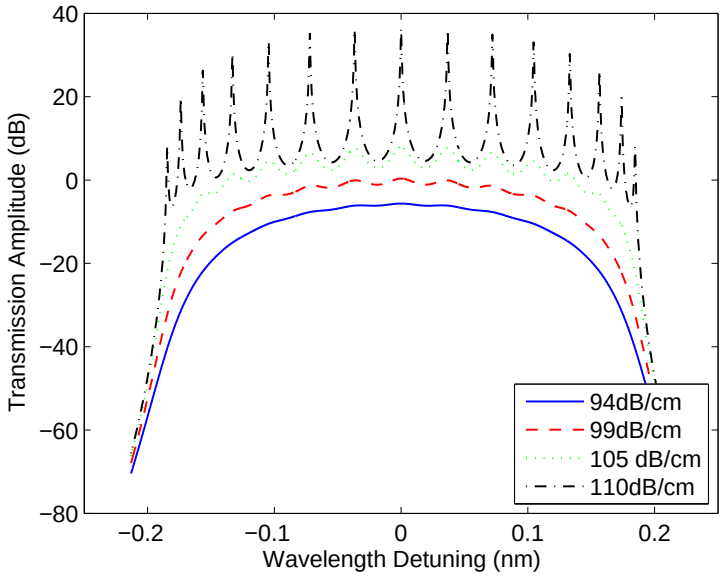

(a)

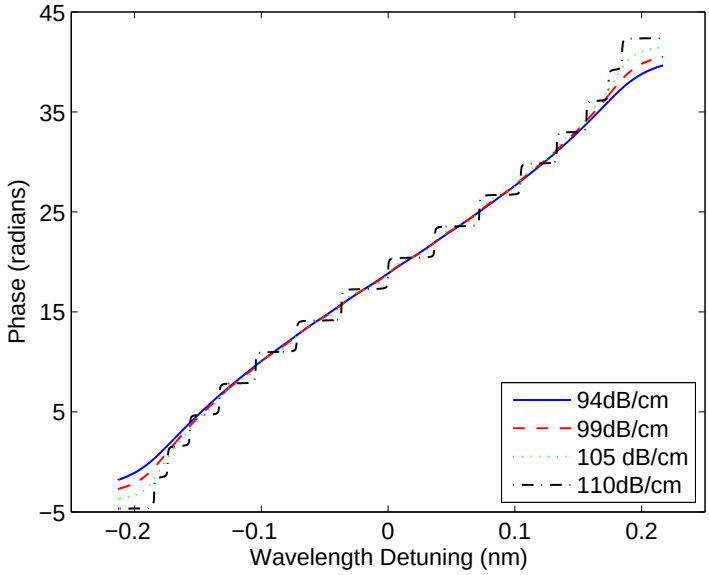

(b)

Figure 7.4: The (a) transmission and (b) phase responses of a resonator array for various gain values. The input is end-coupled into the first element of the array.

Chapter 8

Current Injection InP-InGaAsP Fabry-Perot Resonator Arrays

8.1 Introduction

In this final chapter[1], we present measurements of the transmission spectra of CROWs in the form of active Fabry-Perot resonator arrays fabricated in InP-InGaAsP semiconductor materials. The gain is supplied through the injection of electrical current. The transfer matrix model used to analyze these structures was developed in Chapter 7. The measured signal-to-noise ratio is found to be a strong function of wavelength and degraded rapidly along the resonator chain away from the input. Our results highlight a number of issues related to noise as well as device termination and excitation described in Chapter 6. We shall close by describing the ingredients necessary for the practical implementations of loss-compensated and amplifying CROWs.

8.2 Device Fabrication

For practical purposes, the properties of CROWs, such as the inter-resonator coupling and optical amplification, should be electrically tunable. To this end, we fabricated CROWs in compound III-V semiconductor (InP-InGaAsP) materials. A schematic of the devices is shown in Fig. 8.1. Each CROW consisted of 46 laterally

[1] ©2007 OSA. Reprinted, with permission, from [148].

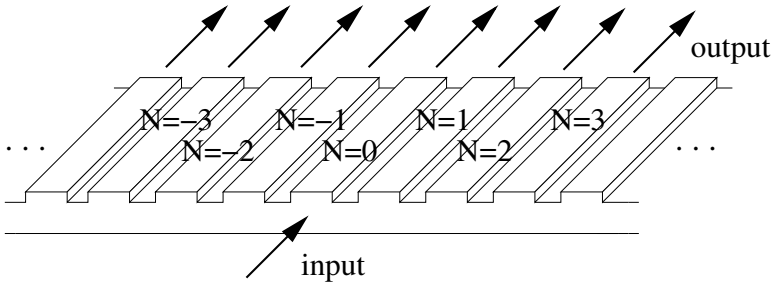

Figure 8.1: Schematic of the Fabry-Perot resonator array CROW

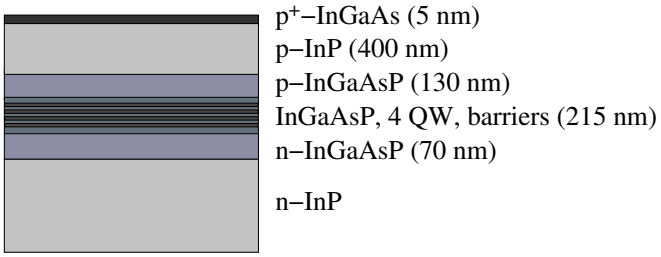

Figure 8.2: Schematic of the wafer structure

coupled Fabry-Perot resonators with a relatively weak index contrast of $\Delta n/n \approx 10^{-2}$ centered under a 100 μm wide electrical contact such that 25 resonators were pumped. The resonators consisted of single-mode waveguides that were 3 μm wide, and we made devices with various inter-resonator spacings near 1 μm. The resonator end mirrors were simply cleaved facets.

The devices were fabricated using a series of aligned electron-beam lithography steps using a Leica EBPG 5000 system, wet chemical etching, and metal evaporation. The wafer structure is outlined in Fig. 8.2 with the active region consisting of four unstrained quantum wells. The wet-etch was a two step process wherein we first transferred the pattern to the thin InGaAs layer using a hydrobromic acid (HBr) etch, and then using the InGaAs as a mask to etch the InP with hydrochloric acid (HCl). The InGaAsP acted as an etch stop for the HCl. The waveguides were aligned along the [110] direction in the InP to obtain straight side-walls. Feature sizes of the order of 100 nm can be chemically etched using this technique [149, 150]. We shall briefly discuss the fabrication process, which is summarized in Fig. 8.3.

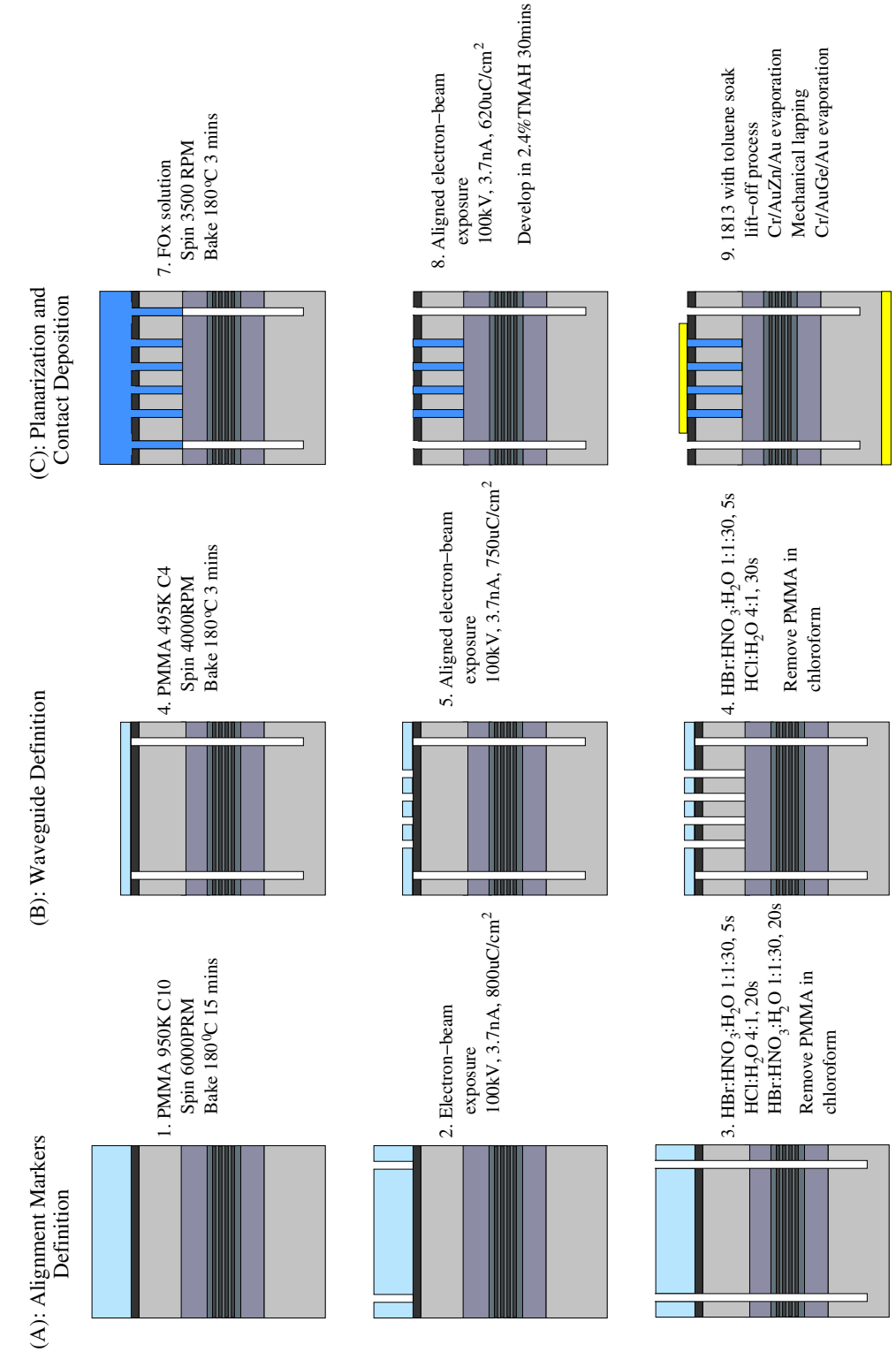

Figure 8.3: Summary of the fabrication process

First, alignment markers were defined using electron-beam lithography in a 2.5 μm thick layer of poly-methylmethacrylate (PMMA) (950K C10, Microchem) and wet-etched into the semiconductor. We immersed the chip in a solution of HBr (48%):HNO_3 (68%):H_2O 1:1:30 for 5 seconds, HCl (37%):H_2O 4:1 for 30 seconds, and HBr:HNO_3:H_2O 1:1:30 for 45 seconds to etch into the InGaAsP layers. The resultant markers were approximately 12 μm $\times$ 12 μm and 1 μm deep. The markers were spaced on a grid of 1.85 mm $\times$ 2.5 mm. The PMMA was stripped off using chloroform after the etching.

Subsequently, a 250 nm thick layer of PMMA (495K C4, Microchem) was spun onto the chip and an electron-beam exposure aligned to the markers was performed to define the trenches between the resonator waveguides. After the lithography, the gaps were etched by immersing the chip in HBr:HNO_3:H_2O 1:1:30 for 5 seconds and HCl:H_2O 4:1 for 30 seconds.

After removing the residual PMMA, a dilution of methylbutylisoketone (MIBK): Flowable Oxide 16 (FOx 16, Dow Corning) 1:1.75 was spun onto the chip. The FOx layer filled the trenches and was about 350 nm thick over the unpatterned regions. FOx is a spin-on glass but can also be cured by electron-beam exposure [151]. A second aligned electron-beam exposure of the trenches was then performed. The chip was developed in 2.4% tetramethylammonium hydroxide (TMAH) solution (CD26, Microposit) for 30 minutes. The FOx patterns were wider than the trenches by 200 nm and backfilled the trenches. Without this planarization step, the devices failed to achieve laser action.

Next, electrical contacts were deposited using a lift-off process. A 2.5 μm thick layer of 1813 resist (Microposit) was spun on and exposed photolithographically. Before development in 2.4% TMAH, the chip was soaked in toluene for 1 minute to create a slight undercut profile to assist the lift-off [152]. The p-side contact, Cr/AuZn/Au 2 nm/6 nm/250 nm, was deposited using a thermal evaporator. The chip was then mechanically thinned to about 100 μm thick, and the n-side contact, Cr/AuGe/Au 2 nm/6 nm/250 nm, was evaporated. Finally, devices approximately 550 μm in length were cleaved from the chip. Figure 8.4 shows several scanning electron microscope

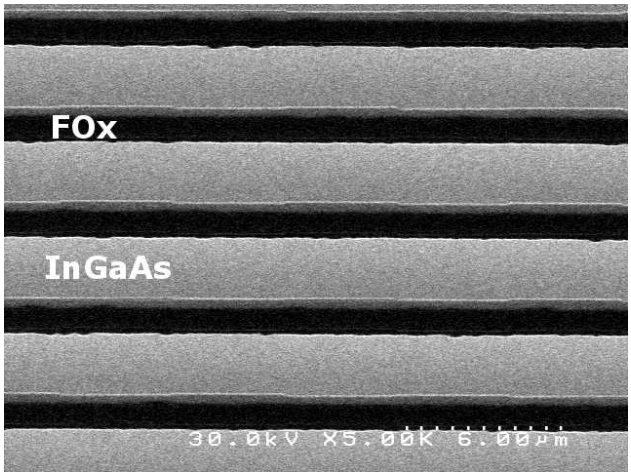

(a)

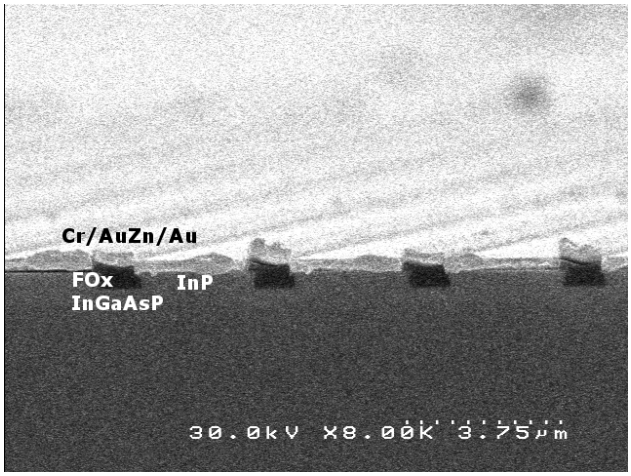

(b)

Figure 8.4: Scanning electron micrographs of the (a) the top view of the FOx overlay that backfilled the trenches and (b) the cross-section of a completed device

images of the fabricated devices.

8.3 Measurement

We measured the transmission spectrum at each of the coupled resonators for various injection current levels. The measurement setup is shown in Fig. 8.5. To measure the devices, we coupled light from a tunable laser (Agilent 81640A) from free-space to a resonator facet near the center of the device. The devices were mounted onto cop-

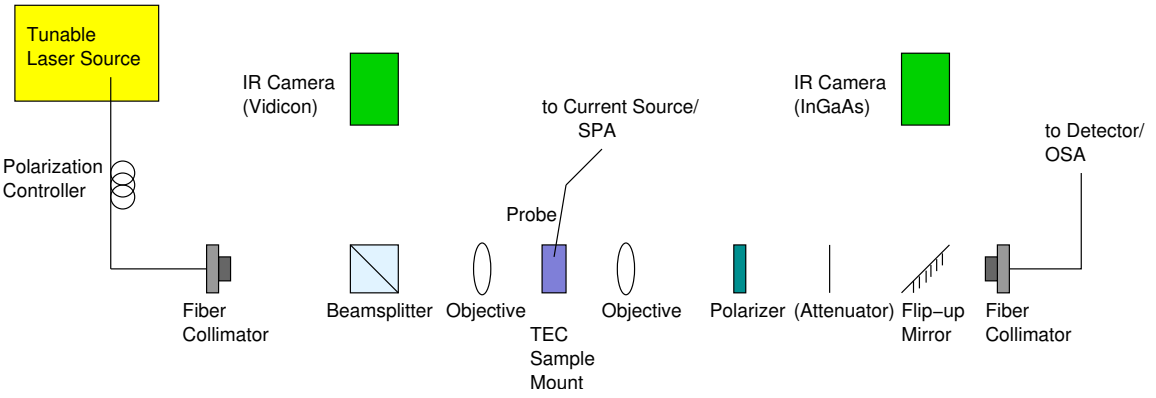

Figure 8.5: Schematic of the experimental setup. SPA is the semiconductor parameter analyzer and OSA is the optical spectrum analyzer.

per bars using an electrically and thermally conductive epoxy (H2OE-LV, Epotek) and onto a thermoelectric cooling (TEC) stage. The temperature was maintained at 20°C. We then imaged the output of the device using a high-sensitivity InGaAs camera (Goodrich SU640SDV-1.7RT) to measure the transmission amplitude at each waveguide position. The waveguide positions could be readily identified from the near-field image of the device, an example of which is shown in Fig. 8.6(a). We investigated TE polarized light which experiences more gain compared to the TM polarization [153].

The devices were pumped with current pulses with a temporal width of 200 ns and a period of 10 μs using a pulsed current source (HP 8114A). The integration time of the camera, of the order of milliseconds, was significantly longer than the pulse width and period, which automatically averaged the transmission amplitude. Laser action was observed in the devices, with a threshold peak current density around $J_{th} \approx 750$ A/cm^2, indicating that losses could be completely compensated. Fig. 8.6(b) shows a typical light-current curve.

8.4 Results

For the transmission measurements, we operated the devices below threshold. For comparisons with theory, we used the transfer matrix method from the last chapter

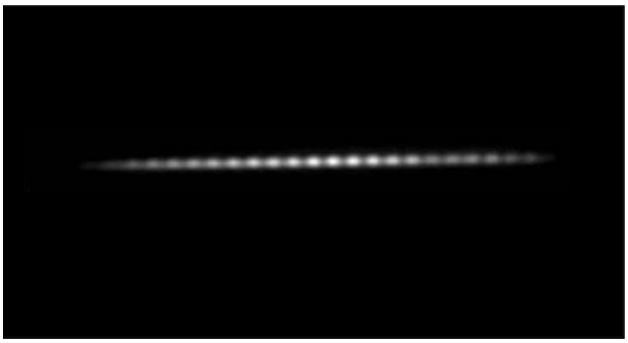

(a)

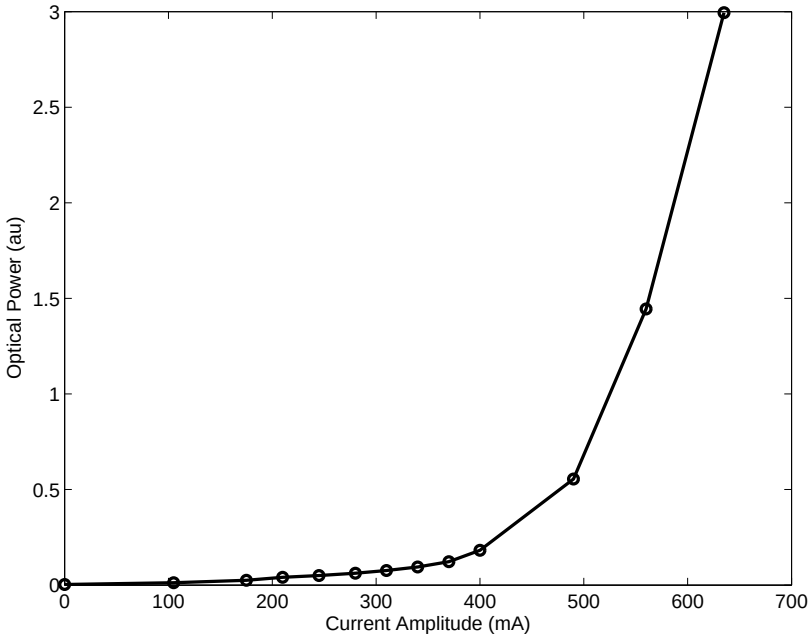

(b)

Figure 8.6: (a) Sub-threshold near-field image. (b) A typical optical power vs. injection current curve.

and set the field amplification for central 25 waveguides to be 534 cm^{-1} to simulate the sub-threshold regime and the losses for the outer resonators to be 5.6 cm^{-1} to model the unpumped region. The calculated normalized transmission spectra and group delay did not depend strongly on the specific value of gain we chose as long as the calculations remained numerically stable. We did not include spontaneous emission into the transfer matrices.

Fig. 8.7 shows the transmission spectra for two devices with inter-resonator separations of 800 nm and 900 nm, resulting in per length coupling constants of $\kappa_l = 1.1 \times 10^{-3}$ μm^{-1} and $\kappa_l = 0.9 \times 10^{-3}$ μm^{-1} respectively. The spatial profile of the waveguide mode was calculated with a mode-solver. The input light was focussed onto the zeroth resonator. The amplitude of the injection current was 280 mA corresponding to approximately $0.7J_{th}$. For these plots, the spontaneous emission background in the absence of the input was subtracted from the measured amplitude. There is generally good agreement between the theoretical and experimental results. Since the spontaneous emission could be subtracted as a background, the noise was not dominated by the beating between the signal and the spontaneous emission.

Fig. 8.8 shows the transmission spectra for the devices at various values of pump current amplitudes without subtracting the spontaneous emission background in the absence of an input. The theoretical group delay is included as well. The dotted lines in Fig. 8.8(a), (b), (f), and (g) indicate the resonance wavelengths of a single resonator. The spectra are normalized to the maximum power at a current amplitude of 310 mA.

As evidenced by the plots, the transmission spectra vary strongly as a function of position and coupling strengths, and that both peaks and notches can occur on resonance. The spectra at 280 mA are in the closest agreement with the theoretical calculations. The highest transmission amplitude does not occur at the band-edges but at the band-center even though the group delay is smaller. This can be understood from the arguments in Chapter 6 that a weak resonance is set up in the direction of periodicity because of the unpumped regions outside the contact and because the excitation source has varying magnitudes of spatial overlap with the modes

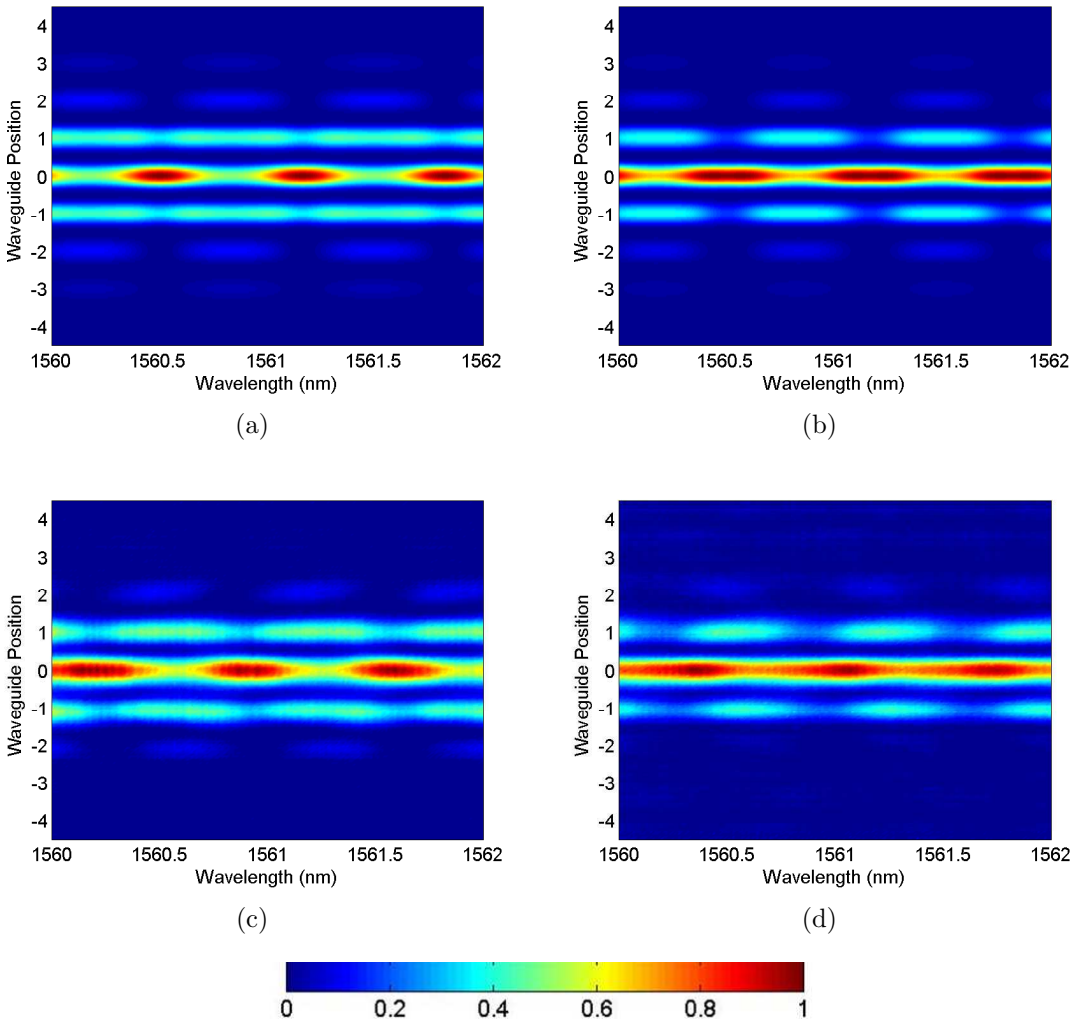

Figure 8.7: The theoretically calculated transmission spectra for (a) $\kappa_l = 1.1 \times 10^{-3}$ μm^{-1} and (b) $\kappa_l = 0.9 \times 10^{-3}$ μm^{-1}, and the measured transmission spectra, less the spontaneous emission background, at a current amplitude of 280mA for an array with inter-resonator spacings of (c) 800 nm and (d) 900 nm

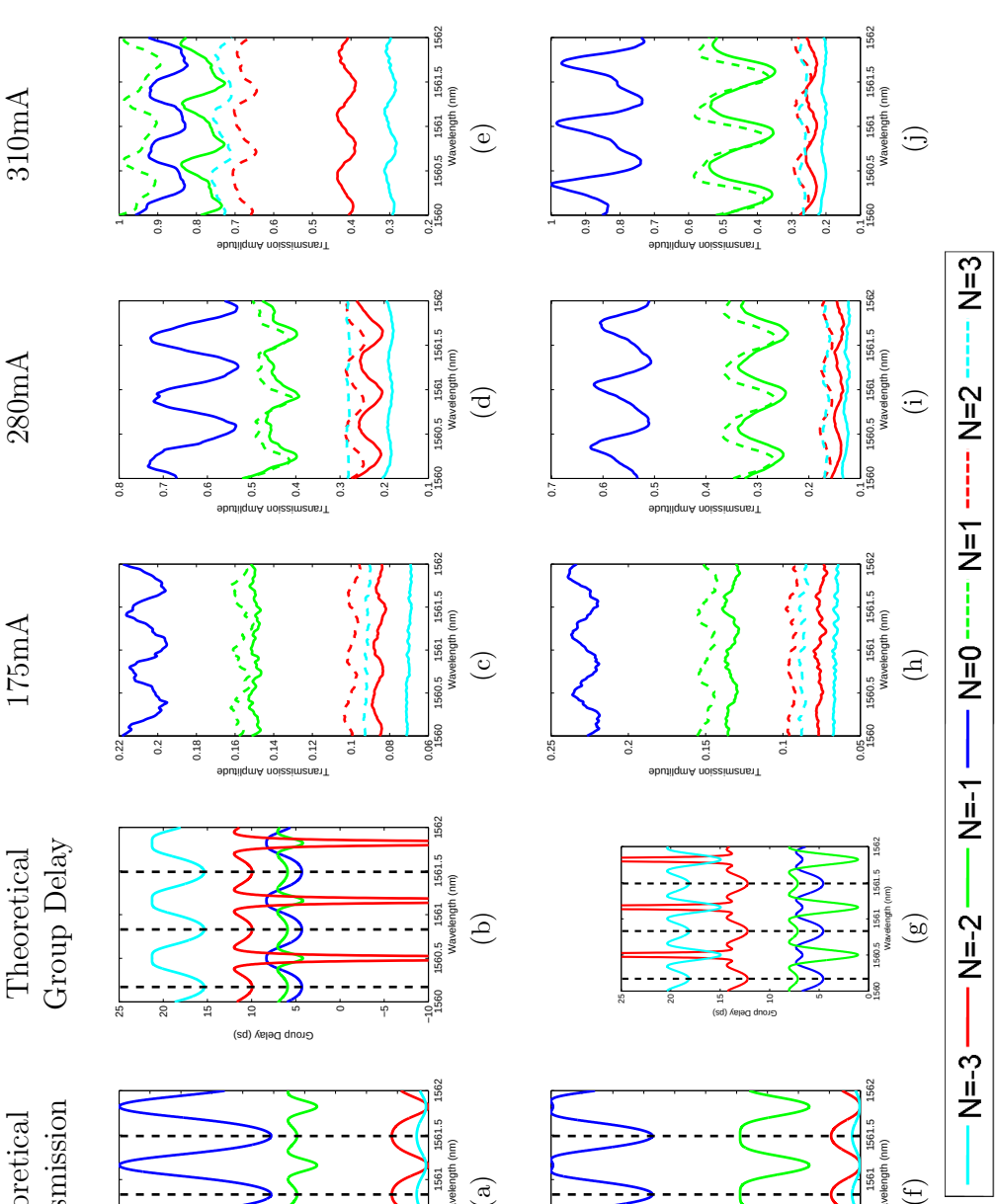

Figure 8.8: Top row: The theoretical (a) transmission and (b) group delay as well as (c)–(e) the experimentally measured transmission spectra at various resonators and injection current amplitudes for an array with an inter-resonator spacing of 800 nm. Bottom row (f)–(j): The same for an array with an inter-resonator spacing of 900 nm

of the structure. The group delay away from the band-center can be both positive and negative depending on the inter-resonator coupling strength. For lower loss resonators with a higher extinction ratio between the CROW band and the stop band, the anomalous group delays would occur at frequencies where the light is mostly attenuated. Because of the absorption outside the contact region, the transmission spectra do not exhibit sharp peaks.

Ideally, the transmission spectra at the various resonators should be symmetric about the excitation at $N = 0$. However, the measured spectra are asymmetric, which is due to non-uniformity in the gain across the devices and the resonators. The non-uniformity can arise from the electrical contacts, slight errors in the lithographic alignment of the FOx overlay layer, as well as the gain material itself, which contributed to local bright spots in the devices.

Fig. 8.8 suggests that the signal-to-noise ratio (SNR) degraded rapidly as a function of the resonator position. Assuming that the noise was dominated by spontaneous emission only, and not by the beating between the signal and the spontaneous emission, the measured optical power was approximately the sum of the signal and the spontaneous emission background without the input signal. Therefore,

$$\mathrm{SNR_{opt}} = \frac{\text{Output Power with the Input}}{\text{Output Power without the Input}} - 1, \tag{8.1}$$

where $\mathrm{SNR_{opt}}$ is the optical SNR. The electrical SNR is given by $|\mathrm{SNR_{opt}}|^2$. Since we did not spectrally resolve the near-field images, the spontaneous emission power across the entire emission bandwidth of about 40 nm was collected. The noise figure can be determined by dividing the signal-to-total-source spontaneous emission ratio of the input laser source of about 27 dB by $\mathrm{SNR_{opt}}$. Fig. 8.9 shows $\mathrm{SNR_{opt}}$ at an injection current of 280 mA of the resonator array with an inter-resonator spacing of 800 nm for which the transmission spectra are shown in Fig. 8.8(d). Because of the large measurement bandwidth, low input coupling efficiency, and the low quality factors of the resonators, $\mathrm{SNR_{opt}}$ decreased to near zero after only a few resonators. Moreover, because of the resonant nature of CROWs, $\mathrm{SNR_{opt}}$ depended strongly on

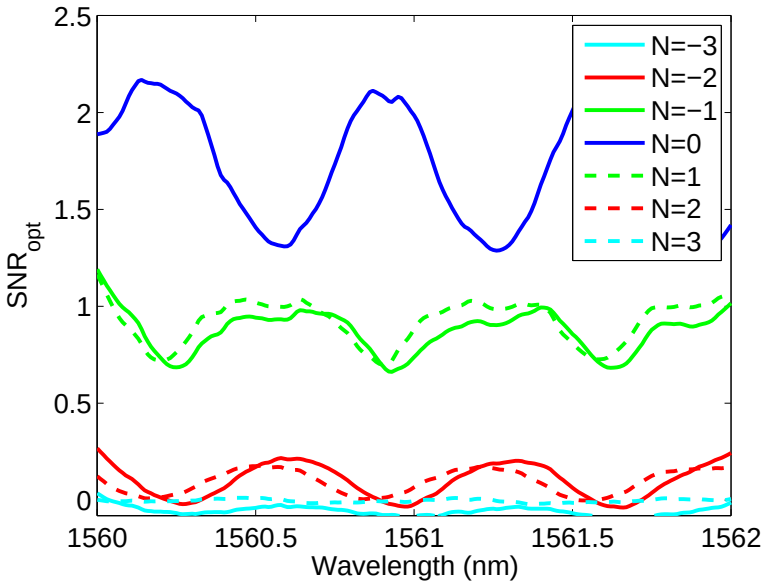

Figure 8.9: SNR_{opt} as a function of wavelength and resonator position of an array with a transmission spectrum shown in Fig. 8.8(d)

the wavelength.

8.5 Discussion

Our demonstration represents the first steps toward realizing active CROWs, illustrating a number of technical challenges in these devices. First, because ideally CROWs consist of a very large number of resonators, the fabricated device must be uniform over its footprint. This requires uniformity in the material, etching, and electrical contacts. Second, continuous-wave (CW) operation of these devices is desirable and would enable accurate measurements of the phase response or group delay of these structures. CW operation requires improved heat dissipation that should be achievable with buried structures and improved contact resistivity.

The SNR should be increased and the noise figure should be decreased for CROWs to be practical. While the Fabry-Perot resonator arrays with cleaved facets are simplest to implement, a relatively low facet reflectivity of $\sim 30\%$ implies that these resonators possess high optical losses so a high gain is necessary. High reflectivity

mirrors, in the form of gratings for example, can be incorporated to improve the quality factors of the resonators. Asymmetric cavity designs with unequal mirror reflectivity at the two facets can reduce the amount of measured spontaneous emission noise [135]. Higher input coupling efficiency would also improve the amount of signal power coupled into the CROW to increase the SNR. This can be achieved by incorporating input and output waveguides with mode converters much like microring CROWs or the proposed side-coupled Fabry-Perot CROWs [34, 133].

Lastly, since the introduction of gain allows for laser oscillation, an important question is whether CROWs should be operated above or below laser threshold. There are benefits and disadvantages to both types of operation. Sub-threshold operation is simpler to understand and model, but requires highly accurate fabrication to ensure that the resonators are identical to each other. Moreover, to suppress laser action in the CROW, the input and output coupling constants as well as the inter-resonator coupling strength should be large, which place a lower limit on the group velocity and net amplification attainable [126].

Operation above threshold is more complicated to analyze because locking effects may come into play but can be more interesting fundamentally. Above threshold, the CROW can lock to the input signal and also the resonators can become phase coherent with each other. Phase-locked laser arrays have been studied extensively both theoretically and experimentally for several decades [143, 153]. Phase-locking can occur even if the uncoupled elements are not exactly identical. The locking range, or the maximum allowed detuning for the uncoupled resonators, depends on the gain and the complex coupling coefficient between the resonators [143, 154]. In general, the stronger the coupling, the larger the locking range. By increasing the optical gain, the locking range can be increased, and thus a larger variation in the uncoupled resonator resonance frequencies can be tolerated. Therefore, a light pulse centered at the laser frequency can effectively propagate through a chain of identical resonators.

On the other hand, a CROW laser can also lock to the input signal through the process of injection-locking so the input changes the operation of the CROW itself [153, 155, 156, 157]. Injection-locking can be used to tune the resonance frequency

of the array to or away from the central wavelength of an optical pulse to be propagated through the array. This may be a simple way to modify the dispersion of an input optical pulse to the array. Laser action can also clamp the gain, which may help in stabilizing the operation of an amplifying CROW much like gain-clamped semiconductor optical amplifiers [158, 159, 160].

8.6 Summary

We have measured the transmission spectra of electrically pumped Fabry-Perot resonator array CROWs fabricated in InP-InGaAsP. The devices could behave as lasers, indicating that losses could be completely compensated. The transmission spectra and the SNR were strongly dependent on the injection current and resonator position. The SNR of the devices degraded rapidly away from the input resonator. The devices can be improved through fabrication uniformity, lower loss resonators, and increased input coupling efficiency. We have also highlighted some possible avenues to operate laser arrays as loss-compensated or amplifying CROWs.

Appendix A

Transfer and Scattering Matrices

A.1 Introduction

We have used transfer and scattering matrices extensively in this work. Here, we shall briefly outline some properties of these matrices and illustrate how they can be applied to analyze other types of coupled resonator geometries. Specifically, we shall study two examples: 1. a coupled system of a standing wave and travelling wave resonator (a Fabry-Perot and a ring resonator) and 2. a circular array of ring resonators.

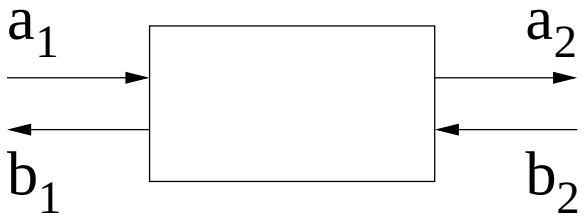

Figure A.1: A four port element

A.2 Preliminaries

For a 4 port element as in Fig. A.2, the output fields are related to the input fields by a transfer matrix, $\mathbf{M}$,

$$\begin{bmatrix} a_2 \\ b_2 \end{bmatrix} = \mathbf{M} \begin{bmatrix} a_1 \\ b_1 \end{bmatrix}. \tag{A.1}$$

If the system has time reversal symmetry, then

$$\begin{bmatrix} t \\ 0 \end{bmatrix} = \mathbf{M} \begin{bmatrix} 1 \\ r \end{bmatrix}, \begin{bmatrix} 0 \\ t^* \end{bmatrix} = \mathbf{M} \begin{bmatrix} r^* \\ 1 \end{bmatrix}, \tag{A.2}$$

where t and r are the transmission and reflection coefficients, leading to a transfer matrix of the form

$$\mathbf{M} = \begin{bmatrix} \frac{1}{t^*} & -\frac{r^*}{t^*} \\ -\frac{r}{t} & \frac{1}{t} \end{bmatrix}. \tag{A.3}$$

On the other hand, if there is mirror symmetry, then

$$\begin{bmatrix} t \\ 0 \end{bmatrix} = \mathbf{M} \begin{bmatrix} 1 \\ r \end{bmatrix}, \begin{bmatrix} r \\ 1 \end{bmatrix} = \mathbf{M} \begin{bmatrix} 0 \\ t \end{bmatrix}, \tag{A.4}$$

which leads to a matrix of the form

$$\mathbf{M} = \begin{bmatrix} \frac{t^2-r^2}{t} & \frac{r}{t} \\ -\frac{r}{t} & \frac{1}{t} \end{bmatrix}. \tag{A.5}$$

Therefore, if the system possesses both mirror and time reversal symmetry, and if we can choose the phase such that $t = t^*$, then

$$-r^* = r, \tag{A.6a}$$

$$t^2 - r^2 = 1. \tag{A.6b}$$

A.3 Examples of Transfer Matrices

Knowing the form of the transfer matrices, we can readily find out their explicit expressions for specific waveguide or device components. In this section, we show several examples of transfer matrices.

A.3.1 Waveguide

As a simple example, the scattering matrix of a waveguide of length L is given by

$$M_L = \begin{bmatrix} \exp(-i\beta L) & 0 \\ 0 & \exp(i\beta L) \end{bmatrix}, \tag{A.7}$$

where β is the propagation constant of the waveguide.

A.3.2 Grating

From coupled-mode theory, we have the reflection and transmission coefficients for a grating with a sinusoidal index perturbation [44]:

$$r_G = \frac{-i\kappa_G^* \sinh(sL_G)}{s\cosh(sL_G) + i\frac{\Delta\beta}{2}\sinh(sL_G)}, \tag{A.8a}$$

$$t_G = \frac{s\exp(i\Delta\beta\frac{L_G}{2})}{s\cosh(sL_G) + i\frac{\Delta\beta}{2}\sinh(sL_G)}. \tag{A.8b}$$

L_G is the length of the grating. κ_F is the per-length grating coupling coefficient given by

$$\kappa_G = \frac{\pi(n_2^2 - n_1^2)}{\lambda\sqrt{n_2^2 + n_1^2}}, \tag{A.9}$$

where n_1 is the minimum index of refraction and n_2 is the maximum. $\Delta\beta$ is the phase-mismatch between the incoming and outgoing wave, which for a single-mode waveguide is

$$\Delta\beta = 2\beta - \frac{2\pi}{\Lambda}, \tag{A.10}$$

where Λ is the grating period, $\beta = 2\pi\bar{n}/\lambda$, and $\bar{n} = \sqrt{(n_1^2 + n_2^2)/2}$. Lastly, s is related to the difference between κ_F and $\Delta\beta$,

$$s^2 = |\kappa_F|^2 - \left(\frac{\Delta\beta}{2}\right)^2. \tag{A.11}$$

Therefore, we substitute t_G and r_G into Eq. (A.3) to obtain $\mathbf{M}_G$, the transfer matrix for a lossless, uniform grating.

A.3.3 Waveguide Coupled to a Ring Resonator

The transfer function of a waveguide coupled to a ring resonator described by Eq. (4.2) can also be expressed in terms of a transfer matrix, where the transmission coefficient of the ring is given by

$$t_R = \frac{t_r \exp(i\beta 2\pi R) - \alpha_r}{\exp(i\beta 2\pi R) - \alpha_r t_r}, \tag{A.12}$$

where α_r is the fractional round-trip attenuation or the amplification factor of the field in the ring, and κ_r and t_r are the coupling and transmission coefficients between the ring and the waveguide. If there is no coupling between the clockwise and counter-clockwise propagating waves in the resonator, $r_R = 0$. t_R and $r_R = 0$ can be substituted into Eq. (A.5) to obtain the transfer matrix $\mathbf{M}_R$.

A.4 Coupled Ring-Fabry-Perot Resonators

As an example, let us examine the coupled system between a Fabry-Perot and a ring resonator as shown in Fig. A.4 [161]. The transmission and reflection coefficients of the composite structure are given by the product of the transfer matrices representing each element.

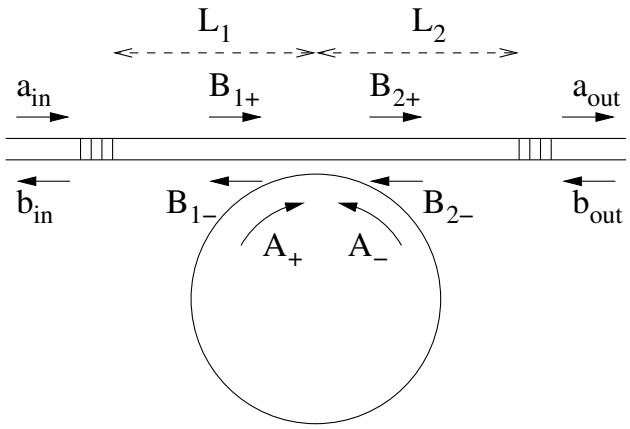

Figure A.2: Fabry-Perot resonator coupled to a microring resonator

$$\begin{bmatrix} a_{out} \\ b_{out} \end{bmatrix} = \mathbf{M}_{sys} \begin{bmatrix} a_{in} \\ b_{in} \end{bmatrix} \equiv \begin{bmatrix} A & B \\ C & D \end{bmatrix} \begin{bmatrix} a_{in} \\ b_{in} \end{bmatrix}, \tag{A.13}$$
$$\mathbf{M}_{sys} = \mathbf{M}_{G2}\mathbf{M}_{L2}\mathbf{M}_{R}\mathbf{M}_{L1}\mathbf{M}_{G1}.$$

Since $b_{out} = 0$, the transmission and reflection coefficients are given by

$$T = \frac{a_{out}}{a_{in}} = \frac{AD - BC}{D}, \tag{A.14a}$$

$$R = \frac{b_{in}}{a_{in}} = -\frac{C}{D}. \tag{A.14b}$$

Several examples of the transmission spectra calculated from Eq. (A.13) and (A.14) are shown in Fig. A.3 in the case where the Q of the ring resonator is significantly higher than that of the Fabry-Perot. The Q factor for the ring resonator is 2.2×10^{11} and the Q factor for the Fabry-Perot resonator is 5.1×10^{8}. For the calculations, $\alpha_r = t_r$ such that the critical coupling condition is satisfied. An asymmetric lineshape arises when the resonance frequency of the ring resonator is detuned from that of the Fabry-Perot. A "hole" in the transmission of the Fabry-Perot resonator occurs at the resonance of the ring resonator. These transmission spectra have been experimentally observed in a coupled system of a fiber Bragg grating resonator and

a high-Q microtoroid [161]. Because of the rapidly varying phase and amplitude responses with respect to the wavelength, we expect large group delays are possible at the frequencies where the transmission is maximum.

A.5 Circular Arrays of Ring Resonators

As another example of the utility of transfer matrices, we propose and analyze a novel type of wavelength-selective reflector based on a circular array of coupled microring resonators[1]. Narrow-band reflection peaks can be achieved with the reflector. The ring resonators also allow for simple and wide-range tuning of the reflection peak. The circular array consists of $N > 2$ ring resonators coupled to a waveguide as shown in Fig. A.4. The circular array can also be regarded as a "super" ring resonator formed by a microring CROW. A wave propagating in the waveguide excites a travelling wave inside the ring resonator array. From Fig. A.4, we observe that for an odd number of rings ($N \geq 3$), the device may act as a reflector, but for an even number of rings ($N \geq 4$), the device is always non-reflecting.

A.5.1 Transfer Matrix Analysis

To analyze light propagation in the resonator array, we use a transfer matrix formalism. The symbols used are summarized in Table A.1. The forward and backward propagating field components are defined in Fig. A.5. We use the vector x_n to represent the field components in the $n-1^{th}$ ring,

$$x_n \equiv \begin{bmatrix} a & b & c & d \end{bmatrix}_n^T. \tag{A.15}$$

To describe the coupling of waves between adjacent resonators, we assume that the coupling length is much greater than the wavelength of light such that only the phase-matched waves are coupled. Hence, there is no mixing between the clockwise

[1] ©2004 IEEE. Reprinted, with permission, from [162].

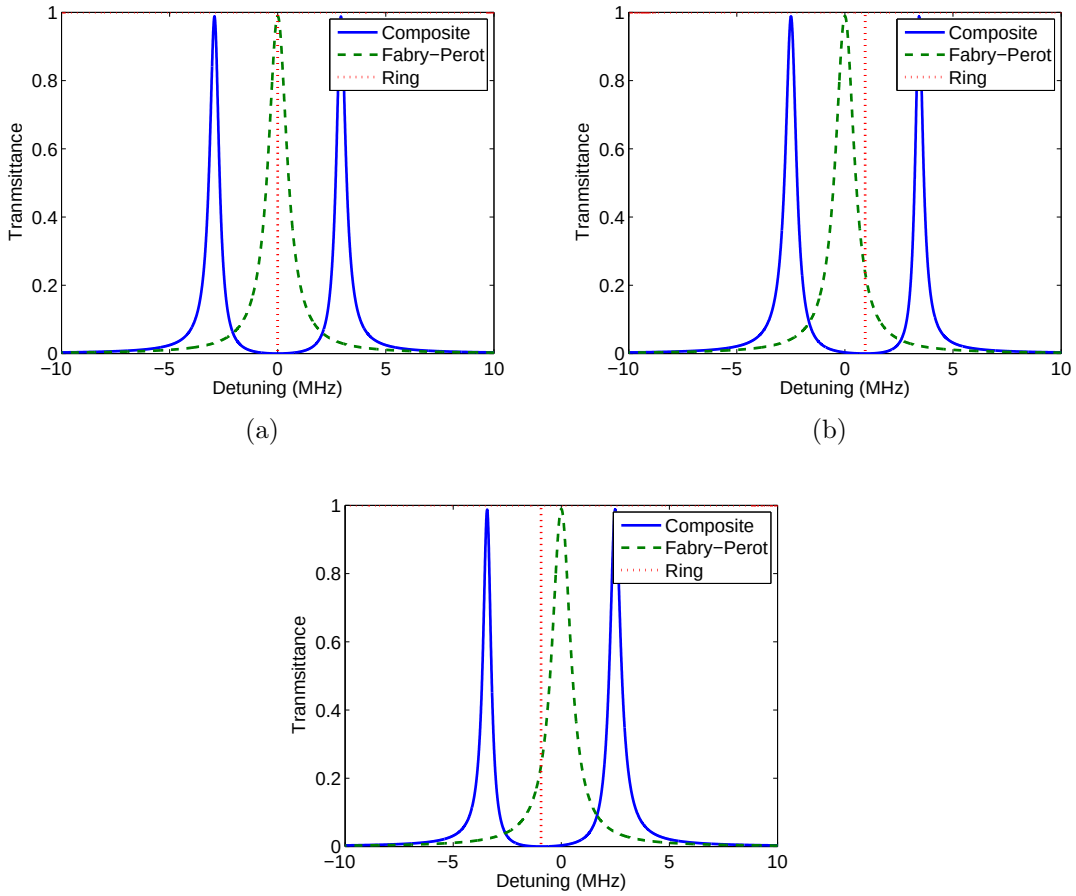

Figure A.3: The calculated transmission spectra for a Fabry-Perot resonator coupled to a ring resonator in the cases where (a) the ring and Fabry-Perot resonance frequencies are the same, (b) the ring resonance frequency is positively detuned from the Fabry-Perot, and (c) the ring resonance frequency is negatively detuned from the Fabry-Perot. The uncoupled Fabry-Perot and ring resonator transmission spectra are also shown for reference.

Table A.1: List of Symbols

Symbol	**Significance**
a_n, b_n, c'_n, d'_n	counter-clockwise propagating fields
c_n, d_n, a'_n, b'_n	clockwise propagating fields
x_n	field vector $[a, b, c, d]_n$
κ	coupling coefficient
t	transmission coefficient
β	propagation constant
α	gain or loss, imaginary part of β
θ	angle of an external vertex of an equilateral polygon

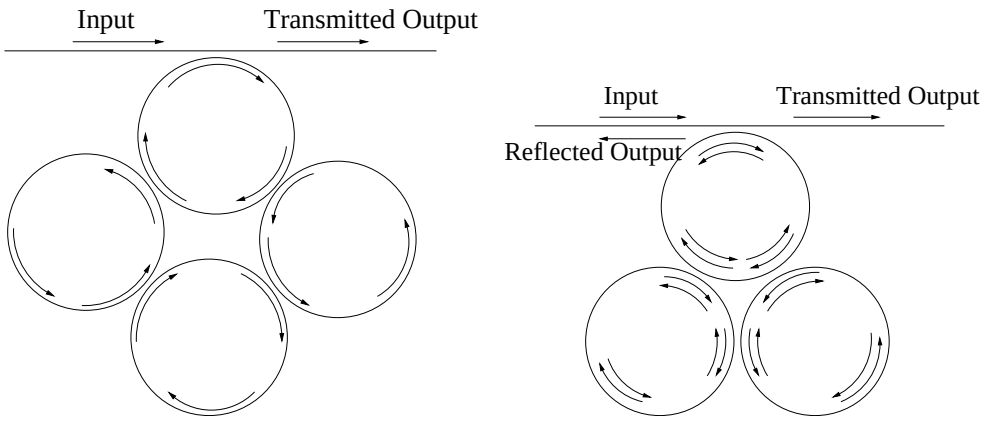

Figure A.4: Schematic of the reflector. (a) For an even number of rings, the device is always transmitting. (b) For an odd number of rings, the device can be reflecting.

and counter-clockwise propagating waves, and the coupling can be represented by a 4×4 matrix:

$$x_{n+1} = \begin{bmatrix} P & 0 \\ 0 & P \end{bmatrix} x'_n \equiv \mathbb{P} x'_n, \tag{A.16a}$$

$$P = \frac{1}{\kappa} \begin{bmatrix} -t & 1 \\ -1 & t^* \end{bmatrix}, \quad n \geq 0, \tag{A.16b}$$

where κ and t are the dimensionless coupling and transmission coefficients. P is unitary such that $|\kappa|^2 + |t|^2 = 1$.

We can relate x'_n and x_n with a propagation matrix such that

$$x'_n = \begin{bmatrix} 0 & Q \\ Q^\dagger & 0 \end{bmatrix} x_n \equiv \mathbb{Q} x_n, \tag{A.17a}$$

$$Q = \begin{bmatrix} 0 & \mathrm{e}^{-i\beta R\theta} \\ \mathrm{e}^{i\beta R(2\pi-\theta)} & 0 \end{bmatrix}, \tag{A.17b}$$

where β is the propagation constant, R is the radius of the rings, $Q^\dagger$ is the conjugate transpose of Q, and θ is determined from the internal angles of the polygon whose vertices are located at the centers of the rings. β may be complex, such that $\beta =$

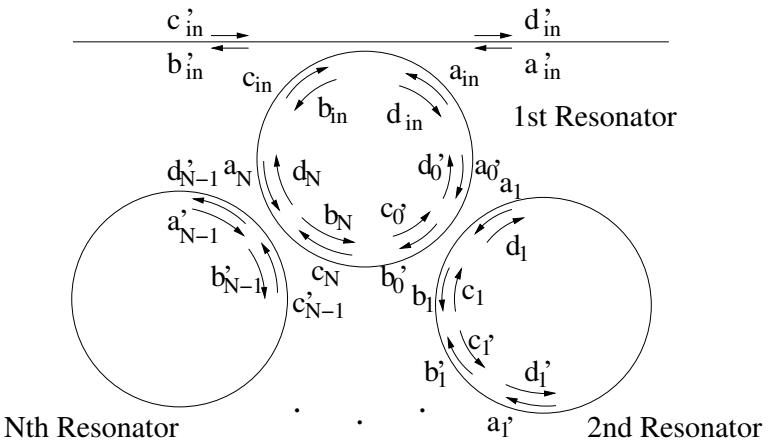

Figure A.5: A circular array of an arbitrary number of rings with the clockwise and counter-clockwise fields labelled

$n_{\text{eff}}\omega/c + i\alpha$, to account for loss or gain. For an equilateral polygon, θ is

$$\theta = 2\pi - \frac{\pi(N-2)}{N}. \tag{A.18}$$

Combining (A.16) and (A.17),

$$x_{n+1} = \begin{bmatrix} 0 & PQ \\ PQ^{\dagger} & 0 \end{bmatrix} x_n \equiv \mathbb{T}x_n. \tag{A.19}$$

For N ($N > 2$) ring resonators in the circular chain, we cascade the matrices to obtain

$$x_N = \mathbb{T}^{N-1}\mathbb{P}x_0'. \tag{A.20}$$

Our goal is to find an expression that depends solely on x_{in}', since the components of x_{in}' will give the transfer functions of the structure. Thus, we seek to manipulate (A.20) into the form

$$x_{in}' = Bx_{in}', \tag{A.21}$$

where B is a matrix to be determined. (A.21) also has the form of an eigenvalue problem with an eigenvalue of 1.

To begin, we note that at the first resonator, the coupling to the external wave-

guide is

$$x_{in} = \mathbb{P}_{in} x'_{in}. \tag{A.22}$$

Moreover, there are 6 phase relations in the first resonator:

$$\begin{aligned} a'_0 &= d_{in} \mathrm{e}^{-i\beta R\theta/2}, \quad d'_0 = a_{in} \mathrm{e}^{i\beta R\theta/2}, \\ b'_0 &= c_N \mathrm{e}^{i\beta R(2\pi-\theta)}, \quad c'_0 = b_N \mathrm{e}^{-i\beta R(2\pi-\theta)}, \\ a_N &= b_{in} \mathrm{e}^{-i\beta R\theta/2}, \quad d_N = c_{in} \mathrm{e}^{i\beta R\theta/2}. \end{aligned} \tag{A.23}$$

We use (A.23) to express x_N and x'_0 in terms of elements in x_{in} in (A.20). b_N and c_N simplify to

$$\left.\begin{aligned} b_N &= \tfrac{a_{in} A_{24} \mathrm{e}^{i\beta R\theta/2}}{1 - A_{23} \mathrm{e}^{-i\beta R(2\pi-\theta)}} \\ c_N &= \tfrac{d_{in} A_{31} \mathrm{e}^{-i\beta R\theta/2}}{1 - A_{32} \mathrm{e}^{i\beta R(2\pi-\theta)}} \end{aligned}\right\} N = \text{even}, \tag{A.24a}$$

$$\left.\begin{aligned} b_N &= \tfrac{d_{in} A_{21} \mathrm{e}^{-i\beta R\theta/2} + a_{in} A_{22} A_{34} \mathrm{e}^{i\beta R(2\pi+\theta/2)}}{1 - A_{22} A_{33}} \\ c_N &= \tfrac{a_{in} A_{34} \mathrm{e}^{i\beta R\theta/2} + d_{in} A_{21} A_{33} \mathrm{e}^{-i\beta R(2\pi-\theta/2)}}{1 - A_{22} A_{33}} \end{aligned}\right\} N = \text{odd}, \tag{A.24b}$$

where A_{ij} is the ij^{th} element of A and $A \equiv \mathbb{T}^{N-1}\mathbb{P}$. Hence, invoking (A.22), we can rewrite (A.20) as

$$M \mathbb{P}_{in} x'_{in} = \mathbb{T}^{N-1} \mathbb{P} W \mathbb{P}_{in} x'_{in}, \tag{A.25}$$

where M and W express b_N, c_N, b'_0, and c'_0 using (A.23) and (A.24). Finally, we can rewrite (A.25) in our desired form (A.21):

$$x'_{in} = \mathbb{P}_{in}^{-1} M^{-1} \mathbb{T}^{N-1} \mathbb{P} W \mathbb{P}_{in} x'_{in} \equiv B x'_{in}. \tag{A.26}$$

However, $\mathrm{Det}(W) = 0$, rendering B non-invertible. This is expected because physically the system is fully characterized relative to a single input, so the four components of x'_{in} are not linearly independent variables. Thus, we have some freedom in selecting the form of the eigenvector x'_{in}. Assuming only a single input, we set one of the inputs to the circular chain of rings to zero, say a'_{in}, and we take the transmission

and reflectance relative to c'_{in}. The resultant eigenvector has the form

$$x'_{in} = \begin{bmatrix} 0 & b'_{in} & 1 & d'_{in} \end{bmatrix}^T, \tag{A.27}$$

where d'_{in} is the transmission function and b'_{in} is the reflection function. They can be calculated by solving the matrix equation

$$\begin{bmatrix} \frac{B_{42}}{1-B_{44}} & -1 \\ 1 & -\frac{B_{24}}{1-B_{22}} \end{bmatrix} \begin{bmatrix} b'_{in} \\ d'_{in} \end{bmatrix} = \begin{bmatrix} \frac{B_{43}}{1-B_{44}} \\ \frac{B_{23}}{1-B_{22}} \end{bmatrix}, \tag{A.28}$$

where B_{ij} is the ij^{th} element of B. The solution also satisfies

$$B_{32}b'_{in} + B_{33} + B_{34}d'_{in} = 1 \tag{A.29a}$$

$$B_{12}b'_{in} + B_{13} + B_{14}d'_{in} = 0, \tag{A.29b}$$

ensuring that it is self-consistent with (A.26).

A.5.2 Results and Discussion

We use (A.28) to compute the reflectance and transmittance spectra of the circular array based reflector. For an even number of rings, the structure is verified to be purely transmitting. For lossless rings, the even number of rings acts as an all-pass filter. Figs. A.6(a) and A.6(b) show the transmission and phase characteristics of an array of 4 resonators. The inter-resonator coupling is $\kappa = -0.5i$ and the coupling between the waveguide and the array is also $\kappa_i = -0.5i$. The radius of the rings is 100 μm and their effective index is 1.5. The transmission drops and the phase changes most rapidly at the resonances of the "super" resonator. The phase response is not strongly dependent on loss.

Figs. A.6(c) and A.6(d) show the spectra of 3 coupled resonators for various losses. The inter-resonator coupling is $\kappa = -0.08i$ and the coupling between the waveguide and the array is $\kappa_i = -0.53i$. The radius of the rings is 100 μm and their effective

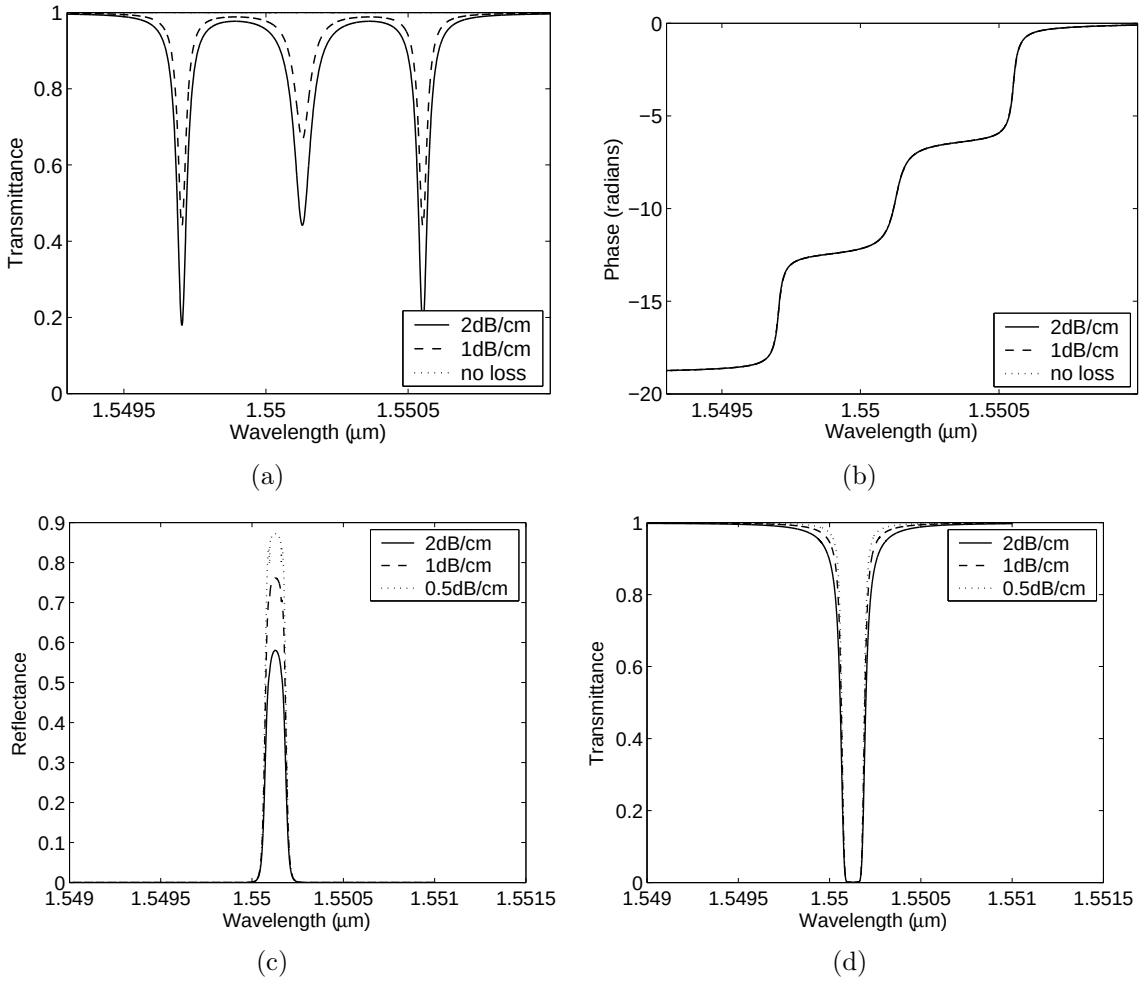

Figure A.6: Top: The transmittance (a) and phase response (b) of an array of 4 resonators for various losses. $\kappa = -0.5i$, $\kappa_i = -0.5i$. Bottom: The reflectance (c) and transmittance (d) of an array of 3 resonators for various losses. $\kappa = -0.08i$, $\kappa_i = -0.53i$. For both cases, $r = 100$ μm and $n_{\text{eff}} = 1.5$.

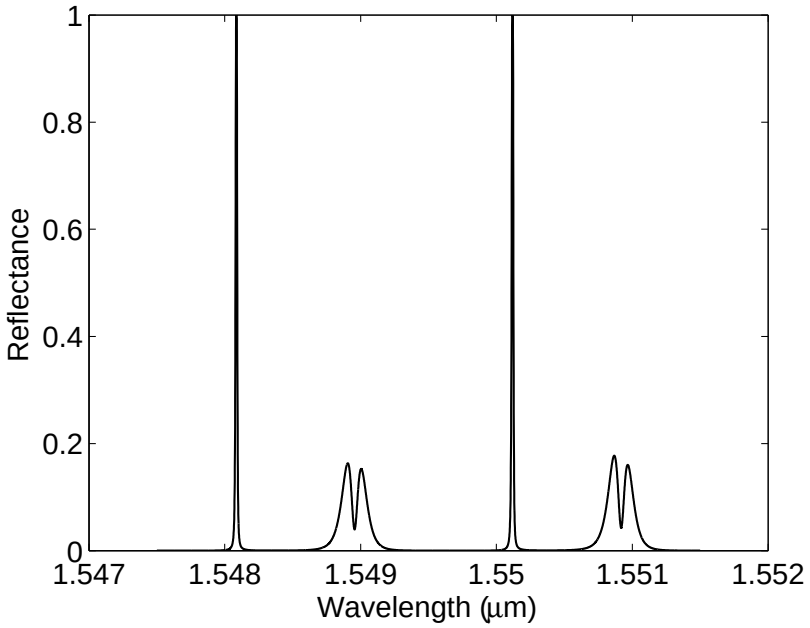

Figure A.7: The reflectance of an array consisting of 3 different resonators. $r_{1,3} = 130$ μm, $r_2 = 125$ μm, $\kappa = -0.3i$, $\kappa_i = -0.85i$.

index is 1.5. The structure exhibits a narrow reflection peak centered at 1.55 μm and its free spectral range is 2.4 nm. The maximum reflectance achievable is inversely proportional to the propagation loss in the rings. In general, to obtain narrow reflection peaks, weak inter-resonator coupling is required. For filtering applications, the input coupling can be chosen to optimize the flatness of the transmission and reflection spectra.

An advantage to the matrix formalism is that it can readily deal with an array composed of an arbitrary mix of resonators and coupling constants simply by accounting for the differences in resonator sizes, coupling, and internal angles in the transfer matrices. By varying the resonators, we can more finely tune the strongly reflected frequencies. Fig. A.7 shows the reflectance spectrum for an array of 3 resonators in which the second resonator is of a different size. The rings are lossless with inter-resonator coupling of $-0.3i$ and the coupling to the waveguide is $-0.85i$. The first and third rings (using the notation in Fig. A.5) have a radius of $r_{1,3} = 130$ μm, while the second ring has a radius of $r_2 = 125$ μm. The main reflection peaks are

spaced 2 nm apart. However, even though the coupling coefficients are higher than the previous example, the reflection peaks are narrower than the structure composed of identical resonators with a smaller coupling strength (as in Fig. A.6(c)). The use of different resonators provides an additional degree of freedom to obtain narrow reflection peaks.

References

[1] A. Yariv. *Optical Electronics in Modern Communications.* Oxford University Press, New York, 5th edition, 1997.

[2] K. J. Vahala. Optical microcavities. *Nature*, 424(6950):839–846, 2003.

[3] C. K. Madsen. General IIR optical filter design for WDM applications using all-pass filters. *J. Lightwave Technol.*, 18(6):860–868, 2000.

[4] B. E. Little, S. T. Chu, W. Pan, D. Ripin, T. Kaneko, Y. Kokubun, and E. Ippen. Vertically coupled glass microring resonator channel dropping filters. *IEEE Photon. Technol. Lett.*, 11(2):215–217, 1999.

[5] B. E. Little, S. T. Chu, H. A. Haus, J. Foresi, and J.-P. Laine. Microring resonator channel dropping filter. *J. Lightwave Technol.*, 15(6):998–1005, 1997.

[6] M. L. Gorodetsky, A. A. Savchenkov, and V. S. Ilchenko. Ultimate Q of optical microsphere resonators. *Opt. Lett.*, 21(7):453–455, 1996.

[7] M. Cai, O. Painter, and K. J. Vahala. Observation of critical coupling in a fiber taper to a silica-microsphere whispering-gallery mode system. *Phys. Rev. Lett.*, 85(1):74–77, 2000.

[8] S. L. McCall, A. F. J. Levi, R. E. Slusher, S. J. Pearton, and R. A. Logan. Whispering-gallery mode microdisk lasers. *Appl. Phys. Lett.*, 60(3):289–291, 1992.

[9] D. K. Armani, T. J. Kippenberg, S. M. Spillane, and K. J. Vahala. Ultra-high-Q toroid microcavity on a chip. *Nature*, 421(6926):925–928, 2003.

[10] B. E. Little, S. T. Chu, P. P. Absil, J. V. Hryniewicz, F. G. Johnson, F. Seiferth, D. Gill, V. Van, O. King, and M. Trakalo. Very high-order microring resonator filters for WDM applications. *IEEE Photon. Technol. Lett.*, 16(10):2263–2265, 2004.

[11] C. K. Madsen and J. H. Zhao. *Optical Filter Design and Analysis: A Signal Processing Approach*. Wiley, New York, 1999.

[12] P. Rabiei, W. H. Steier, C. Zhang, and L. R. Dalton. Polymer micro-ring filters and modulators. *J. Lightwave Technol.*, 20(11):1968–1975, 2002.

[13] T. J. Kippenberg, S. M. Spillane, and K. J. Vahala. Kerr-nonlinearity optical parametric oscillation in an ultrahigh-Q toroid microcavity. *Phys. Rev. Lett.*, 93(8):083904, 2004.

[14] H. Rokhsari, T. J. Kippenberg, T. Carmon, and K. J. Vahala. Radiation-pressure-driven micro-mechanical oscillator. *Opt. Express*, 13(14):5293–5301, 2005.

[15] C. J. Hood, T. W. Lynn, A. C. Doherty, A. S. Parkins, and H. J. Kimble. The atom-cavity microscope: Single atoms bound in orbit by single photons. *Science*, 287(5457):1447–1453, 2000.

[16] O. Painter, R. K. Lee, A. Scherer, A. Yariv, J. D. O'Brien, P. D. Dapkus, and I. Kim. Two-dimensional photonic band-gap defect mode laser. *Science*, 284(5421):1819–1821, 1999.

[17] J. Scheuer and A. Yariv. Two-dimensional optical ring resonators based on radial Bragg resonance. *Opt. Lett.*, 28(17):1528–1530, 2003.

[18] Y. Xu, W. Liang, A. Yariv, J.G. Fleming, and S.Y. Lin. High-quality-factor Bragg onion resonators with omnidirectional reflector cladding. *Opt. Lett.*, 28(22):2144–2146, 2003.

[19] A. Yariv, Y. Xu, R. K. Lee, and A. Scherer. Coupled-resonator optical waveguide: a proposal and analysis. *Opt. Lett.*, 24(11):711–713, 1999.

[20] N. Stefanou and A. Modinos. Impurity bands in photonic insulators. *Phys. Rev. B*, 57(19):12127–12133, 1998.

[21] A. Melloni and F. Morichetti. Linear and nonlinear pulse propagation in coupled resonator slow-wave optical structures. *Opt. Quant. Electron.*, 35:365–379, 2003.

[22] G. Lenz, B. J. Eggleton, C. K. Madsen, and R. E. Slusher. Optical delay lines based on optical filters. *IEEE J. Quant. Elect.*, 37(4):525–532, 2001.

[23] S. Lan, S. Nishikawa, H. Ishikawa, and O. Wada. Engineering photonic crystal impurity bands for waveguides, all-optical switches and optical delay lines. *IEICE Trans. Electron.*, E85C(1):181–189, 2002.

[24] H. Altug and J. Vuckovic. Experimental demonstration of the slow group velocity of light in two-dimensional coupled photonic crystal microcavity arrays. *Appl. Phys. Lett.*, 86(11):111102, 2005.

[25] Y. Xu, R. K. Lee, and A. Yariv. Propagation and second-harmonic generation of electromagnetic waves in a coupled-resonator optical waveguide. *J. Opt. Soc. Am. B*, 77(3):387–400, 2000.

[26] D. N. Christodoulides and N. K. Efremidis. Discrete temporal solitons along a chain of nonlinear coupled microcavities embedded in photonic crystals. *Opt. Lett.*, 27(8):568–570, 2002.

[27] S. Mookherjea and A. Yariv. Kerr-stabilized super-resonant modes in coupled-resonator optical waveguides. *Phys. Rev. E*, 66(4):046610, 2002.

[28] J. E. Heebner and R. W. Boyd. 'Slow' and 'fast' light in resonator-coupled waveguides. *J. Mod. Opt.*, 49(14-15):2629–2636, 2002.

[29] M. Bayindir, B. Temelkuran, and E. Ozbay. Tight-binding description of the coupled defect modes in three-dimensional photonic crystals. *Phys. Rev. Lett.*, 84(10):2140–2143, 2000.

[30] S. Mookherjea and A. Yariv. Optical pulse propagation in the tight-binding approximation. *Opt. Express*, 9(2):91–96, 2001.

[31] S. Mookherjea and A. Yariv. Optical pulse propagation and holographic storage in a coupled-resonator optical waveguide. *Phys. Rev. E*, 64(6):066602, 2001.

[32] S. Mookherjea and A. Yariv. Pulse propagation in a coupled-resonator optical waveguide to all orders of dispersion. *Phys. Rev. E*, 65(5):056601, 2002.

[33] S. Mookherjea and A. Yariv. Second-harmonic generation with pulses in a coupled-resonator optical waveguide. *Phys. Rev. E*, 65(2):026607, 2002.

[34] J. K. S. Poon, J. Scheuer, S. Mookherjea, G. T. Paloczi, Y. Huang, and A. Yariv. Matrix analysis of microring coupled-resonator optical waveguides. *Opt. Express*, 12(1):90–103, 2004.

[35] J. K. S. Poon, J. Scheuer, Y. Xu, and A. Yariv. Designing coupled-resonator optical waveguide delay lines. *J. Opt. Soc. Am. B*, 21(9):1665–1673, 2004.

[36] A. L. Reynolds, U. Peschel, F. Lederer, P. J. Roberts, T. F. Krauss, and P. J. I. de Maagt. Coupled defects in photonic crystals. *IEEE Trans. Microwave Theory Tech.*, 49(10):1860–1867, 2001.

[37] H. A. Haus. *Waves and Fields in Optoelectronics*. Prentice-Hall, Englewood Cliffs, New Jersey, 1984.

[38] K. Oda, N. Takato, and H. Toba. A wide-FSR waveguide double-ring resonator for optical FDM transmission systems. *J. Lightwave Technol.*, 9(6):728–736, 1991.

[39] R. Orta, P. Savi, R. Tascone, and D. Trinchero. Synthesis of multiple-ring resonator filters for optical systems. *IEEE Photon. Technol. Lett.*, 7(12):1447–1449, 1995.

[40] G. T. Paloczi, Y. Huang, A. Yariv, and S. Mookherjea. Polymeric Mach-Zehnder interferometer using serially coupled microresonators. *Opt. Express*, 11(21):2666–2671, 2003.

[41] J. V. Hryniewicz, P. P. Absil, B. E. Little, R. A. Wilson, and P.-T. Ho. Higher order filter response in coupled microring resonators. *IEEE Photon. Technol. Lett.*, 12(3):320–322, 2000.

[42] A. Melloni, R. Costa, P. Monguzzi, and M. Martinelli. Ring-resonator filters in silicon oxynitride technology for dense wavelength-division multiplexing systems. *Opt. Lett.*, 28(17):1567–1569, 2003.

[43] A. Yariv. Universal relations for coupling of optical power between microresonators and dielectric waveguides. *Electron. Lett.*, 36(4):321–322, 2000.

[44] A. Yariv and P. Yeh. *Optical Waves in Crystals: Propagation and Control of Laser Radiation*. Wiley, New York, 1984.

[45] J. E. Heebner, R. W. Boyd, and Q.-H. Park. SCISSOR solitons and other novel propagation effects in microresonator-modified waveguides. *J. Opt. Soc. Am. B*, 19(4):722–731, 2002.

[46] A. D. Poularikas. *The Handbook of Formulas and Tables for Signal Processing*. IEEE Press, New York, 1998.

[47] S. Longhi, M. Marano, M. Belmonte, and P. Laporta. Superluminal pulse propagation in linear and nonlinear photonic grating structures. *IEEE. J. Sel. Top. Quant. Elect.*, 9(1):4–16, 2003.

[48] J. K. S. Poon, L. Zhu, G. A. DeRose, and A. Yariv. Transmission and group delay in microring coupled-resonator optical waveguides. *Opt. Lett.*, 31(4):456–458, 2006.

[49] F.N. Xia, L. Sekaric, and Y. Vlasov. Ultracompact optical buffers on a silicon chip. *Nature Photonics*, 1(1):65–71, 2007.

[50] S. Olivier, C. Smith, M. Rattier, H. Benisty, C. Weisbuch, T. Krauss, R. Houdre, and U. Osterle. Miniband transmission in a photonic crystal waveguide coupled-resonator optical waveguide. *Opt. Lett.*, 26(13):1019–1051, 2001.

[51] O. J. Painter, K. Srinivasan, and P. E. Barclay. Wannier-like equation for the resonant cavity modes of locally perturbed photonic crystals. *Phys. Rev. B*, 68(6950):035214, 2003.

[52] Z.-Y. Li and K.-M. Ho. Light propagation in semi-infinite photonic crystals and related waveguide structures. *Phys. Rev. B*, 68:155101, 2003.

[53] M. Bayindir, S. Tanriseven, and E. Ozbay. Propagation of light through localized coupled-cavity modes in one-dimensional photonic band-gap structures. *Appl. Phys. A*, 72:117–119, 2001.

[54] W. Chen and D. L. Mills. Gap solitons and the nonlinear optical-response of superlattices. *Phys. Rev. Lett.*, 58(2):160–163, 1987.

[55] C. M. de Sterke and J. E. Sipe. Envelope-function approach for the electrodynamics of nonlinear periodic structures. 38(10):5149–5165, 1988.

[56] C. M. de Sterke, D. G. Salinas, and J. E. Sipe. Coupled-mode theory for light propagation through deep nonlinear gratings. *Phys. Rev. E*, 54(2):1969–1989, 1996.

[57] B. J. Eggleton, R. E. Slusher, C. M. de Sterke, P. A. Krug, and J. E. Sipe. Bragg grating solitons. *Phys. Rev. Lett.*, 76(10):1627–1630, 1996.

[58] D. N. Christodoulides and R. I. Joseph. Slow Bragg solitons in nonlinear periodic structures. *Phys. Rev. Lett.*, 62(15):1746–1749, 1989.

[59] J. B. Khurgin. Optical buffers based on slow light in electromagnetically induced transparent media and coupled resonator structures: comparative analysis. *J. Opt. Soc. Am. B*, 22(5):1062–1074, 2005.

[60] P. Rabiei and W. H. Steier. Tunable polymer double micro-ring filters. *IEEE Photon. Technol. Lett.*, 15(9):1255–1257, 2003.

[61] Y. Yanagase, S. Yamagata, and Y. Kokubun. Wavelength tunable polymer microring resonator filter with 9.4 nm tuning range. *Electron. Lett.*, 39(12):922–924, 2003.

[62] R. Le Dantec, T. Benyattou, G. Guillot, A. Spisser, C. Seassal, J. L. Leclercq, P. Viktorovitch, D. Rondi, and R. Blondeau. Tunable microcavity based on InP-air Bragg mirrors. *IEEE. J. Sel. Top. Quant. Elect.*, 5(1):111–114, 1999.

[63] M. Strassner, C. Luber, A. Tarraf, and N. Chitica. Widely tunable-constant bandwidth monolithic Fabry-Perot filter with a stable cavity design for WDM systems. *IEEE Photon. Technol. Lett.*, 14(11):1548–1550, 2002.

[64] A. Melloni and M. Martinelli. Synthesis of direct-coupled-resonators bandpass filters for WDM systems. *J. Lightwave Technol.*, 20(2):296–303, 2002.

[65] H. F. Taylor. Design of multireflector resonant bandpass filters for guided wave optics. *J. Lightwave Technol.*, 19(6):866 – 871, 2001.

[66] R. Grover, V. Van, T. A. Ibrahim, P. P. Absil, L. C. Calhoun, F. G. Johnson, J. V. Hryniewicz, and P.-T. Ho. Parallel-cascaded semiconductor microring resonators for high-order and wide-FSR filters. *J. Lightwave Technol.*, 20(5):900–905, 2002.

[67] Y. Akahane, T. Asano, B. S. Song, and S. Noda. High-q photonic nanocavity in a two-dimensional photonic crystal. *Nature*, 425(6961):944–947, 2003.

[68] K. Srinivasan, P. E. Barclay, O. J. Painter, J. Chen, A. Y. Cho, and C. Gmachl. Experimental demonstration of a high quality factor photonic crystal microcavity. *Appl. Phys. Lett.*, 83(10):1915–1917, 2003.

[69] J. Niehusmann, A. Vorckel, P. H. Bolivar, T. Wahlbrink, W. Henschel, and H. Kurz. Ultrahigh-quality-factor silicon-on-insulator microring resonator. *Opt. Lett.*, 29(24):2861–2863, 2004.

[70] P. P. Absil, S. T. Chu, D. Gill, J. V. Hryniewicz, F. Johnson, O. King, B. E. Little, F. Seiferth, and V. Van. Very high order integrated optical filters. In *Optical Fiber Communication Conference on CD-ROM*, page TuL3, Washington, DC, 2004. Optical Society of America.

[71] S. C. Hagness, D. Rafizadeh, S. T. Ho, and A. Taflove. FDTD microcavity simulations: design and experimental realization of waveguide-coupled single-mode ring and whispering-gallery-mode disk resonators. *J. Lightwave Technol.*, 15(11):2154–2165, 1997.

[72] e.g. Specifications of the JDS fused coupler, polarization maintaining tap.

[73] A. L. Martin, D. K. Armani, L. Yang, and K. J. Vahala. Replica-molded high-Q polymer microresonators. *Opt. Lett.*, 29(6):533–535, 2004.

[74] S. M. Spillane, T. J. Kippenberg, O. J. Painter, and K. J. Vahala. Ideality in a fiber-taper-coupled microresonator system for application to cavity quantum electrodynamics. *Phys. Rev. Lett.*, 91(4):043902, 2003.

[75] T. J. Karle, D. H. Brown, R. Wilson, M. Steer, and T. F. Krauss. Planar photonic crystal coupled cavity waveguides. *IEEE. J. Sel. Top. Quant. Elect.*, 8(4):909–918, 2002.

[76] S. Nishikawa, S. Lan, N. Ikeda, Y. Sugimoto, H. Ishikawa, and K. Asakawa. Optical characterization of photonic crystal delay lines based on one-dimensional coupled defects. *Opt. Lett.*, 27(23):2079–2081, 2002.

[77] T. D. Happ, M. Kamp, A. Forchel, J. L. Gentner, and L. Goldstein. Two-dimensional photonic crystal coupled-defect laser diode. *Appl. Phys. Lett.*, 82(1):4–6, 2003.

[78] A. A. Savchenkov, V. S. Ilchenko, T. Handley, and L. Maleki. Second-order filter response with series-coupled silica microresonators. *IEEE Photon. Technol. Lett.*, 15(4):543–544, 2003.

[79] D. G. Rabus, M. Hamacher, U. Troppenz, and H. Heidrich. High-Q channel-dropping filters using ring resonators with integrated SOAs. *IEEE Photon. Technol. Lett.*, 14(10):1442–1444, 2002.

[80] S. T. Chu, W. Pan, S. Sato, T. Kaneko, B. E. Little, and Y. Kokubun. Wavelength trimming of a microring resonator filter by means of a UV sensitive polymer overlay. *IEEE Photon. Technol. Lett.*, 11(6):688 – 690, 1999.

[81] H. Haeiwa, T. Naganawa, and Y. Kokubun. Wide range center wavelength trimming of vertically coupled microring resonator filter by direct UV irradiation to SiN ring core. *IEEE Photon. Technol. Lett.*, 16(1):135 – 137, 2004.

[82] S. T. Chu, B. E. Little, V. Van, J. V. Hryniewicz, P. P. Absil, F. G. Johnson, D. Gill, O. King, F. Seiferth, M. Trakalo, and J. Shanton. Compact full C-band tunable filters for 50 GHz channel spacing based on high order micro-ring resonators. In *OSA Trends in Optics and Photonics (TOPS) Vol. 86, Optical Fiber Communication Conference, Technical Digest, Postconference Edition*, page PDP9, Washington, DC, 2004. Optical Society of America.

[83] J. K. S. Poon, Y. Huang, G. T. Paloczi, and A. Yariv. Soft lithography replica molding of critically coupled low-loss polymer microring resonators. *IEEE Photon. Technol. Lett.*, 16(11):2496–2498, 2004.

[84] J. K. S. Poon, Y. Huang, G. T. Paloczi, A. Yariv, C. Zhang, and L. R. Dalton. Wide-range tuning of polymer microring resonators by the photobleaching of CLD-1 chromophores. *Opt. Lett.*, 29(22):2584–2586, 2004.

[85] L. Eldada and L. W. Shacklette. Advances in polymer integrated optics. *IEEE. J. Sel. Top. Quant. Elect.*, 6(1):54–68, 2000.

[86] M.-C. Oh, H. Zhang, C. Zhang, H. Erlig, Y. Chang, B. Tsap, D. Chang, A. Szep, W. H. Steier, H. R. Fetterman, and L. R. Dalton. Recent advances in electroopic polymer modulators incorporating highly nonlinear chromophore. *IEEE. J. Sel. Top. Quant. Elect.*, 7(5):826–835, 2001.

[87] H. Ma, A. K.-Y. Jen, and L. R. Dalton. Polymer-based optical waveguides: materials, processing, and devices. *Adv. Mater.*, 14(19):1339–1365, 2002.

[88] S. Suzuki, Y. Hatakeyama, Y. Kokubun, and S. T. Chu. Precise control of wavelength channel spacing of microring resonator add-drop filter array. *J. Lightwave Technol.*, 20(4):745–750, 2002.

[89] L. Eldada. Advances in telecom and datacom optical components. *Opt. Eng.*, 40(7):1165–1178, 2001.

[90] M. Kawachi. Recent progress in silica-based planar lightwave circuits on silicon. *IEE P.-Optoelectron.*, 143(5):257–262, 1996.

[91] T. Barwicz, M. Popovic, P. T. Rakich, M. R. Watts, H. A. Haus, E. P. Ippen, and H. I. Smith. Microring-resonator-based add-drop filters in SiN: fabrication and analysis. *Opt. Express*, 12(7):1437–1442, 2004.

[92] M. Melchiorri, N. Daldosso, F. Sbrana, L. Pavesi, G. Pucker, C. Kompocholis, P. Bellutti, and A. Lui. Propagation losses of silicon nitride waveguides in the near-infrared range. *Appl. Phys. Lett.*, 86:121111, 2005.

[93] Jr. P. G. Suchoski, T. K. Findakly, and F. J. Leonberger. Stable low-loss proton-exchanged linbo3 waveguide devices with no electro-optic degradation. *Opt. Lett.*, 13(11):1050–1052, 1988.

[94] L. Pavesi and D. J. Lockwood. *Silicon Photonics*. Springer, Berlin, 2004.

[95] T. Brenner and H. Melchior. Integrated optical modeshape adapters in InGaAsP/InP for efficientfiber-to-waveguide coupling. *IEEE Photon. Technol. Lett.*, 5(9):1053–1056, 1993.

[96] Y. N. Xia and G. M. Whitesides. Soft lithography. *Annu. Rev. Mater. Sci.*, 28:153–184, 1998.

[97] Y. Huang, G. T. Paloczi, J. Scheuer, and A. Yariv. Soft lithography replication of polymeric microring optical resonators. *Opt. Express*, 11(20):2452–2248, 2003.

[98] G. T. Paloczi, Y. Huang, A. Yariv, J. Luo, and A. Jen. Replica molded electrooptic polymer Mach-Zehnder modulator. *Appl. Phys. Lett.*, 2004. to be published.

[99] P. P. Absil, J. V. Hryniewicz, B. E. Little, R. A.Wilson, L. G. Joneckis, and P.-T. Ho. Compact microring notch filters. *IEEE Photon. Technol. Lett.*, 12(4):398–400, 2000.

[100] A. Yariv. Critical coupling and its control in optical waveguide-ring resonator systems. *IEEE Photon. Technol. Lett.*, 14(4):483–485, 2002.

[101] G. T. Paloczi, Y. Huang, J. Scheuer, and A. Yariv. Soft lithography molding of polymer integrated optical devices: Reduction of the background residue. *J. Vac. Sci. Tech. B*, 2004. to be published.

[102] V. Van, P. P. Absil, J. V. Hryniewicz, and P.-T. Ho. Propagation loss in single-mode GaAs-AlGaAs microring resonators: measurement and model. *J. Lightwave Technol.*, 19(11):1734–1739, 2001.

[103] C.-Y. Chao and L. J. Guo. Reduction of surface scattering loss in polymer microrings using thermal-reflow technique. *IEEE Photon. Technol. Lett.*, 16(6):1498–1500, 2004.

[104] C. Zhang, L. R. Dalton, M.-C. Oh, H. Zhang, and W. H. Steier. Low V_π electrooptic modulators from CLD-1: Chromophore design and synthesis, material processing, and characterization. *Chem. Mater.*, 13(9):3043–3050, 2001.

[105] A. T. Chen, V. Chuyanov, F. I. MartiCarrera, S. Garner, W. H. Steier, S. S. H. Mao, Y. S. Ra, L. R. Dalton, and Y. Q. Shi. Trimming of polymer waveguide Y-junction by rapid photobleaching for tuning the power splitting ratio. *IEEE Photon. Technol. Lett.*, 9(11):1499–1501, 1997.

[106] M. B. J. Diemeer, F. M. M. Suyten, E. S. Trommel, A. McDonach, J. M. Copeland, L.W. Jenneskens, and W.H.G. Horstuis. Photoinduced channel waveguide formation in nonlinear optical polymers. *Electron. Lett.*, 26(6):379–380, 1990.

[107] S. K. Kim, K. Greary, H. R. Fetterman, C. Zhang, C. Wang, and W. H. Steier. Photo-bleaching induced electro-optic polymer modulators with dual driving electrodes operating at 1.55μm wavelength. *Electron. Lett.*, 39(18):1321–1322, 2003.

[108] A. Galvan-Gonzalez, M. Canva, G. I. Stegeman, R. Tweig, K. P. Chan, T. C. Kowwalczyk, X. Q. Zhang, H. S. Lackritz, S. Marder, and S. Thayumanavan. Systematic behavior of electro-optic chromophore photostability. *Opt. Lett.*, 25(5):332–334, 2000.

[109] C. C. Teng. Traveling-wave polymeric optical intensity modulator with more than 40 GHz of 3-dB electrical bandwidth. *Appl. Phys. Lett.*, 60(13):1538–1540, 1992.

[110] J. K. S. Poon, L. Zhu, G. A. DeRose, and A. Yariv. Polymer microring coupled-resonator optical waveguides. *J. Lightwave Technol.*, 24(4):1843–1849, 2006.

[111] L. Maleki, A. B. Matsko, A. A. Savchenkov, and V. S. Ilchenko. Tunable delay line with interacting whispering-gallery-mode resonators. *Opt. Lett.*, 29(6):626–628, 2004.

[112] S. Mookherjea. Dispersion characteristics of coupled-resonator optical waveguides. *Opt. Lett.*, 30(18):2406–2408, 2005.

[113] e.g. Toray Raytela plastic optical fibers.

[114] Y.-G. Zhao, W.-K. Lu, Y. Ma, S.-S. Kim, and S. T. Ho. Polymer waveguides useful over a very wide wavelength range from the ultraviolet to infrared. *Appl. Phys. Lett.*, 77(19):2961–2963, 2000.

[115] A. Stapleton, S. Farrell, H. Akhavan, R. Shafiiha, Z. Peng, S.-J. Choi, J. O'Brien, and P. D. Dapkus. Optical phase characterization of active semiconductor microdisk resonators in transmission. *Appl. Phys. Lett.*, 88(3):031106, 2006.

[116] Y. Q. Shi, C. Zhang, H. Zhang, J. H. Bechtel, L. R. Dalton, B. H. Robinson, and W. H. Steier. Low (sub-1-volt) halfwave voltage polymeric electro-optic modulators achieved by controlling chromophore shape. *Science*, 288(5463):119–122, 2000.

[117] S. L. Logunov. Cavity ringdown detection of losses in thin films in the telecommunication wavelength window. *Appl. Opt.*, 40(9):1570–1573, 2001.

[118] H. Kogelnik and C. V. Shank. Coupled-wave theory of distributed feedback lasers. *J. Appl. Phys.*, 43(5):2327–2335, 1972.

[119] J. C. Knight, J. Arriaga, T. A. Birks, A. Ortigosa-Blanch, W. J. Wadsworth, and P. St. Russell. Anomalous dispersion in photonic crystal fiber. *IEEE Photon. Technol. Lett.*, 12(7):807–809, 2000.

[120] M. Notomi, K. Yamada, A. Shinya, J. Takahashi, C. Takahashi, and I. Yokohama. Extremely large group-velocity dispersion of line-defect waveguides in photonic crystal slabs. *Phys. Rev. Lett.*, 87(25):253902, 2001.

[121] T. Asano, K. Kiyota, D. Kumamoto, B.-S. Song, and S. Noda. Time-domain measurement of picosecond light-pulse propagation in a two-dimensional photonic crystal-slab waveguide. *Appl. Phys. Lett.*, 84(23):4690–4692, 2004.

[122] T. J. Karle, Y. J. Chai, C. N. Morgan, I. H. White, and T. F. Krauss. Observation of pulse compression in photonic crystal coupled cavity waveguides. *J. Lightwave Technol.*, 22(2):514–519, 2004.

[123] W. J. Kim, W. Kuang, and J. D. O'Brien. Dispersion characteristics of photonic crystal coupled resonator optical waveguides. *Opt. Express*, 11(25):3431–3437, 2003.

[124] J. B. Khurgin. Expanding the bandwidth of slow-light photonic devices based on coupled resonators. *Opt. Lett.*, 30(5):513–515, 2005.

[125] J. K. Ranka, R. S. Windeler, and A. J. Stentz. Visible continuum generation in air-silica microstructure optical fibers with anomalous dispersion at 800 nm. *Opt. Lett.*, 25(1):25–27, 2000.

[126] J. K. S. Poon and A. Yariv. Active coupled-resonator optical waveguides – Part I: Gain enhancement and noise. 2007. (Submitted to J. Opt. Soc. Am. B).

[127] R. K. Chang and A. J. Campillo. *Optical Processes in Microcavities*. World Scientific, Singapore, 1996.

[128] C. H. Henry. Theory of spontaneous emission noise in open resonators and its application to lasers and optical amplifiers. *J. Lightwave Technol.*, 4(3):288–297, 1986.

[129] J. P. Dowling, M. Scalora, M. J. Bloemer, and C. M. Bowden. The photonic band-edge laser – a new approach to gain enhancement. *Appl. Phys. Lett.*, 75(4):1896–1899, 1994.

[130] S. Nojima. Enhancement of optical gain in two-dimensional photonic crystals with active lattice points. *Jpn. J. Appl. Phys.*, 37(5):L565–L567, 1998.

[131] L. Florescu, K. Busch, and S. John. Semiclassical theory of lasing in photonic crystals. *J. Opt. Soc. Am. B*, 19(9):2215–2223, 2002.

[132] P. Chak and J.E. Sipe. Minimizing finite-size effects in artificial resonance tunneling structures. *Opt. Lett.*, 13(17):2568–2570, 2006.

[133] J. K. S. Poon, P. Chak, J. M. Choi, and A. Yariv. Slowing light with Fabry-Perot resonator arrays. 2007. (Submitted to J. Opt. Soc. Am. B).

[134] W. C. Yueh. Explicit inverses of several tridiagonal matrices. *Appl. Math. E-Notes*, 6:74–83, 2006.

[135] T. Mukai and Y. Yamamoto. Noise in an AlGaAs semiconductor-laser amplifier. *IEEE J. Quant. Elect.*, 18(4):564–575, 1982.

[136] N. A. Olsson. Heterodyne gain and noise measurement of a $1.5\mu m$ resonant semiconductor-laser amplifier. *IEEE J. Quant. Elect.*, 22(5):671–676, 1986.

[137] R. J. Lang and A. Yariv. Semiclassical theory of noise in multielement semiconductor lasers. *IEEE J. Quant. Elect.*, 22(3):436–449, 1986.

[138] A. Yariv. *Quantum Electronics*. Wiley, New York, 3rd edition, 1989.

[139] Y. A. Vlasov and S. J. McNab. Coupling into the slow light mode in slab-type photonic crystal waveguides. *Opt. Lett.*, 31(1):50–52, 2006.

[140] G. P Agrawal and N. K. Dutta. *Long-Wavelength Semiconductor Lasers*. Van Nostrand Reinhold Company, New York, 1986.

[141] S. Mookherjea. Spectral characteristics of coupled resonators. *J. Opt. Soc. Am. B*, 23(6):1137–1145, 2006.

[142] S. Mookherjea and A. Oh. Effect of disorder on slow light velocity in optical slow-wave structures. *Opt. Lett.*, 32(3):289–291, 2007.

[143] D. Botez and D. R. Scifres. *Diode Laser Arrays*. Cambridge University Press, Cambridge, 1994.

[144] S. Fan, P. R. Villeneuve, J. D. Joannopoulos, and H.A. Haus. Channel drop filters in photonic crystals. *Opt. Express*, 3(11):4–11, 1998.

[145] Y. Xu, Y. Li, R. K. Lee, and A. Yariv. Scattering-theory analysis of waveguide-resonator coupling. *Phys. Rev. E*, 62(5):7389–7404, 2000.

[146] M. Sumetsky and B.J. Eggleton. Modeling and optimization of complex photonic resonant cavity circuits. *Opt. Express*, 11(4):381–391, 2003.

[147] S. Mookherjea. Using gain to tune the dispersion relation of coupled-resonator optical waveguides. *IEEE Photon. Technol. Lett.*, 18(5):715–717, 2006.

[148] J. K. S. Poon, L. Zhu, G. A. DeRose, J. M. Choi, and A. Yariv. Active coupled-resonator optical waveguides – Part II: Current injection InP-InGaAsP Fabry-Perot resonator arrays. 2007. (Submitted to J. Opt. Soc. Am. B).

[149] K. L. Koch, P. J. Corvini, and W. T. Tsang. Anisotropically etched deep gratings for InP/InGaAsP optical devices. *J. Appl. Phys.*, 62(8):3461–3463, 1987.

[150] E. Inamura, Y. Miyamoto, S. Tamura, T. Takasugi, and K. Furuya. Wet chemical etching for ultrafine periodic structure: Rectangular InP corrugations of 70 nm pitch and 100 nm pitch depth. *Jpn. J. Appl. Phys.*, 28(10):2193–2196, 1989.

[151] H. Namatsu, Y. Takahashi, K. Yamazaki, T. Yamaguchi, M. Nagase, and K. Kurihara. Three-dimensional siloxane resist for the formation of nanopatterns with minimum linewidth fluctuations. *J. Vac. Sci. Tech. B*, 16(1):69–76, 1998.

[152] M. Hatzakis, B. J. Canavello, and J. M. Shaw. Single-step optical lift-off process. *IBM J. Res. Develop.*, 24(4):452–460, 1980.

[153] W. W. Chow, S. W. Koch, and M. Sargent III. *Semiconductor-Laser Physics*. Springer, Berlin, 1997.

[154] H. G. Winful, S. Allen, and L. Rahman. Validity of the coupled-oscillator model for laser-array dynamics. *Opt. Lett.*, 18(21):1810–1812, 1993.

[155] A. E. Siegman. *Lasers*. University Science Books, Mill Valley, 1986.

[156] L. Goldberg, H. F. Taylor, J. F. Weller, and D. R. Scifres. Injection locking of coupled-stripe diode laser arrays. *Appl. Phys. Lett.*, 46(3):236–238, 1985.

[157] J. P. Hohimer, A. Owyoung, and G. R. Hadley. Single-channel injection locking of a diode-laser array with a cw dye laser. *Appl. Phys. Lett.*, 47(12):1244–1246, 1985.

[158] B. Bauer, F. Henry, and R. Schimpe. Gain stabilization of a semiconductor optical amplifier by distributed feedback. *IEEE Photon. Technol. Lett.*, 6(2):182–185, 1994.

[159] L. F. Tiemeijer, P. J. A. Thijs, T. Dongen, J. J. M. Binsma, E. J. Jansen, and H. R. J. R. Vanhelleputte. Reduced intermodulation distortion in 1300 nm gain-clamped MQW laser amplifiers. *IEEE Photon. Technol. Lett.*, 7(3):284–286, 1995.

[160] M. Bachmann, P. Doussiere, J. Y. Emery, R. NGo, F. Pommereau, L. Goldstein, G. Soulage, and A. Jourdan. Polarisation-insensitive clamped-gain SOA with integrated spot-size convertor and DBR gratings for WDM applications at 1.55μm wavelength. *Electron. Lett.*, 32(22):2076–2078, 1996.

[161] W. Liang, L. Yang, J. K. S. Poon, Y. Y. Huang, K. J. Vahala, and A. Yariv. Transmission characteristics of a Fabry-Perot etalon-microtoroid resonator coupled system. *Opt. Lett.*, 31(4):510–512, 2006.

[162] J. K. S. Poon, J. Scheuer, and A. Yariv. Frequency-selective reflector based on a circular array of coupled microring resonators. *IEEE Photon. Technol. Lett.*, 16(5):1331–1333, 2004.